Design and implementation of a monochromatic high harmonic generation light source at 100 kHz and its application to time- and angle-resolved photoelectron spectroscopy on Bi_2Se_3

Dissertation

zur

Erlangung der naturwissenschaftlichen Doktorwürde
(Dr. sc. nat.)

vorgelegt der

Mathematisch-naturwissenschaftlichen Fakultät

der

Universität Zürich

von

Adrian Christian Schuler
von Zermatt (VS)

Promotionskommission

Prof. Dr. Jürg Osterwalder (Vorsitz und Leitung der Dissertation)
Dr. Matthias Hengsberger
Prof. Dr. Michael Bauer
Prof. Dr. Thomas Greber

Zürich 2018

Abstract

Besides the interest in many industrial applications, the development of new laser systems is important to study electronic properties of materials like, e.g. carrier lifetimes and mobility. Such physical properties can be observed with pulsed laser light sources employed in a pump-probe scheme.

Angle-resolved photoelectron spectroscopy (ARPES) is an experimental technique to map the electron distribution of crystals. The first Brillouin zone is the smallest unit of the reciprocal space and represents the complete solid. To cover the full Brillouin zone, extreme ultraviolet (XUV) photon energies are needed. If ARPES is employed in a pump-probe scheme, the real-time evolution of the band structure can be observed. Therefore, a pulsed XUV light source provides the foundation to observe the temporal evolution of the electron distribution of the full first Brillouin zone.

The main objective of this thesis is the design and implementation of a high harmonic (HHG) light source with high repetition rate in combination with the photoemission setup TREx. For this purpose, the second harmonic from our femtosecond Ti:sapphire laser system serves as driving laser to generate the 5th harmonic with 15 eV photons in Ar^+ gas at a repetition rate of 100 kHz. If the fundamental and the XUV pulses are employed in a pump-probe scheme, it is possible to observe charge carrier dynamics in materials with time- and angle-resolved photoelectron spectroscopy (trARPES).

The topological insulator Bi_2Se_3 was the first system studied by means of trARPES with the new HHG light source. The out-of-equilibrium dynamics for the occupied and unoccupied band structure at different momenta in k-space were recorded. Furthermore, the temporal evolution of the characteristic topological surface state at $\overline{\Gamma}$ could be observed. The hot electron dynamics at $\overline{\mathrm{M}}$ and $\overline{\mathrm{M}}'$ are attributed to the unoccupied conduction band. In our data, the depletion in the valence band due to the excitation of the electrons and a transient broadening of the occupied bands was observed.

A second system studied with the new light source was h-BN/Ni(111). It is a possible candidate for valleytronic applications in which the location of excited electrons in reciprocal-space is used as information carrier. The goal was to excite electrons into the conduction band minimum at $\overline{\mathrm{K}}$ at the border of the Brillouin zone and to observe the population using HHG light. The population of the conduction band

valley at $\overline{\mathrm{K}}$ could not be observed so far which could tentatively be attributed to the limitation of the pump photon energy. Due to time restrictions, this project could not be finished.

In previous experiments, it could be shown that trARPES data contain information about structural dynamics. Using the photoswitchable molecule tetra-tert-butyl-azobenzene (TBA) as a model system corroborated with multi-scattering calculations we could show that this method is a very sensitive tool for tracking configuration changes.

Zusammenfassung

Neben dem Interesse für viele industrielle Anwendungen ist die Entwicklung neuer Lasersysteme wichtig um elektronische Eigenschaften von Materialien zu untersuchen, wie z.B. Lebenszeiten von Ladungsträgern und dessen Mobilitäten. Solche physikalischen Eigenschaften können mit gepulsten Laserlichtquellen, angewandt in einem Pump-Probe Aufbau, beobachtet werden.

Winkelaufgelöste Photoelektronenspektroskopie (ARPES) ist eine experimentelle Methode zur Abbildung der Elektronenverteilung in Kristallen. Die erste Brillouin-Zone ist die kleinste Einheit des reziproken Raumes und repräsentiert den vollständigen Festkörper. Damit die gesamte Brillouin-Zone untersucht werden kann, werden extem-ultraviolette (XUV) Photonenenergien benötigt. Falls ARPES in einem Pump-Probe Aufbau angewendet wird, kann die zeitliche Entwicklung der Bandstruktur beobachtet werden. Deshalb bildet eine gepulste XUV Lichtquelle die Grundlage zur Beobachtung der zeitlichen Entwicklung der Elektronenverteilung der gesamten ersten Brillouin-Zone.

Das Hauptziel dieser Dissertation ist der Entwurf und der Aufbau einer Höher Harmonischen (HHG) Lichtquelle bei hohen Repetitionsraten in Kombination mit dem Photoemissionsaufbau TREx. Zu diesem Zweck wurde die zweite Harmonische von unserem femtosekunden Titan:Saphir Oszillator Lasersystem benutzt, um die 5te Harmonische mit 15 eV Photonenenergie in Ar^+ Gas bei einer Repetitionsrate von 100 kHz zu erzeugen. Werden die Fundamentale und die XUV Pulse in einem Pump-Probe Aufbau angewendet, ist es möglich mit zeit und winkelaufgelöster Photoelektronenspektroskopie (trARPES) die Ladungsträgerdynamik in Materialien zu untersuchen.

Der topologische Isolator Bi_2Se_3 war das erste System welches mittels trARPES mit der neuen HHG Lichtquelle untersucht wurde. Die Dynamik für das aus dem Gleichgewicht getriebenen System wurde für verschiedene Momenta der besetzten und unbesetzten Bandstruktur im reziproken Raum aufgenommen. Weiterhin wurde die zeitliche Entwicklung des charakteristischen topologischen Oberflächenzustandes bei $\overline{\Gamma}$ beobachtet. Die Dynamik der heissen Elektronen bei $\overline{\mathrm{M}}$ und $\overline{\mathrm{M}'}$ wurde dem unbesetzten Valenzband zugeschrieben. Weiterhin wurde in unseren Daten die Verarmung durch Elektronenanregung im Valenzband und eine transiente Verbreiterung der besetzten Zustände beobachtet.

Ein zweites System welches mit der neuen Lichtquelle untersucht wurde ist h-BN/Ni(111). Dies ist ein möglicher Kandidat für valleytronics Anwendungen in welchen der Ort der angeregten Elektronen im reziproken Raum als Informatrionsträger genutzt wird. Das Ziel war die Elektronen ins Leitungsbandminimum bei $\overline{\mathrm{K}}$ an der Brillouin-Zonengrenze anzuregen und die Bevölkerung mittels HHG Licht zu beobachten. Die Bevölkerung des Leitungsbandminimums bei $\overline{\mathrm{K}}$ konnte bis jetzt nicht beobachtet werden was möglicherweise mit der Limitierung der Pumpphotonenenergie zu tun hat. Auf Grund der zeitlichen Limitierung konnte dieses Projekt nicht abgeschlossen werden.

In vorangegangenen Experimenten konnte gezeigt werden, dass trARPES Daten Informationen über strukturelle Änderungen beinhaltet. Mit dem Modellsystem Tetra-tert-butyl Azobenzen (TBA) welches mittels Photonen eine strukturelle Änderung erfährt konnten wir in Kombination mit Multiplenstreurechnungen zeigen, dass diese Methode ein sensitives Werkzeug ist um Änderungen von Konfigurationen zu verfolgen.

List of Acronyms

2PPE	two-photon photoemission
AC	analysis chamber
ARPES	angle-resolved photoelectron spectroscopy
BBO	beta barium borate
BCB	bulk conduction band
BVB	bulk valence band
BZ	brillouin zone
CPA	chirped pulse amplification
CVD	chemical vapor deposition
EDC	energy-distribution curve
fcc	face centered cubic
FHG	fourth harmonic generation
FROG	frequency-resolved optical gating
FS	fused silica
FWHM	full width half maximum
h-BN	hexagonal boron nitride
HH	high-harmonic
HHG	high-harmonic generation
IMFP	inelastic mean free path
IPS	image potential state
IR	infrared radiation
IS	interface state
LEED	low energy electron diffraction
LL	load lock
MCP	micro channel plate
ML	multilayer
OPA	optical parametric amplifier

PC	preparation chamber
PED	photoelectron diffraction
PES	photoelectron spectroscopy
PSD	position sensitive detector
PSS	photostationary state
QH	quantum Hall
QSH	quantum spin Hall
SBZ	surface Brillouin zone
SHG	second harmonic generation
SOC	spin-orbit coupling
SPV	surface photovoltage
SS	surface state
TI	topological insulator
TMP	turbo molecular pump
TR	time-reversal
tr2PPE	time-resolved two-photon photoemission
trARPES	time- and angle-resolved photoelectron spectroscopy
TREx	time-resolved experiment
TRIM	time-reversal-invariant momentum
trPED	time-resolved photoelectron diffraction
TSS	topological surface state
UHV	ultra high vacuum
UPS	UV photoelectron spectroscopy
USR	unoccupied surface resonance
XPD	x-ray photoelectron diffraction
XPS	x-ray photoelectron spectroscopy

Contents

1 Introduction

Electronic properties like, e.g. carrier lifetimes and mobilities are important for the application in modern electronics. Besides the introduction of new materials, the development of new laser systems is of great significance to study the physical properties of these materials.

Historically, the foundation for the development of the laser (light amplification by stimulated emission of radiation) is dated back to 1917. A. Einstein published the work on the quantum theory of radiation [1]. The theoretical concept describes that electrons cannot only absorb and emit light spontaneously, but they can also be stimulated to emit light of a specific wavelength. This is called stimulated emission. It took almost forty years for the first experimental proof of Einstein's theory. In 1953, C.H. Townes and his co-workers constructed the first maser (microwave amplification by stimulated emission of radiation) with a wavelength of a little more than one centimeter from excited ammonia molecules [2]. In the following years, Townes was extending his work on stimulated emission to obtain radiation of shorter wavelengths. In 1958, C.H. Townes and A.L. Schawlow introduced the idea of a maser working in the infrared and optical range [3]. T.H. Maiman then built the first working laser in 1960. This ruby laser was the first application of stimulated emission of infrared radiation (700 nm) [4].

Today, almost sixty years later, lasers are present in countless applications. In science, the laser became an important device where it is used to study physical and chemical properties of matter like molecular vibrations, chemical reactions or electron dynamics in materials. The wide range of wavelengths available from far-infrared to UV is important for the light-matter interaction. Thus, the wavelength to be chosen depends on the physical effect to be studied. Although, there is a limitation in wavelength in the UV range, where the large atomic and molecular resonances for UV radiation lead to rather high absorption of the light in air. Therefore, the nonlinear optical process to generate photon energies above 7 eV [5] is inefficient in air. However, this can be overcome by generating XUV light in vacuum.

High harmonic generation (HHG) in rare gases represents a low cost, table-top technique to produce XUV laser pulses in vacuum. Therefore an intense laser field interacting with the rare gas generates multiple odd harmonics of the driving laser photon energy. The energy range provided by this technique starts at few tens to many hundreds of electron volts. The potential of this type of light sources was proposed [6] shortly after its discovery in 1987 [7]. Since then, many new experimental HHG setups were designed and implemented for different applications such as static ARPES[8] and time-resolved ARPES[9], attosecond pulses applications[10] and microscopy[11].

The main part of this thesis, presented in chapter 3, was the development and characterization of a photoemission setup with femtosecond high harmonic generation. It enables us to carry out trARPES from solids with monochromatic XUV light. The high repetition rate HHG setup combined with the five-axis sample manipulator and two-dimensional hemispheric display analyzer is well suited to measure trARPES maps avoiding space-charge effects due to high pulse energies at low repetition rates [12].

In chapter 5, the trARPES measurements on Bi_2Se_3 recorded with the high harmonic generation setup is shown. It was the first system measured because the understanding so far lacks the electron dynamics at the Brillouin zone boundaries and the bulk valence band structure. The response of the system due to the pumping with 800 nm light is large [13]. Furthermore, the first Brillouin zone ($\sim 1\,\text{Å}^{-1}$) is rather small, which allows the high-symmetry point L and F to be measured in a pump-probe scheme even at fairly low photon energies.

The access to the full first Brillouin zone provided by the XUV photon energies is ideal to study valleytronic systems [14]. The direct transition of bound electronic states to valleys in the unoccupied states at the Brillouin zone boundaries in these materials can be studied by means of pump-probe spectroscopy [15]. In most materials, the selectivity of the valley is done by spin selection which can be achieved rather easily by circularly polarized light. Our first valleytronics candidate is h-BN/Ni(111), which is discussed in chapter 4. The π^*-band with predicted local minima at the high-symmetry points $\overline{\mathrm{K}}$ and $\overline{\mathrm{K'}}$ [16] can be reached with photon energies starting from 15 eV. The conjectured difference in electron spin density offers the possibility of valleytronics by exciting the electrons from the Ni3d states with circularly polarized light into the π^*-band of h-BN.

In chapter 6, a study of the sensitivity of photoelectron diffraction to conformational changes is shown. Structural changes upon photoexcitation are important among functionalization of molecules. Photoinduced structural changes of tetra-tert-butyl-azobenzene adsorbed on Au(111) were shown by means of STM [17] and tr2PPE [18]. Time-resolved photoelectron diffraction with high harmonics could combine the direct observation of the structural change with femtosecond resolution. The sensitivity of photoelectron diffraction to structural changes has to be clarified because an ensemble of molecules is measured, but usually, only a few percents of the molecules change their configuration upon photoexcitation in a pump-probe experiment from solids.

Chapter 7 gives an outlook of the possible future application for the new pulsed XUV light source and how the light source will be improved to extend the pump photon energies. The conclusions are presented at the end of each chapter.

2 Photoemission from solids

2.1 Photoelectron spectroscopy

Photoelectron spectroscopy (PES) is based on the photoelectric effect, which was first observed by Hertz [19] in 1887 and explained in 1905 by Einstein [20], who explained it with the quantum nature of light. The photoelectric effect describes the emission of electrons under irradiation of light. If the energy of the photon $h\nu$ absorbed by an electron of the solid is large enough to overcome the binding energy E_{B} of the electron and the work function of the sample ϕ, the electron can leave the solid and can be detected by a photoelectron analyzer by recording its residual kinetic energy E_{kin} and emission angle. The kinetic energy of the electron is then given by the equation

$$E_{\mathrm{kin}} = h\nu - E_{\mathrm{B}} - \phi \tag{2.1}$$

where h is the constant of Planck and ν the frequency of the incoming photon. This equation allows us to directly calculate the binding energy of the emitted electron from the recorded kinetic energy. One obtains a photoelectron spectrum with characteristic lines for all distinct binding energies of the electrons in the solid (figure 2.1b and 2.2).

A phenomenological approach to the photoemission process is the three-step model:

Step 1: The electron in the solid is optically excited via absorption of a photon. The transition from the initial state with the energy $E_{\mathrm{i}}(k_{\mathrm{i}})$ to the final state $E_{\mathrm{f}}(k_{\mathrm{f}})$ is momentum and energy conserved. The momentum transfer from a UV photon can be neglected compared to the momentum of the electron. Thus the momentum of the photoelectron in the final state is approximately the same as in the initial state modulo G in the extended Brillouin zone scheme $\mathbf{k}_{\mathrm{f}} = \mathbf{k}_{\mathrm{i}} + \mathbf{G}$ where $\mathbf{G}$ is the reciprocal lattice vector.

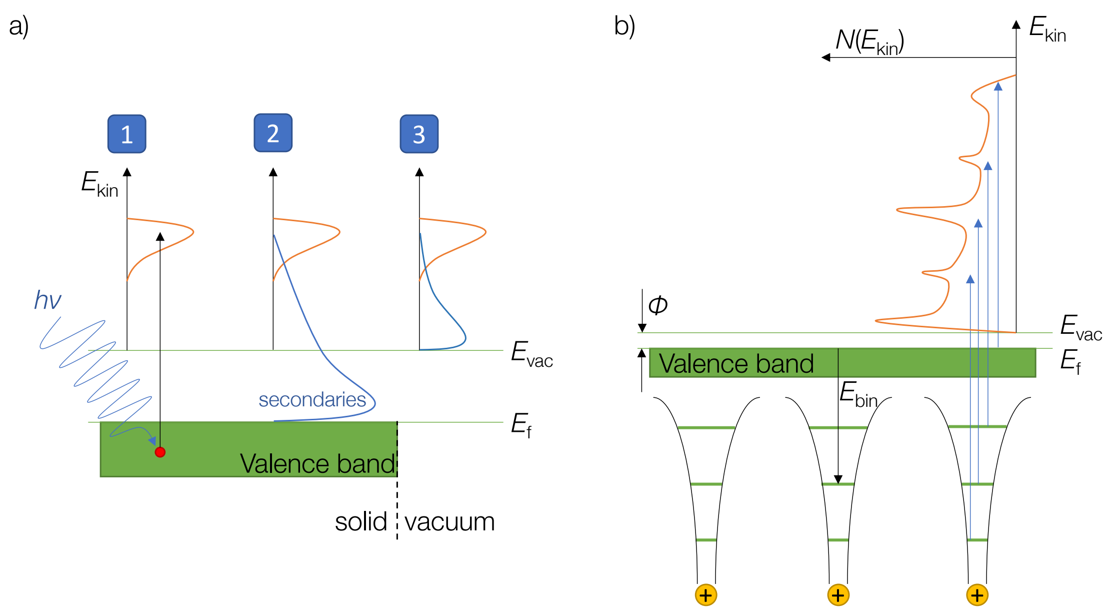

Figure 2.1 **a)** Illustration of the photoemission tree-step process. 1) Excitation of the electron inside the crystal by absorption of a photon with the energy hν. 2) Transport of the photoelectron to the surface. The electron loses energy on the way by inelastic processes which creates a background of secondaries. 3) The photoelectron escapes through the surface potential barrier into the vacuum and is detected by the electron analyzer. **b)** Sketch of a photoelectron spectrum with the characteristic lines for the core level and valence electrons. Adapted from [21] and [22].

The optical transition rate W_{if} for an electron with the initial state $|i\rangle$ into the final state $|f\rangle$ after the excitation is described by Fermi's golden rule

$$W_{if} \propto \sum_{i,f} \frac{2\pi}{\hbar} |\langle\psi_i|H'|\psi_f\rangle|^2 \delta(E_f - E_i - h\nu) \tag{2.2}$$

where the δ-function ensures the energy conservation for the allowed transitions and H' is the Hamiltonian which describes the perturbation by the electromagnetic field. The derivation of Fermi's golden rule is not done at this point but can be found in [21].

Step 2: The transport of the photoelectron from inside the crystal to the surface. The electron loses energy due to inelastic processes while being transported to the surface. These losses create a background of secondaries. The inelastic mean free path (IMFP) of the photoelectrons is mainly determined by the electron density within the solid and depends on the kinetic energy. The elastic peaks in PES are interpreted as lines without losses.

Step 3: The photoelectron escapes through the surface potential barrier into the vacuum where it is detected by the photoelectron analyzer. Step 3 is important for angle-resolved photoelectron spectroscopy (ARPES) and will be discussed in detail in the following section.

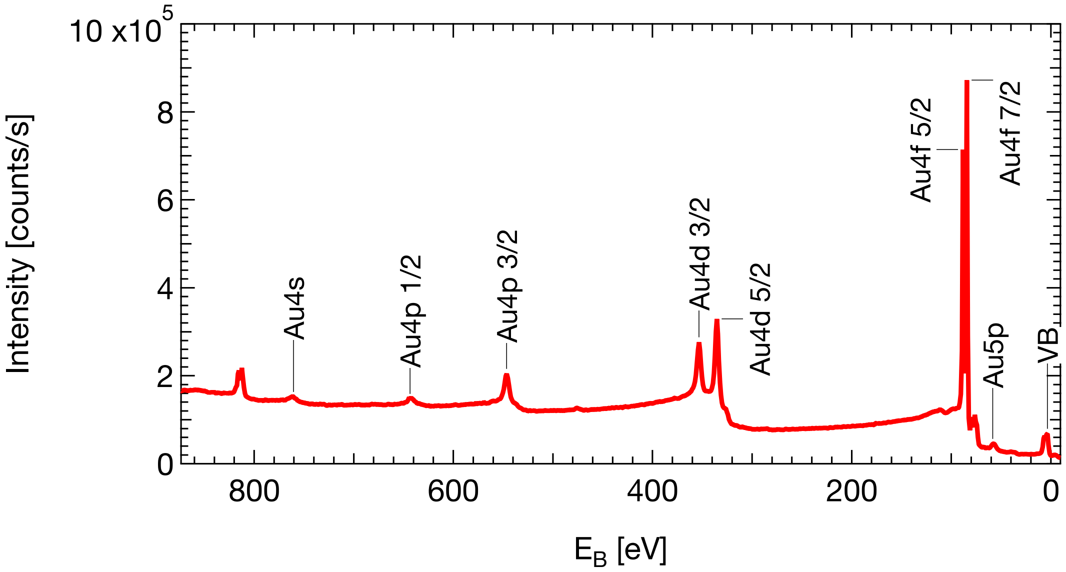

Figure 2.2 Measured x-ray photoelectron spectroscopy (XPS) data of bare Au(111) recorded with the MgKα emission line ($h\nu = 1253.4\,\mathrm{eV}$). In this figure the most important elastic lines corresponding to the core level and valence electrons are labeled.

The type of a light source is chosen to the specific needs of the physical question to be answered. The x-ray energy range is used to excite the core-level electrons within the solid. Tunable light sources are provided by synchrotrons where photon energies in the range of a few tens of electron volt up to multiple keV can be generated. X-ray tubes with distinct photon energies are used in labs. Depending on the anode material, e.g. Magnesium, Silicon or Aluminum, the photon energies are typically in the range of $1 - 2\,\mathrm{keV}$.

To excite the valence electrons, it is more convenient to use low photon energies in the range of $5 - 50\,\mathrm{eV}$ because the cross-sections for valence electrons are higher at low photon energies and the bandwidth is smaller providing a higher energy resolution. Regarding tunable light sources, some facilities can provide these energies. Within the laboratory environment the standard tools are high-intensity Helium lamps which provide the distinct emission lines of helium-like 21.2 eV and 40.8 eV.

2.2 ARPES

ARPES is one of the key tools to study the electronic structure of solids [23]. Most physical properties of solids are defined by the electron distribution around the Fermi energy E_F. A typical ARPES experiment is shown in figure 2.3 and the momenta of the detected photoelectrons can be written as

$$k_\mathrm{x} = \frac{1}{\hbar}\sqrt{2m_\mathrm{e}E_\mathrm{kin}^\mathrm{vac}\sin(\theta)\cos(\phi)} \tag{2.3}$$

$$k_\mathrm{y} = \frac{1}{\hbar}\sqrt{2m_\mathrm{e}E_\mathrm{kin}^\mathrm{vac}\sin(\theta)\sin(\phi)} \tag{2.4}$$

$$k_\mathrm{z} = \frac{1}{\hbar}\sqrt{2m_\mathrm{e}E_\mathrm{kin}^\mathrm{vac}\cos(\theta)} \tag{2.5}$$

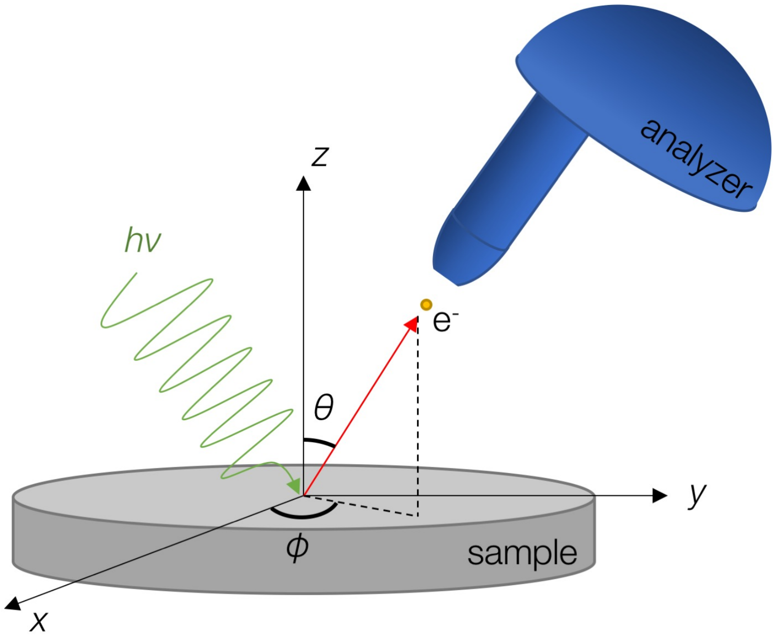

Figure 2.3 Illustration of an ARPES experiment. The optically excited electrons are detected by the electron analyzer which is set to a given E_kin and counts the electrons emitted into a chosen angular window. This information leads to the calculation of the energy and momenta of the initial state of the electrons inside the solid.

One issue of the detected photoelectrons is that they are detected in vacuum, i.e. after they left the potential range of the solid. Therefore a closer look at the momenta is required (Step 3 of the three-step model).

In order to leave the solid, the excited photoelectron needs to gain enough energy from the photon to overcome the surface potential barrier. Thus, the photoelectron in the solid needs to have at least an energy of $(\hbar^2/2m){k'_\perp}^2 \geq (\hbar^2/2m){k_\perp}^2 + E_0$, which leads to a minimum momenta needed $k'_{\text{min}\perp}$ (see figure 2.4b). E_0 is the energy of the valence band bottom (inner potential). The relation between the measured momenta and the initial momenta is discussed separately for the parallel and perpendicular components:

Parallel momenta: The transmission through the surface leaves the parallel component of the momentum $k_\parallel$ conserved, and the momentum conservation can be written as (see figure 2.4a)

$$k'_\parallel = \frac{1}{\hbar}\sqrt{2m_\text{e}E_\text{kin}^\text{solid}}\sin(\theta') = \frac{1}{\hbar}\sqrt{2m_\text{e}E_\text{kin}^\text{vac}}\sin(\theta) = k_\parallel \tag{2.6}$$

where $\hbar$ denotes the reduced Planck constant, m_e is the mass of the electron, $k'_\parallel$ and $k_\parallel$ are the momenta of the excited electron inside and outside the solid. $E_\text{kin}^\text{solid}$ and θ' describe the excited final state in the solid. E_kin^vac and θ are values which can be measured in a ARPES experiment. $k'_\parallel$ of the excited final state in the solid can be calculated from the ARPES observables E_kin^vac and θ by

$$k'_\parallel = 0.512\sqrt{2m_\text{e}E_\text{kin}^\text{vac}\sin(\theta)} \tag{2.7}$$

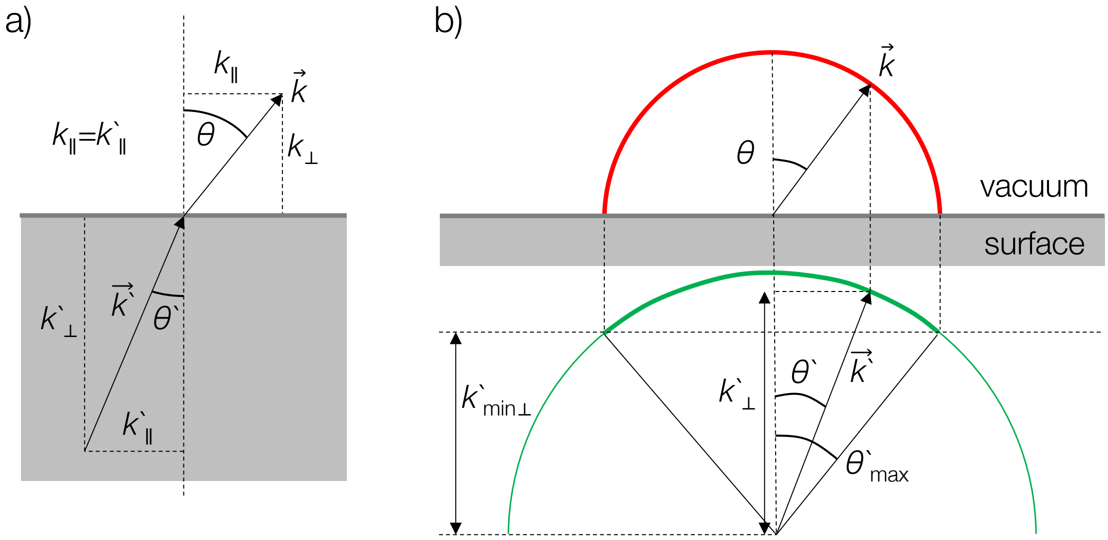

Figure 2.4 Refraction at the surface: **a)** $k'_\parallel$ of the photoelectron is conserved passing through the surface while $k'_\perp$ is changed by the surface potential step. **b)** Scheme of the photoemission horizon due to the refraction. The photoelectrons need to have at least a momentum of $k'_{\text{min}\perp}$ to escape. The solid lines depict the escape cones inside the crystal and in vacuum. Adapted from [21].

Perpendicular momenta: The perpendicular momentum is more complex due to the surface potential step [22] which is defined by the inner potential E_0. Therefore, $k'_\perp$ can be written as

$$k'_\perp = \frac{1}{\hbar}\sqrt{2m_\mathrm{e}\left(E_\mathrm{kin}^\mathrm{vac}\cos^2(\theta) + E_0\right)} \tag{2.8}$$

considering $E_\mathrm{kin}^\mathrm{vac} = E_\mathrm{kin}^\mathrm{solid} - E_0$. The calculation of $k'_\perp$ requires the inner potential E_0, which is a fit parameter or empirical parameter which usually is energy-dependent.

2.3 tr2PPE and trARPES

Femtosecond laser systems with photon energies below the workfunction of the sample and with intensities high enough to allow multiphoton ionization offer the possibility to study the temporal evolution of the unoccupied electronic states inbetween the Fermi energy and the vacuum level with femtosecond time resolution [24, 25]. The photon energies for time-resolved two-photon photoemission (tr2PPE) [26] fulfill the relation $h\nu_1, h\nu_2 < \phi < h\nu_1 + h\nu_2$. In figure 2.5, the process of tr2PPE is illustrated.

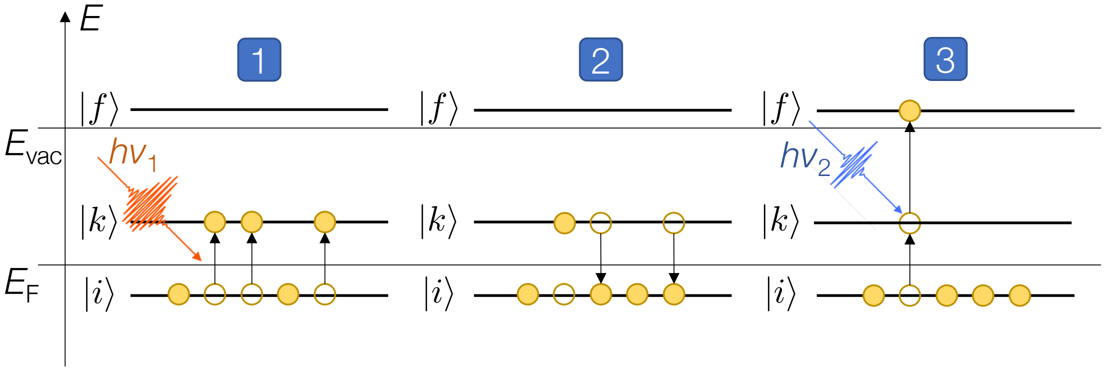

Figure 2.5 Illustration of the tr2PPE process. The photon energies for tr2PPE must fulfill the condition $h\nu_1, h\nu_2 < \phi < h\nu_1 + h\nu_2$. Step 1: A first femtosecond laser pulse $h\nu_1$ exites electrons from the initial state $|i\rangle$ into the intermediate state $|k\rangle$. Step 2: The excited electrons in the intermediate state may relax via elastic and inelastic process back into the initial state. The sum of these processes define the relaxation time τ of the intermediate state. Step 3: A second laser pulse $h\nu_2$ excites electrons after a certain time delay Δt from the intermediate state into the final state $|f\rangle$ above the vacuum level. These photoelectrons will then be recorded by the electron analyzer. The figure is inspired by the "Electron spectroscopies" lecture at University of Zürich.

Step 1: A first laser pulse (pump pulse) with the photon energy of $h\nu_1$ excites electrons from the initial state $|i\rangle$ into an intermediate state $|k\rangle$.

Step 2: After the excitation, the electrons in the intermediate state can relax via various elastic and inelastic processes like, e.g. electron-hole pair excitation or electron-phonon coupling. These processes define the lifetime τ (relaxation time) of the intermediate state.

Step 3: After a defined time delay Δt, the second laser pulse hits the sample with the photon energy $h\nu_2$ and excites some of the electrons in the intermediate state into the final state $|f\rangle$ above the vacuum level.

The measured kinetic energy and the emission angle of the photoelectrons after step 3 are used to calculate the energy and the momentum (cf. section 2.2) for the initial and intermediate states by

$$E_i - E_{\mathrm{F}} = E_{\mathrm{kin}} + \phi - h\nu_1 - h\nu_2 \tag{2.9}$$

$$E_k - E_{\mathrm{F}} = E_{\mathrm{kin}} + \phi - h\nu_2 \tag{2.10}$$

Time- and angle-resolved photoelectron spectroscopy (trARPES) is similar to tr2PPE but the photon energies of the laser pulses are in the range of $h\nu_1 < \phi < h\nu_2$. Therefore, this technique measures the temporal evolution of the non-equilibrium electron distribution of the occupied and unoccupied band structure afer irradiation with an intense laser pulse [26]. Figure 2.6 illustrates the process of trARPES.

The biggest difference to tr2PPE becomes evident in step 3. Instead of only probing the electrons in the intermediate state $|k\rangle$, the probe pulse also excites electrons from the occupied initial states $|i\rangle$ into vacuum, which corresponds to conventional ARPES.

By varying the delay line and therefore changing the temporal separation Δt between the pump and the probe pulses, intensity traces with respect to Δt can be analyzed. In figure 2.7a, trARPES data taken with 1.5 eV/15 eV are shown. From the integration range, indicated by the black box, the transient population trace in figure 2.7b is plotted (green circles). We assume that both laser pulses are Gaussian and therefore the cross-correlation of these two pulses again results in a Gaussian (red dashed line). The second characteristic time scale in the transient is linked to the relaxation time of the intermediate state. The transient can be fitted by a

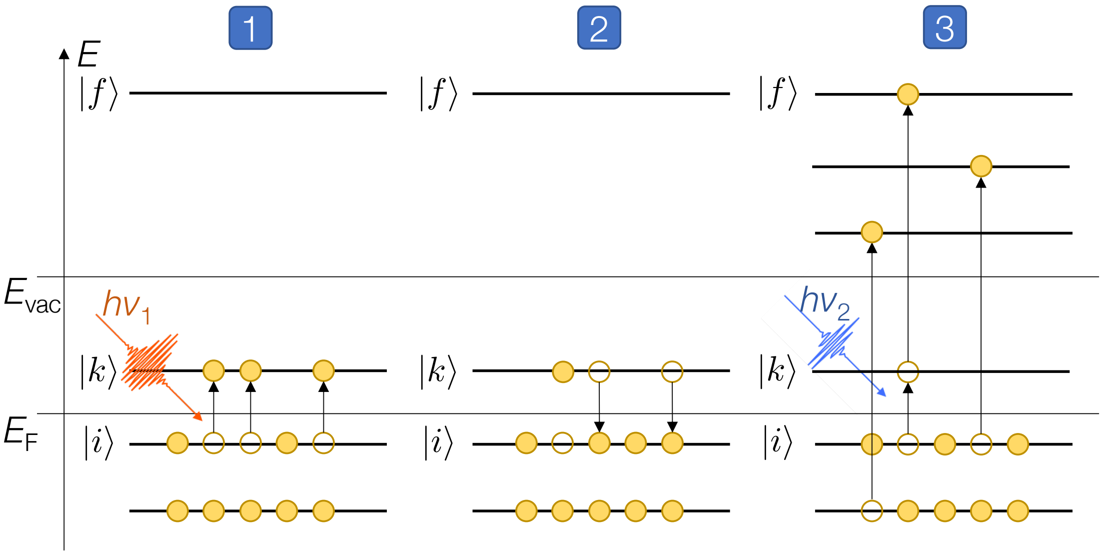

Figure 2.6 Scheme of trARPES. The photon energies of the two laser pulses are $h\nu_1 < \phi < h\nu_2$. Step 1: Irradiation with a short laser pulse $h\nu_1$ excites electrons from the initial state $|i\rangle$ into the intermediate state $|k\rangle$. Step 2: After the excitation, the electrons may relax back to the initial state. All relaxation channels combined define the relaxation time τ. Step 3: After a well defined time delay Δt, a second laser pulse hits the sample and excites the electrons from the intermediate state and the non-equilibrium initial states into the vacuum. The figure is inspired by the "Electron spectroscopies" lecture at University of Zürich.

Gaussian (red dashed line) convoluted with an exponential background (blue dash-dotted line). This leads to the numerical solution with the following fitting function [27]

$$f(t) = A \cdot \sqrt{\frac{2}{\pi}} \cdot \exp\left(\frac{\sigma^2 - 4\tau(t-t_0)}{4\tau^2}\right) \cdot \left(1 + \mathrm{erf}(-\frac{\sigma^2 - 2\tau(t-t_0)}{2\sigma\tau})\right) \tag{2.11}$$

with A as the amplitude, σ from the Gaussian, τ relaxation time, t time delay between pump and probe, t_0 time delay zero and the error function erf.

Unoccupied electronic states are an important aspect to study the electronic properties of solids. The most direct way to observe unoccupied states is inverse photoemission. Ultrashort (femtosecond) pulsed laser systems are another important light source to investigate the unoccupied states by photoemission. The size is ideal for smaller laboratories and femtosecond time resolution is well suited to measure temporal evolution of electronic lifetimes. Most of these laser systems operate in the near infrared regime (photon energies $1 - 1.5\,\mathrm{eV}$) but can be extended up to $7\,\mathrm{eV}$

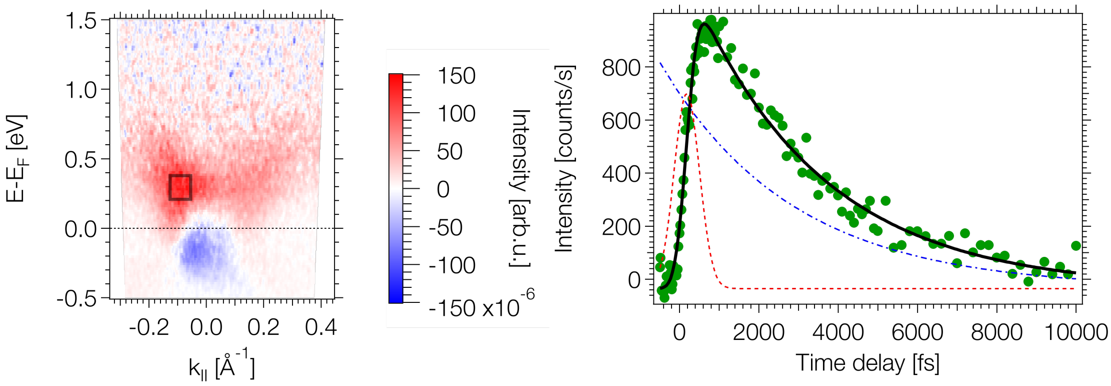

Figure 2.7 Illustration of the fitting routine for transient population traces. Left: trARPES data from Bi_2Se_3 with the black box indicating the integration area for the transient on the right. Right: Experimental transient (green circles) with the fit to the data (black solid line). The fitting function is a combination of a gaussian (red dashed line) and an exponential decay (blue dash-dotted line).

in nonlinear crystal materials. In recent years high-harmonic generation (HHG) became a popular tool to perform trARPES on solids because the photon energy range is increased without losing the temporal resolution.

3 TREx: High harmonics generation and time-resolved photoemission experiment

3.1 Introduction

The goal of this project was to design a table-top high-harmonics generation setup to measure trARPES data at the edges of the first brillouin zone (BZ). A typical brillouin zone diameter is in the range of $k_{\parallel} = 3\,\text{Å}^{-1}$ with a workfunction of roughly $\phi = 5\,\text{eV}$. Therefore, the required photon energy to reach the edge of the BZ is $h\nu = 13.6\,\text{eV}$.

TrARPES experiments require light sources in a pump-probe scheme. Ultrashort (femtosecond) pulsed laser systems are the key tool to perform time-resolved photoelectron spectroscopy and investigate unoccupied states within solids. The size and power consumption are ideal for smaller laboratories and the femtosecond time resolution is well suited to study electronic lifetimes. The main drawback of these setups, where the light paths are placed in air, is the photon energy. The maximum photon energy which can be reached is limited to $h\nu = 6.2\,\text{eV}$ due to the absorption of the light below 200 nm by air. This can be overcome by HHG where photon energies up to a few hundreds of electron volts can be generated. The HHG process is driven by the fundamental laser pulses which are focussed into a noble gas placed in a UHV system. A more detailed description on HHG is given in the following sections.

3.2 Concept of high harmonics generation

For understanding the process of high harmonic generation, one has to consider the physics on two length scales. The first aspect is the microscopic response of an individual gas atom, which can be described quasi-classically by the three-step model developed by Corkum [28]. The second facet is the macroscopic reaction of the nonlinear medium, which combines the coherent sum of the atomic contributions. In this chapter, the theoretical understanding of the HHG process in the microscopic and macroscopic picture is given, and the parameters for the efficient response of the nonlinear medium are evaluated.

3.2.1 Quasi-classical approach: The three-step model

The HHG process is complex and needs a quantum mechanical treatment to be fully described. Perturbation theory holds for low-order nonlinear harmonics where the field intensities of the focussed laser pulses are lower than the atomic electric field. This does not hold anymore when we consider high-order nonlinear harmonic processes. An intuitive description of the latter process can be provided via the quasi-classical three-step model (cf. figure 3.1).

1) Ionization of the gas atom by an electric field resulting in a free electron with $E_{\text{kin}} = 0$.

2) Acceleration of the electron away and back to the atom upon reversal of the driving field.

3) Recombination of the electron with the ionized atom and relaxation to the ground state. The energy gained by the electron is annihilated by the emission of an XUV photon.

Step 1: At the order of $10^{14}\,\mathrm{Wcm}^{-2}$, the field intensities of the focussed laser pulses are large enough to distort the atomic potential and the probability for the electron to tunnel through the potential barrier increases (cf. figure 3.2). After the tunnel ionization, we end up with a free electron with $E_{\text{kin}} = 0$.

At lower field intensities, the tunneling probability of the electron is decreased, and the multiphoton ionization of the electron becomes dominant, i.e. for a large Keldysh parameter [30, 31]

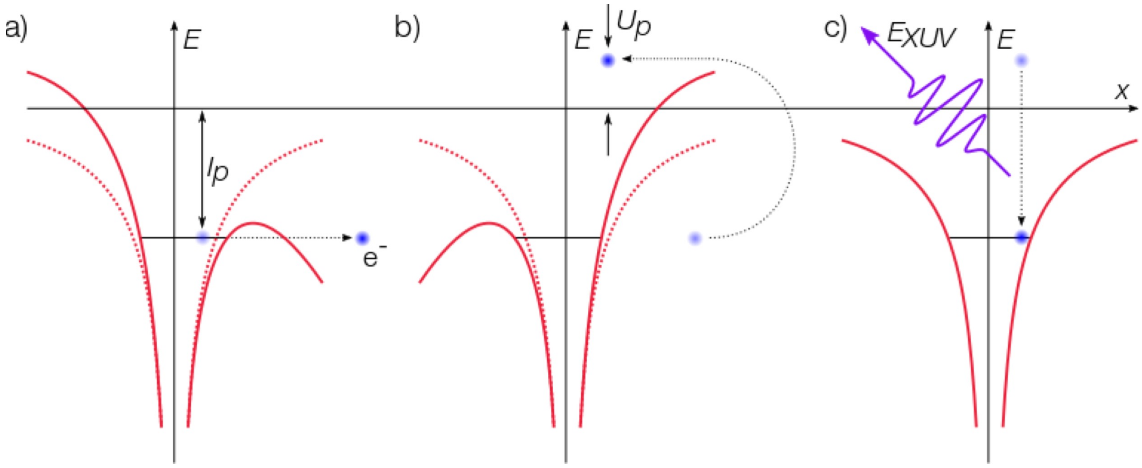

Figure 3.1 Scheme of the three-step model developed by Paul Corkum [28]. The tree steps: **a)** Tunnel ionization of the atom. **b)** Acceleration of the electron in the electric field. **c)** Recombination of the electron with the atom with emission of an XUV photon. Adapted from [29].

$$\gamma = \sqrt{\frac{I_\mathrm{p}}{2 \cdot U_\mathrm{p}}} \tag{3.1}$$

with $\gamma > 1$, where I_p is the ionization potential of the noble gas (e.g. Argon $I_\mathrm{p} = 15.76\,\mathrm{eV}$ [32]) and U_p the ponderomotive energy i.e. the kinetic energy of the electron gained in the driving field (see below equation 3.3).

The third option for the ionization process (cf. figure 3.2) requires even higher field intensities where the atomic potential is distorted heavily so that the Coulomb barrier gets suppressed.

Tunnel ionization is the dominant process for typical laboratory setups where $\gamma < 1$, but the field intensities are still low enough that the suppression of the Coulomb barrier is not yet reached.

Step 2: The electron is accelerated away and back to the atom in the external laser field. The motion of the electron in the field can be described as a free electron accelerated in an oscillating linearly polarized external field, i.e. $E(t) = E_0 \cdot \sin(\omega t)$. The moment of ionization depends on the phase of the laser, and the electron may gain large kinetic energies. Typical kinetic energies are of the order of $10 - 100\,\mathrm{eV}$ therefore no relativistic treatment is required. Directly after the ionization, the velocity vanishes and the position is set to be the origin. The initial conditions are $x(t_\mathrm{i}) = 0$ and $\dot{x}(t_\mathrm{i}) = 0$ where t_i is the time of ionization. Additionally, the electron is supposed to behave like a classical free electron in the electromagnetic field, and we

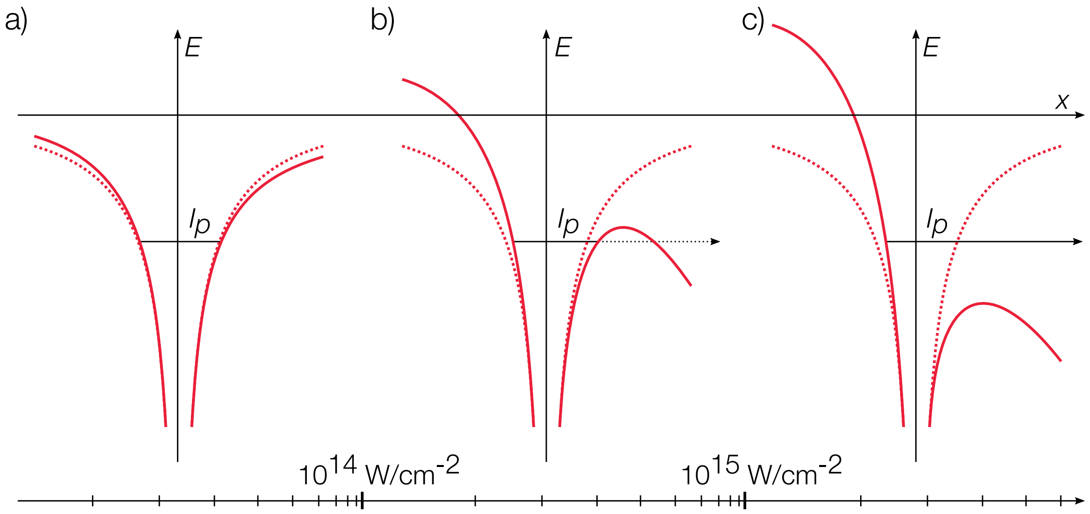

Figure 3.2 Depending on the field intensities of the laser, the gas atom can be ionized by three different processes. **a)** Multiphoton ionization with field intensities below $10^{14}\,\mathrm{Wcm}^{-2}$ and a Keldysh parameter $\gamma > 1$. **b)** Tunnel ionization at field intensities in the order of $10^{14}\,\mathrm{Wcm}^{-2}$ and $\gamma \ll 0$. **c)** High laser fields which suppress the Coulomb barrier. Adapted from [33].

neglect the Coulomb potential of the atom. Therefore the electron can be described by the differential equation [28, 34]

$$\begin{aligned} F = m \cdot \ddot{x}(t) &= -e \cdot E(t) \\ \rightarrow \ddot{x}(t) &= -\frac{eE_0}{m_\mathrm{e}} \cdot \sin(\omega t) \\ \dot{x}(t) &= \frac{eE_0}{m_\mathrm{e}\omega}[\cos(\omega t) - \cos(\omega t_\mathrm{i})] \\ x(t) &= \frac{eE_0}{m_\mathrm{e}\omega^2}[\sin(\omega t) - \sin(\omega t_\mathrm{i}) - \omega(t - t_\mathrm{i}) \cdot \cos(\omega t_\mathrm{i})] \end{aligned} \tag{3.2}$$

where m_e and e are the electron mass and charge, E_0 is the laser field amplitude (the envelope of the laser pulse is assumed to be constant over one cycle) and ω the frequency of the fundamental. The mean energy averaged over one cycle of the laser field is the ponderomotive energy [35, 36]

$$U_\mathrm{p} = \frac{e^2 \cdot {E_0}^2}{4 \cdot m_\mathrm{e} \cdot \omega^2} = \frac{e^2 \cdot I}{2 \cdot m_\mathrm{e} \cdot c \cdot \epsilon_0 \cdot \omega^2} \tag{3.3}$$

with the intensity-field relation of a monochromatic linear polarized electromagnetic wave of $I = \frac{1}{2}cn\epsilon_0{E_0}^2$ and with $n = 1$ in vacuum. Therefore the ponderomotive energy describes the mean kinetic energy ($E_{kin} = \frac{1}{2}mv^2$) of an electron which moves in a sinusoidal field.

Step 3: After the acceleration in the external laser field, the electron may return to the ion and may recombine. The energy lost by the electron when it recollides with the atom is released as an XUV photon. The electron trajectory and the emission of an XUV photon are strongly correlated (cf. figure 3.3). The return energy and the return time are values of great importance for HHG. By investigating equation 3.2 in detail and plotting the electron trajectories for different ionization times as a function of laser cycles, one can get a graphical solution for the maximum energy for the electron and excursion time. The graphical solution for this particular problem was proposed in [37].

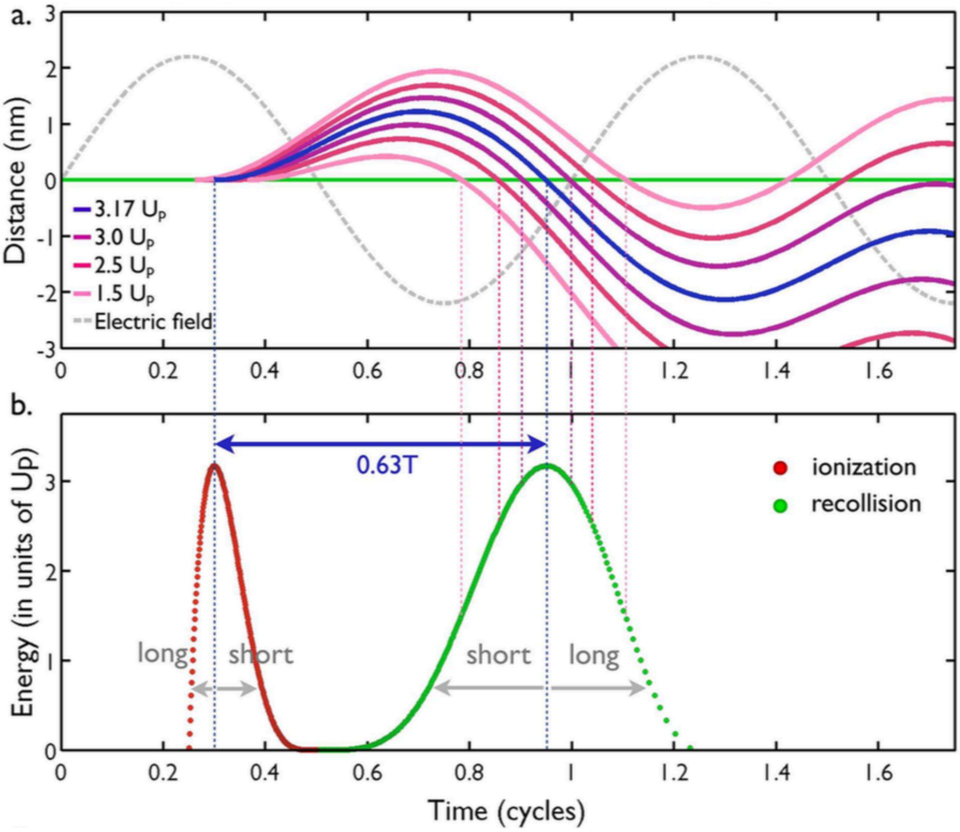

Figure 3.3 **a)** The grey dashed line corresponds to the electric field in arb.u. The solid green line represents the position of the parent ion. The sample electron trajectories for four different recollision energies are presented for laser pulses with a wavelength of 800 nm and a peak energy of 1.57 $\mathrm{Wcm^{-2}}$. **b)** The energy gain of the electron is plotted for the moment of the first collision in a) versus the time in units of laser cycles. The green curve depicts the recollision time whereas the red curve shows the ionization time. 0.63 T corresponds to the mean excursion time of the electron from the moment of ionization to the moment of recollision. The maximum of the green line shows the maximum gained energy of the electron which is 3.17 $\mathrm{U_p}$ and corresponds to the blue trajectory in a). The figure is taken from [38].

From the information from figure 3.3 on the maximum kinetic energy gained by the electron, the cut-off energy E_{cut} for the high harmonic spectrum can be identified to be

$$E_{\mathrm{cut}} = I_{\mathrm{p}} + 3.17 \cdot U_{\mathrm{p}} \tag{3.4}$$

3.2.2 Macroscopic view

The three-step model, introduced in section 3.2.1, describes the response of a single atom of the medium (gas) to a high-intensity field from a laser source. For the macroscopic point-of-view which is important when moving to the application, one has to optimize several parameters to obtain high efficiency. The single atom response does not directly depend on the macroscopic parameters. The macroscopic effects play an essential role in the high harmonic yield, especially when considering low driving field intensities in combination with tight focussing conditions of the fundamental [39].

The yield of the harmonics depends on the phase mismatch of the fundamental and the XUV. By minimizing the phase difference which occurs along the propagation direction of the light the conversion efficiency is maximized since the atoms respond coherently to the driving laser field. The minimization of the phase difference is called phase matching. The phase mismatch between the fundamental and the XUV generated along the propagation direction is described in an article by He *et al.* [40] as

$$\delta\Phi_q(z,t) = \underbrace{\int \Delta k_q(z',t)dz'}_{1)} + \underbrace{q \cdot \arctan(\frac{z}{z_{\mathrm{R}}})}_{2)} + \underbrace{\alpha_j I(z,t)}_{3)} . \tag{3.5}$$

The three terms adding to the phase mismatch have the following origins [29]:

1): The first term accounts for the phase which was accumulated during the propagation of the fundamental and the XUV in the partly ionized nonlinear medium. Δk_q is rewritten as $\Delta k_q = k_{\mathrm{XUV}} - k_{\mathrm{fund}}$ to account for the dispersion within the nonlinear medium due to the presence of neutral atoms and free electrons which all depends on the ionization yield (plasma density).

2): The second term accounts for the focussing of a Gaussian beam which introduces the geometrical Gouy phase. z_R is the Rayleigh length of the fundamental and q is the q-th harmonic.

3): The third term with the driving laser intensity I and the proportionality constant α_j (< 0) which is small (large) negative for short (long) trajectories for a certain harmonic [40–42]. The trajectory depends on the position within the nonlinear medium with respect to the focus of the fundamental. The case where the medium is placed before (behind) the focus along the propagation axis corresponds to longer (shorter) trajectories.

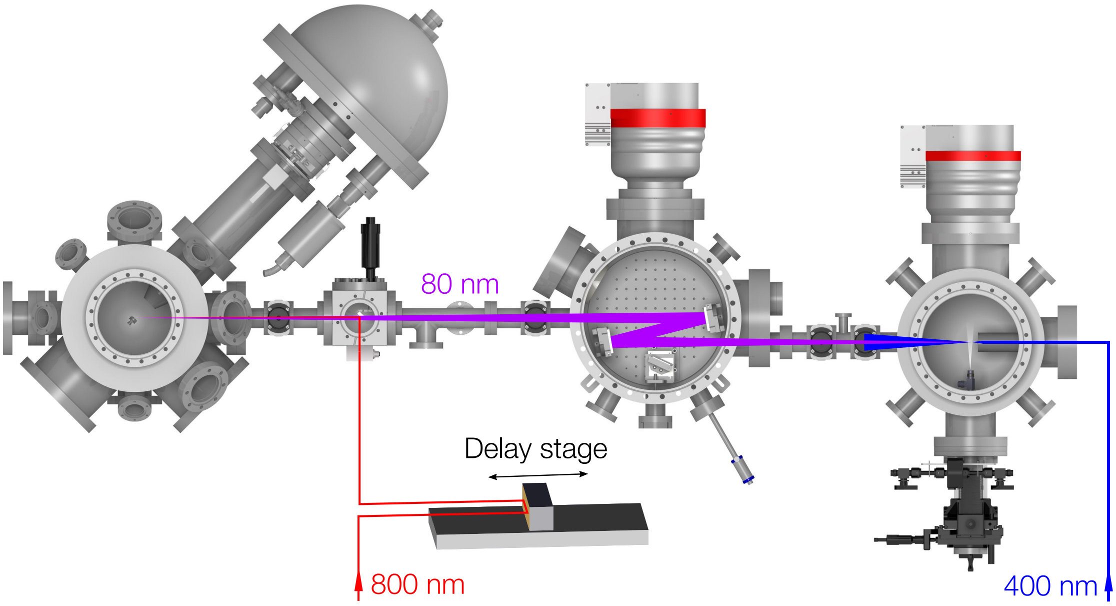

Figure 3.4 Schematics of the HHG setup including the analysis chamber of TREx. Solid lines depict the laser beams for the trARPES measurements. Optionally a BBO can be inserted into the pump line to produce SHG. CATIA drawing and rendering done by T. Kälin.

Tight focussing geometries are typically required for the relatively low pulse energies delivered by high repetition rate systems. In the following paragraphs, the scaling of the experimental parameters is put into perspective for the system built (see figure 3.4) during the thesis [29, 43].

- The laser power that defines the intensities which can be reached within the interaction region. It directly influences the wavevector mismatch $\Delta k_q(z,t)$ because it defines the degree of ionization of the gas medium and the phase which is added up along the propagation direction. See term 1 of equation 3.5

- The focal length f is a scaling parameter for a given beam diameter D. Considering the tight focussing, f is decreasing, the Gouy phase mismatch increases considering the term 2 of equation 3.5 and the corresponding Rayleigh length

$$z_{\mathrm{R}} = \frac{2 \cdot \lambda}{\pi} \cdot \left(\frac{f}{D}\right)^2 \tag{3.6}$$

  becomes smaller. This fact seems to prevent phase matching conditions. However, it is possible to achieve phase matching by scaling the pulse energy E_{f} and the gas pressure p accordingly [39]. The focussing also defines the field intensities in the interaction volume.

- The gas pressure acts directly on $\Delta k_q(z,t)$ since it defines the density within the interaction volume. Another point worth mentioning here is the reabsorption of the XUV by the gas even if it is not relevant for phase matching but the conversion efficiency. For this reason, one uses a low pressure or a small interaction volume to minimize the self-absorption.

The parameters used for the system which is presented here are explained in section 3.5.

3.3 High harmonics generation

3.3.1 Laser System

The light pulses are produced by a commercial femtosecond oscillator (Coherent Mira, 76 MHz) and amplified with a regenerative amplifier (Coherent RegA 9050). The oscillator is a passively mode-locked Kerr-lens Ti:sapphire oscillator, which is pumped by a 5 W pump laser (Verdi V5). The light pulses from the Ti:sapphire oscillator pass a grating stretcher setup (Coherent EC9100) with positive dispersion before seeding the regenerative amplifier which is pumped by a 10.5 W pump laser (Verdi V10). After the chirped pulse amplification (CPA), the pulses are sent back to the compressor to compensate for the initial broadening of the pulses with negative dispersion. The repetition rate can be tuned between $10-300$ kHz. Figure 3.5 shows the laser system. For the measurements with the HHG pulses (cf. section 3.4), the repetition rate is set to 100 kHz which delivers pulses with a wavelength of 800 nm and a pulse energy of $6\,\mu$J. The temporal width of these pulses is 56 fs measured and analyzed with a commercial frequency-resolved optical gating (FROG) setup from Swamp Optics. The spectral width of 27 nm is measured with an optical spectrometer USB2000+UV-VIS from Ocean Optics.

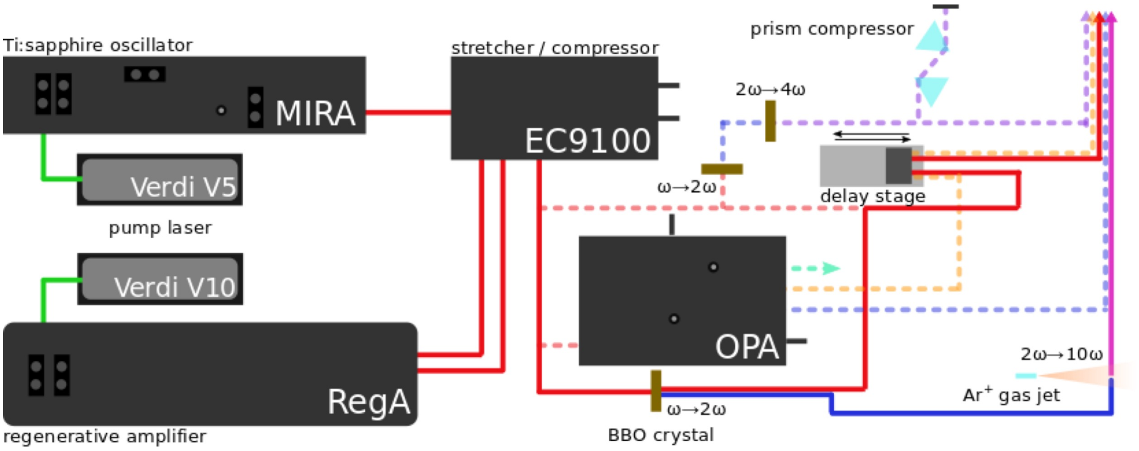

Figure 3.5 Schematic laser setup for the tr2PPE measurements. Three beamlines are available depending on the constraints of the experiment. The dotted lines depict two beamlines which are not essential for this work whereas the solid lines show the setup for the trARPES experiments with the HHG light. Detailed information on the laser equipment can be found in section 3.3.1.

Three different laser beamlines are set up on the optic table to perform trARPES measurements with the photoemission endstation TREx (cf. section 3.4).

1: The laser pulses sent into the optical parametric amplifier (OPA) pass a beam splitter where one beam part is frequency doubled via second harmonic generation (SHG) in a beta barium borate (BBO) crystal and the second beam generates a white light spectrum in a sapphire crystal. Both beams are then focussed into a second BBO where the SHG beam (pump) and the white light continuum (signal) need to be overlapped spacially. The white light is temporally dispersed. The timing and BBO phase matching determine the signal wavelength. Three laser beams are the result of this process which then can be used for experiments. One of them is the signal with a central wavelength between 480 nm and 700 nm, the second one is the remaining of the SHG pump, and the third is the so-called idler which is in the range of 930 −2300nm depending on the signal wavelength.

2: Another setup is 1.55 eV pump and 3.1 eV/6.2 eV probe. Therefore the fundamental is split by a beam splitter where the 800 nm is sent via delay stage as pump to the sample whereas the other beam is used to generate the second (SHG) or fourth harmonic (FHG).

3: The solid lines in figure 3.5 represent the light paths used for the experiments with high harmonics. The fundamental is frequency doubled in a 150 μm thick BBO which is used to pump the Ar^+ gas target with $2\,\mu J$ at 100 kHz. The remaining intensity ($1.5\,\mu J$) from the fundamental after the SHG is guided to the delay stage and then to the solid in the analysis chamber to pump the sample.

3.3.2 HHG chamber

The HHG chamber is the first chamber of a series of three chambers where the SHG beam of the table top laser system is fed into UHV. Three important aspects need to be considered to design this chamber.

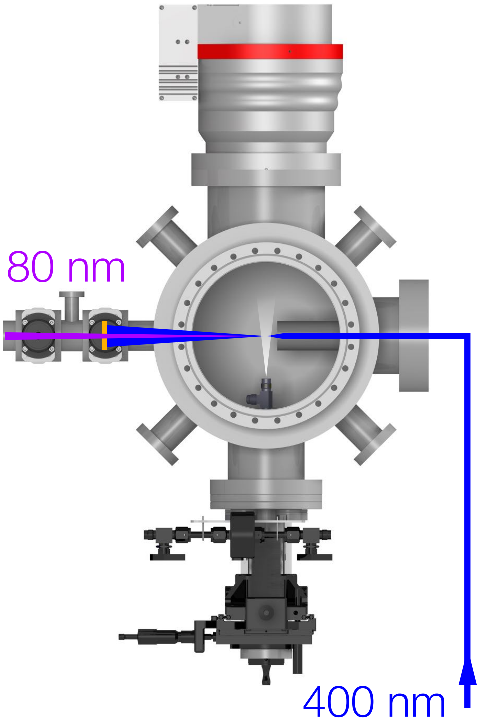

Figure 3.6 The HHG chamber with the second harmonic (400 nm) used to generate the 10^{th}-harmonic (80 nm) in Ar^+ gas. The second harmonic is blocked by a 200 nm think Indium filter (orange color) mounted in a CF40 VAT valve. CATIA drawing and rendering done by T. Kälin.

Focussing: The process of HHG is driven by large electric fields within the interaction volume of the light and the noble gas (cf. section 3.2). Larger fields can be generated by harder focussing of the beam. The current setups are divided between loose [44] and tight [39] focussing versions. The relatively low pulse energy delivered by our setup requires a tight focussing geometry. Different combinations of glass nozzles and lenses were tested (cf. table 3.1) to find an optimal combination of gas-

Focal length f	**Nozzle diameter** d	**Sample current** I	**Pressure** p
50 mm	50 μm	0.15 nA	$1.6 \cdot 10^{-3}$mbar
75 mm	50 μm	0.04 nA	$1.6 \cdot 10^{-3}$mbar
50 mm	25 μm	0.012 nA	$5.9 \cdot 10^{-4}$mbar
38 mm	25 μm	0.005 nA	$5.9 \cdot 10^{-4}$mbar

Table 3.1 Test of the HHG efficiency with different lens and nozzle combinations. For all combinations a pulse energy of 1.6 μJ was used.

light interaction volume and focal length. In our present setup, the 400 nm pump beam is focussed with a fused silica (FS) lens $f = 50$ mm.

Gas jet: Gas filled capillary waveguides [45] and gas jet forming glass nozzles [46] are currently the main tools to form a dense gas-light interaction volume. The choice depends mostly on the focussing geometry. A loose focussing version generates bigger Rayleigh length (cf. section 3.2, equation 3.6). Therefore the gas volume needs to be larger along the light propagation axis where a gas-filled capillary waveguide is the best choice. The tight focussing geometry from our setup requires a smaller interaction volume considering the Rayleigh length of $z_{\mathrm{R}} = 40\,\mu$m. By testing multiple different cylindrical glass nozzle sizes as mentioned in the latter paragraph, the highest conversion rate achieved was with a nozzle opening diameter of 50 μm at backing pressures of the order of 2.5 bar.

Pumps: The pressure difference between the mirror chamber and the HHG chamber needs to be enough not to damage the 200 nm thin Indium foil placed in the window mount of the VAT valve separating the two chambers and to prevent the XUV to be reabsorbed after generation. A Pfeiffer HiPace 700P without Holweck stage to prevent overheating due to the pumping of the Argon gas pumps the HHG chamber with a pumping speed of 665 ls^{-1}. During the generation of high-harmonics the operating pressure is $\sim 10^{-3}$ mbar and in the mirror chamber $\sim 10^{-9}$ mbar.

3.3.3 Mirror chamber

The mirror chamber could also be called monochromator chamber since the comb of several discrete photon energies produced by the HHG process needs to be filtered to have only one harmonic to be focussed on the sample.

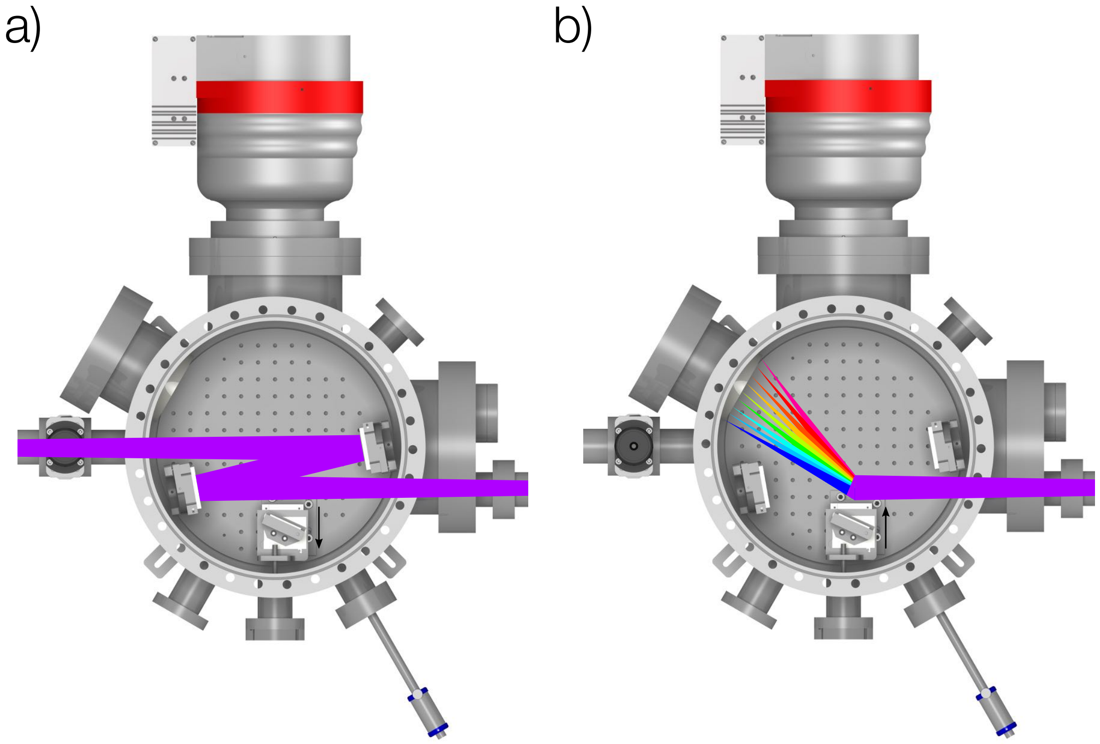

Figure 3.7 Mirror chamber with HHG beam on **a)** the multilayer mirrors to guide the light to the sample in the analysis chamber. **b)** The diffraction grating can be moved into the beam path to redirect the harmonics onto the PSD. CATIA drawing and rendering done by T. Kälin.

Toroidal diffraction grating and position sensitive detector (PSD): By reflecting all the harmonics (cf. section 3.2) from a toroidal diffraction grating onto a PSD (x-y resolved detector) one can record the spatially resolved harmonics [47]. The PSD consists of a Copper resistive anode with x-y resolution and a micro channel plate (MCP) to amplify the signal. The information obtained is used to check which harmonics are generated and the intensity of the individual harmonics.

Mirrors: The simplest way to obtain a spectral selection of the harmonics is via multilayer (ML) mirrors [48]. At normal incidence of the light the time duration of the pulse does not change up to few femtoseconds [49], but it has a disadvantage of the spectral selectivity requiring multiple sets of mirrors to cover the whole spectral range if the setup delivers a large spectrum. It has been shown that ML mirrors can be designed to be tuned and therefore act as a tunable monochromator [50]. Another version is the time-preserving monochromator [51] with one grating to have spectral selectivity and a minimum of temporal broadening. A more complex version is the time-delay compensated monochromator where at least two diffraction gratings in subtractive configuration compensate for the dispersion [52]. Because the selection for many harmonics is not the case for us we employed two ML mirrors in a Z-configuration optimized for maximum reflectivity at 80 nm and a reflection angle of 14.5° at each mirror.

Mirror holders: The mirror holders mounted in the mirror chamber are electronically motorized tip-tilt optical mounts for 2-inch optics from SmarAct. The tip-tilt directions can be controlled from outside the chambers with a control unit without breaking the vacuum. The alignment can be optimized by observing the PES signal.

3.3.4 Detection of XUV

The XUV detection and characterization is done via reflection from a diffraction grating onto the PSD which is a suitable tool to spatially disperse and allows the individual intensities of the harmonics to be determined. The reflection angle on the toroidal diffraction grating used in our setup is shown in figure 3.8. By knowing the incidence angle on the grating and the position on the PSD, the harmonic number can be determined. The harmonic order as a function of the incidence α and diffraction angle β can be written as

$$mN\lambda = \sin(\alpha) + \sin(\beta) \tag{3.7}$$

where m is the diffraction order, $N = \frac{1}{d}$ the inverse grating constant (here $1100\,\mathrm{mm}^{-1}$) and λ is the wavelength. The second equation used for the grating is $-\alpha + \beta = 142\,^\circ$ with $-\alpha_0 = \beta_0 = 71\,^\circ$ for zero order.

In everyday usage of the HHG setup and because a single HH is generated it would be redundant to tune the flux of the XUV from the HHG by observing the signal on the PSD. Therefore we installed an aluminum target on a linear drive which is then connected to a picoamp meter. The target can be moved in and out of the beam to conveniently monitor the sample current resulting from the XUV hitting the target while adjusting the parameters influencing the phase matching of the HHG process.

The detection of the XUV and the procedures to overlap the pump and the probe beam for the time-resolved photoelectron spectroscopy in the AC will be explained in detail in section 3.5.1.

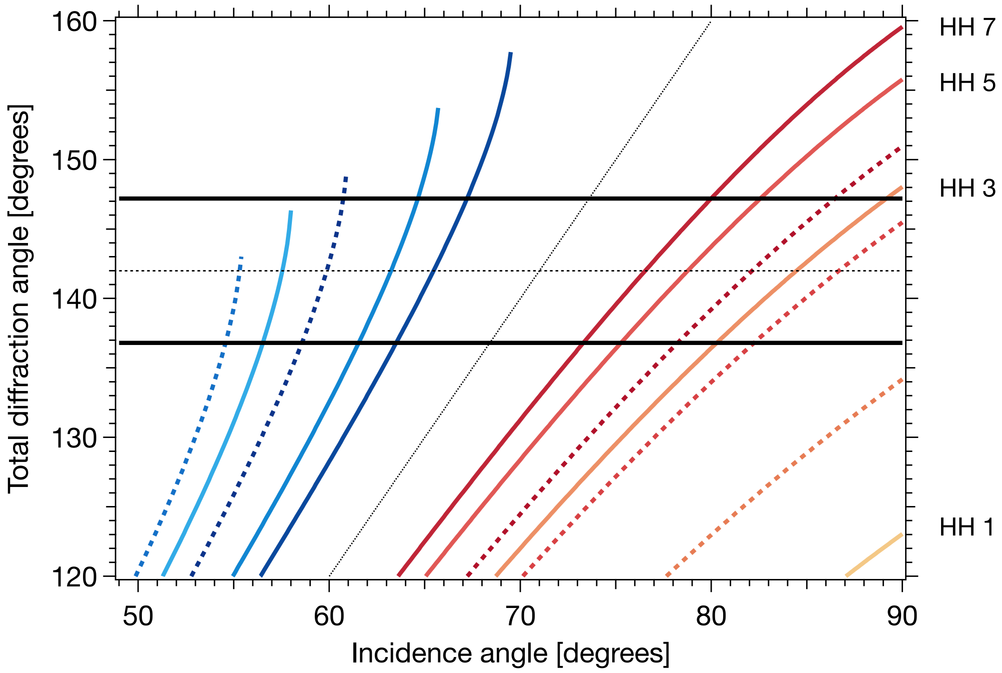

Figure 3.8 Reflection of several harmonics from the toroidal diffraction grating onto the PSD as a function of the incidence angle of the light onto the grating. The black solid lines enclose the window of detection of the PSD. The harmonic order of the light can be distinguished by varying the incidence angle. Different high-harmonic (HH)s are displayed for various diffraction orders. The first order HHs which are detected with the PSD are indicated in the figure.

3.4 Photoemission endstation: TREx

The main goal of this thesis was to build a new photoemission endstation combined with an HHG light source to perform trARPES experiments covering the first SBZ of solids in reciprocal space. The endstation constructed during this thesis is named TREx (time-resolved experiment) and it consists of three main chambers. Figure 3.9 shows a rendering of TREx.

Load lock (LL): The LL is the sample entry lock chamber to introduce the sample from air to ultra high vacuum (UHV). It is vented to bring new samples to the UHV system and pumped down with a turbo molecular pump (TMP). It consists of a simple CF63 cube with a linear transfer arm (three sample positions) attached to transfer the sample into the preparation chamber.

Preparation chamber (PC): The PC is used to prepare the samples for the experiment. It is equipped with two sample positions on a long linear transfer arm to transfer the samples into the analysis chamber. The sample holders can be fixed on the positions to cleave them but also clean the surfaces by repeated Ar^+

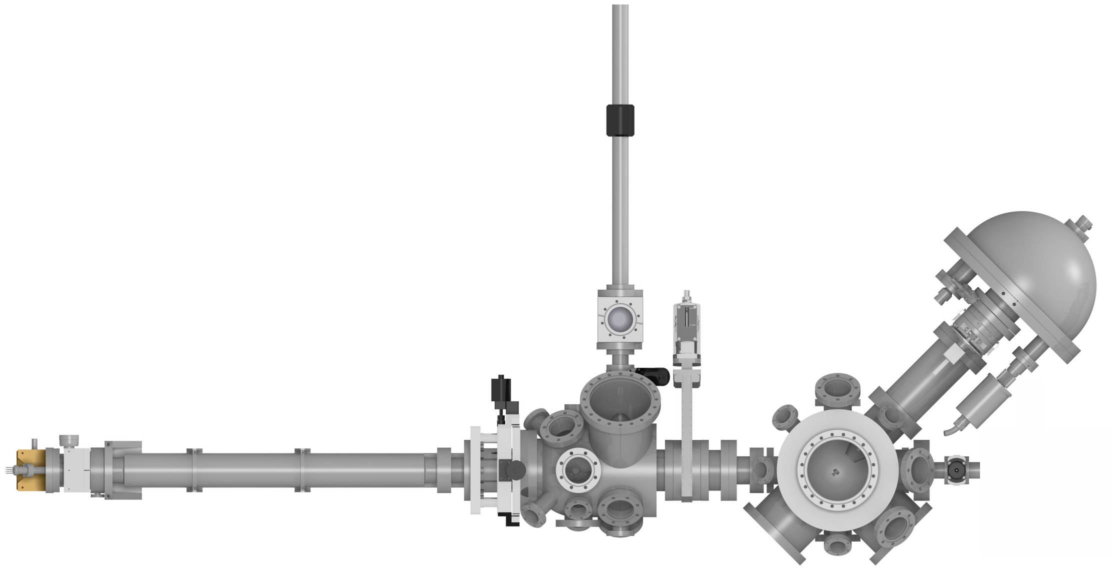

Figure 3.9 Illustration of TREx with the three main chambers: Load lock, preparation chamber and analysis chamber. CATIA drawing and rendering done by T. Kälin.

sputtering and anneal cycles. Monolayers of boron nitride can be prepared, and the samples can be treated with various gases like, e.g. oxygen. Low energy electron diffraction (LEED) can be done to check the surface quality of the preparation.

Analysis chamber (AC): The main chamber of the photoemission endstation is the AC where the measurements on the sample are performed. The home-built five-axis sample goniometer of the manipulator allows sample orientations in any arbitrary direction. With this manipulator, emission in any direction in the full hemisphere above the sample can be mapped. The sample can be biased by applying a voltage, and the photoelectron yield can be determined by recording the sample current. A SPECS Phoibos 100 photoelectron analyzer records the trajectories of the photoelectrons emitted from the solid.

By combining the HHG with T-REx, we obtain a powerful setup for trARPES measurements. In figure 3.13 a rendering of the complete setup is shown. In the HHG chamber the 5th harmonic of the driving laser ($\lambda = 400\,\text{nm}$) is generated and passes through a 200 nm thick In filter (cf. figure 3.10) which is placed in the window socket of a VAT valve to block the second harmonic. The purpose of the metallic window is two-fold. It blocks the 400 nm light and separates the HHG chamber and the mirror chamber so that a pressure difference from 1.5×10^{-3} mbar to vacuum can be reached [53].

The divergent XUV light is collimated on a first, spherical mirror and focussed

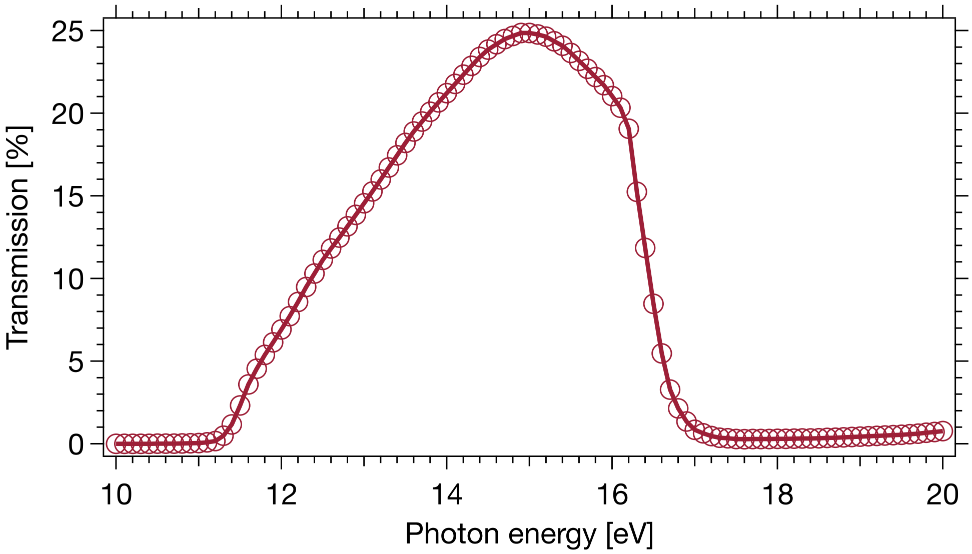

Figure 3.10 Transmission curve for a 200 nm thick indium foil. Transmission window 12 − 16 eV with a transmission of 25 % at 15 eV. Data taken from [54].

on the sample in the AC by a second, toroidal mirror. The design of the ML mirror combination is done in collaboration with OptiXfab [55]. The best mapping performance is given for a toroidal-spherical mirror combination (cf. figure 3.11) which images a 1.42 μm source spot onto a circle of 2 μm diameter on the target thus a slight magnification of about 1.4 occurs.

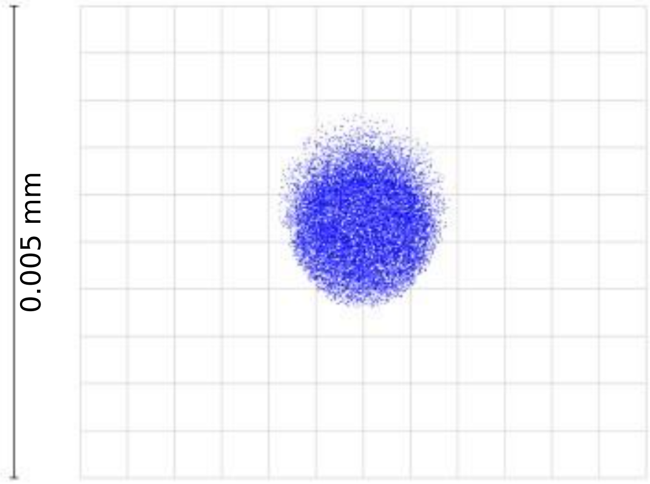

Figure 3.11 Zemax OpticStudio ray-tracing calculations done by OptiXfab for a spherical-toroidal mirror combination. The mapping performance is done assuming a source size spot of 1.42 μm. The spot size on the target is simulated to be 2 μm. The real final spot profile is obtained by convoluting the true source profile with this spot profile resulting in a source magnification of ~ 1.4.

The reflectivity of the XUV ML mirrors was measured at the Physikalisch-Technische Bundesanstalt (PTB) to be 33 % for 15 eV (82 nm). Considering the transmission of 25 % through the indium thin film and the reflectivity of the XUV ML mirrors the transmission of the full beamline is about 3 %.

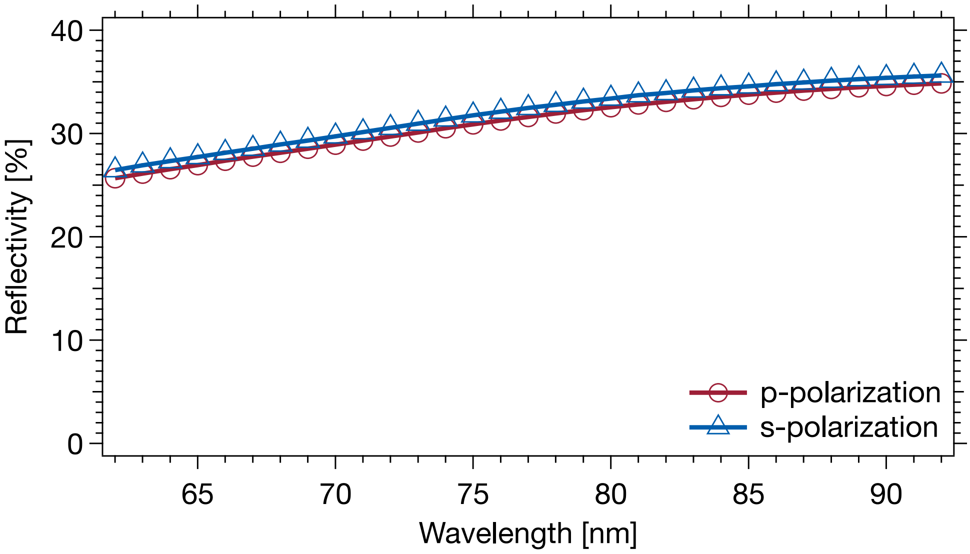

Figure 3.12 Reflectivity curves measured at Physikalisch-Technische Bundesanstalt (PTB) by OptiXfab for the XUV mirrors used in this setup. The angle of incidence for these measurements was 7°.

The third chamber of the HHG setup is the connection between the HHG and TREx. It is a simple CF63 UHV cube which is separated from the AC by a pneumatic VAT gate valve which also acts as a security valve in case of a pressure burst due to damaging of the In foil. The pump beam for the tr2PPE measurements enters the cube and is reflected on a D-shape broadband mirror which covers a range of 200 − 1100nm with a reflectivity of at least 80 % for the whole range. The pickup mirror is mounted on a home-built linear transfer to position the mirror as close as possible to the XUV beam without cutting. The goal is to have the pump and the probe beam collinear which is not easy to achieve because of the strong divergence of the XUV beam with a diameter of about 10 mm close to the D-shape mirror. The smallest deviation for both beams can be realized by bringing the D-shape mirror close to the XUV beam and placing the pump beam close to the edge of the broadband mirror.

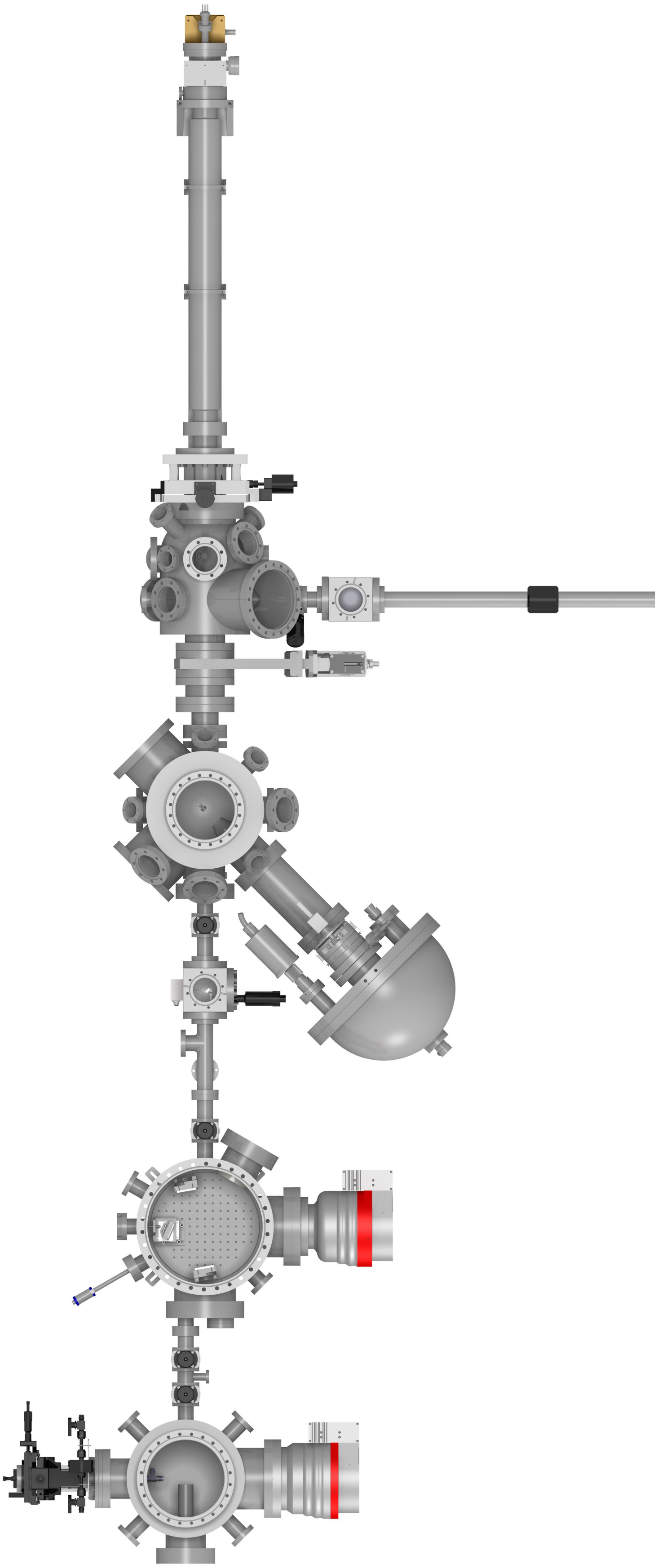

Figure 3.13 Illustration of the photoemission endstation: TREx. CATIA drawing and rendering done by T. Kälin.

3.5 Commissioning: HHG and TREx

The second harmonic seeding the HHG delivers $2.8 \cdot 10^{17}\gamma/\mathrm{s}$. The photon flux in the XUV beam (assuming a quantum efficiency of 10^{-1} [56]) is estimated at $1.3 \cdot 10^{10}\gamma/\mathrm{s}$ by measuring the sample current on the aluminum target placed in the mirror chamber. Considering a transmission of 25 % through the In filter, $5 \cdot 10^{10}\gamma/\mathrm{s}$ are generated. This then leads to a conversion efficiency of $1.8 \cdot 10^{-7}$ which is in line with the reported conversion efficiencies of a single harmonic generated in argon [39, 46, 57].

The number of photons per second on the sample surface can then be found by considering the reflectivity of the XUV mirrors (cf. figure 3.12) of 33 %. We obtain about $5.5 \cdot 10^{9}\gamma/\mathrm{s}$ (or $5.5 \cdot 10^{4}\gamma/\mathrm{pulse}$) on the sample surface.

3.5.1 Spatial and temporal overlap

Pump-probe measurements require spatial and temporal overlap of the laser pulses. Therefore two samples are mounted on the manipulator in the AC to overlap the pulses. The first one is a YAG crystal to do the spatial overlap and the second one is a GaAs(111) sample to find the temporal overlap.

Spatial overlap: By integrating for 30 s with a CCD camera which is attached on the AC the XUV spot of the HHG on the fluorescent YAG crystal can be recorded (cf. figure 3.14). This spot can be marked, and the pump (e.g. 800 nm) spot can then be moved onto the same spot to achieve spatial overlap. The size of the beam spots can be measured in pixel, and with the help of a reference size in the chamber, the pixel can be converted to μm. The spatial overlap can be optimized on GaAs once the temporal overlap is determined.

Temporal overlap: GaAs is useful to find the temporal overlap for a tr2PPE setup. We denote this position of the delay line by t_0 (time delay zero). Delay scans on the GaAs sample with the 800 nm (or 400 nm) pump and 400 nm driving laser from the HHG as probe, the delay line position when both pulses hit the sample simultaneously (t_0) can be determined (cf. figure 3.15). This is a quick method to find a new time zero in case dispersive elements, e.g. lenses, waveplates,... are inserted into the beamline and therefore t_0 shifts. Time zero can be determined with a precision of roughly 50 fs. However, this method of femtosecond absorption saturation [58] on the GaAs sample cannot be applied with XUV since the valence bands (light hole and heavy hole bands) close to the Fermi energy are not visible

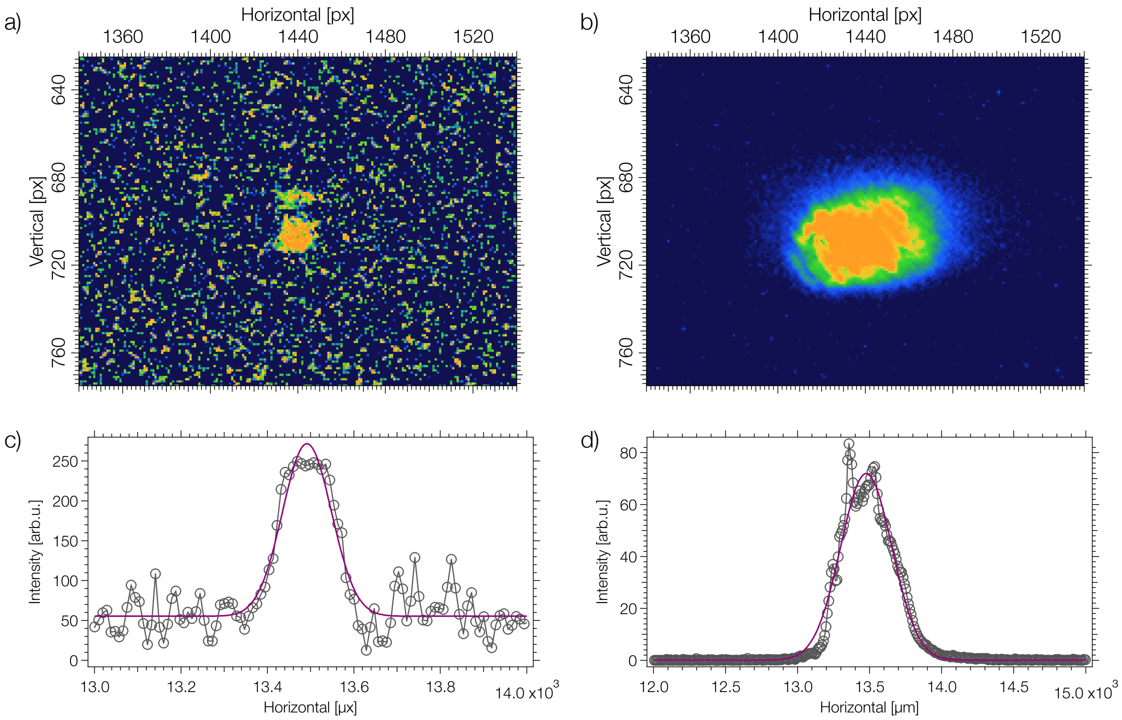

Figure 3.14 CCD camera recordings of the **a)** XUV and **b)** 800 nm pump spot on the YAG crystal. With the conversion of $[\mu m] = 9.4 \cdot [px]$ a FWHM spot size of $133 \pm 7\mu m$ ($2\omega = 226 \pm 11\mu m$) for the **c)** XUV and a FWHM spot size of $419 \pm 5\mu m$ ($2\omega = 712 \pm 9\mu m$) for the **d)** 800 nm pump beam spot are calculated where 2ω denotes the full width at $\frac{1}{e^2}$.

at the XUV wavelength used. The temporal overlap for the 800 nm pump and XUV probe is done with the 800 nm and the 400 nm driving laser of the HHG on GaAs. The generation of high harmonics is not assumed to shift time zero which is verified by measuring transients on the topological insulator Bi_2Se_3 which shows a long living surface state (lifetime of 10 ps) which can be effectively pumped with infrared radiation (IR). A detailed section on Bi_2Se_3 can be found in chapter 5.

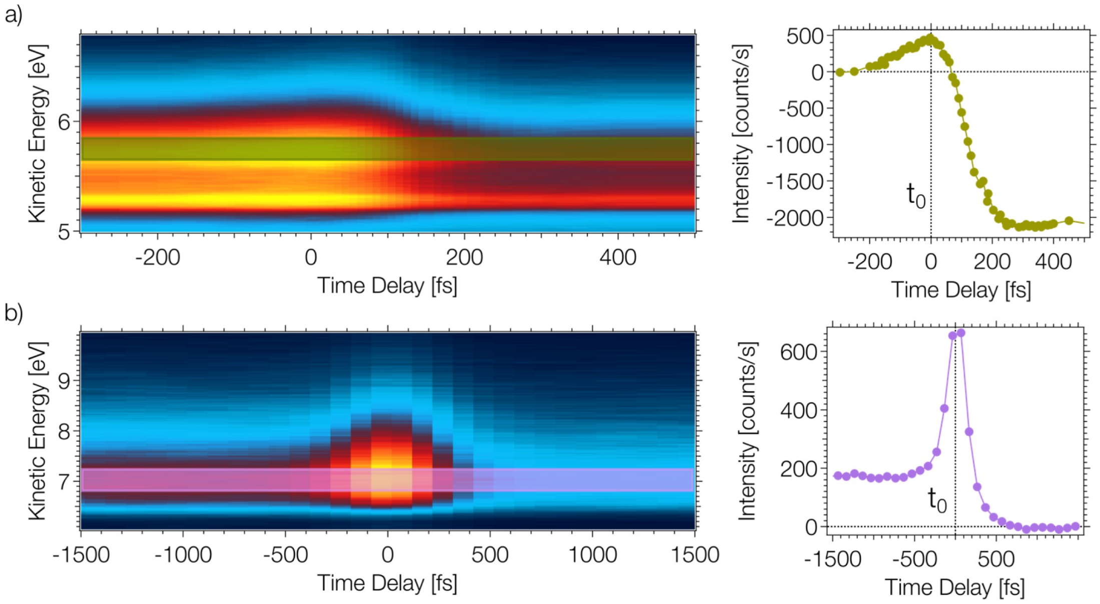

Figure 3.15 Time traces recorded in a pump(λ_1)- probe(λ_2) scheme with **a)** $\lambda_1 = 800\,\mathrm{nm}$, $\lambda_2 = 400\,\mathrm{nm}$ and **b)** $\lambda_1, \lambda_2 = 400\,\mathrm{nm}$ on GaAs(111). *Left:* Energy-distribution curves (energy-distribution curve (EDC)) integrated over the full angluar window of the spectrometer (cf. section 3.4) plotted versus the time delay between the pump and the probe pulse. Integration time per delay point was 7 s and 1 s respectively. *Right:* Time traces of the integration windows indicated in the EDCs on the left side. Time zero (both pulses arrive at the same time) is marked as t$_0$.

3.5.2 Energy resolution

After the installation of the XUV mirror pair, a first static measurement was done on Cu(111). The choice for this specific single crystalline metal has two reasons. It is easy to prepare since it only requires a few sputter and anneal cycles [59]. It also has a sharp Shockley type surface state (SS) with an FWHM of 70 meV [60] at room temperature. The energy resolution for our light source could be calculated from the line width of the surface state to be $\Delta E = 198 \pm 3\,\mathrm{meV}$ and is displayed in figure 3.16.

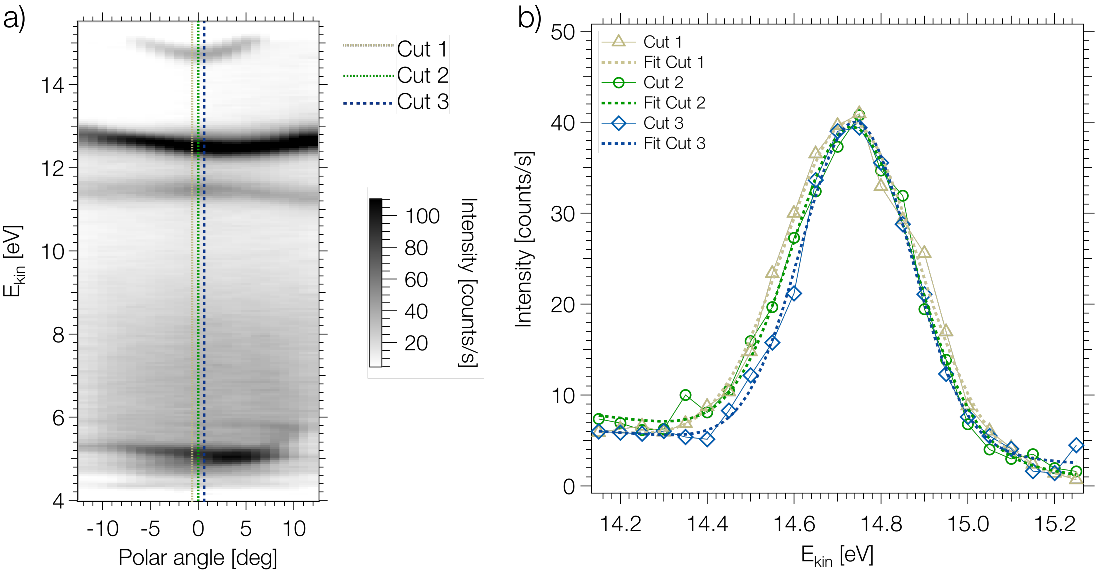

Figure 3.16 Static ARPES data acquired with XUV photons from Cu(111) after installation of the first mirror pair. **a)** ARPES spectrum of Cu(111) integrated over 7 min. The three lines indicate the cut positions for the spectra in b). **b)** Energy cuts for three different slices around normal emission focussed on the surface state. A gaussian fit with a linear background was used to fit the data. The full width half maximum (FWHM) for all three spectra including the errors were calculated. The energy resolution of $\Delta E = 198 \pm 3\,\text{meV}$ is then extracted by the arithmetic mean of all three FWHM.

3.5.3 Temporal resolution of IR pump - XUV probe

The determination of the temporal resolution of the experiment is a critical parameter. A standard procedure to define a pulse duration is to measure the dynamics of hot electrons on a metallic surface. The cross-correlation signal from the trARPES can be fitted by a Gaussian where the time resolution of the experiment can be determined. The fluence of the pump laser beam needs to be in the range of $30\,\mu\text{Jcm}^{-2}$ to generate hot electrons [61]. This experiment has been performed on an Au poly surface which has been sputtered to remove residual atoms on the surface.

It was not possible to detect a hot electron gas with a pump-probe scheme even by pumping the sample with $500\,\mu\text{Jcm}^{-2}$. The best estimation of the time resolution for the present setup is evaluated on the bulk conduction band of Bi_2Se_3. The electrons from the valence bands are excited into the bulk conduction band at higher kinetic energy and relax energetically towards the bottom of the bands [62]. The time traces of the electron dynamics at 0.7 eV above the Fermi energy can be fitted with a Gaussian convoluted with an exponential (cf. equation 3.8) where we can deduct the FWHM of the Gaussian. The fitting function is

$$f(t) = A \cdot \sqrt{\frac{2}{\pi}} \cdot \exp\left(\frac{\sigma^2 - 4\tau(t - t_0)}{4\tau^2}\right) \cdot \left(1 + \mathrm{erf}(-\frac{\sigma^2 - 2\tau(t - t_0)}{2\sigma\tau})\right) \tag{3.8}$$

with A as the amplitude, σ from the Gaussian, τ decay time, t time delay between pump and probe and t_0 the mean of the Gaussian.

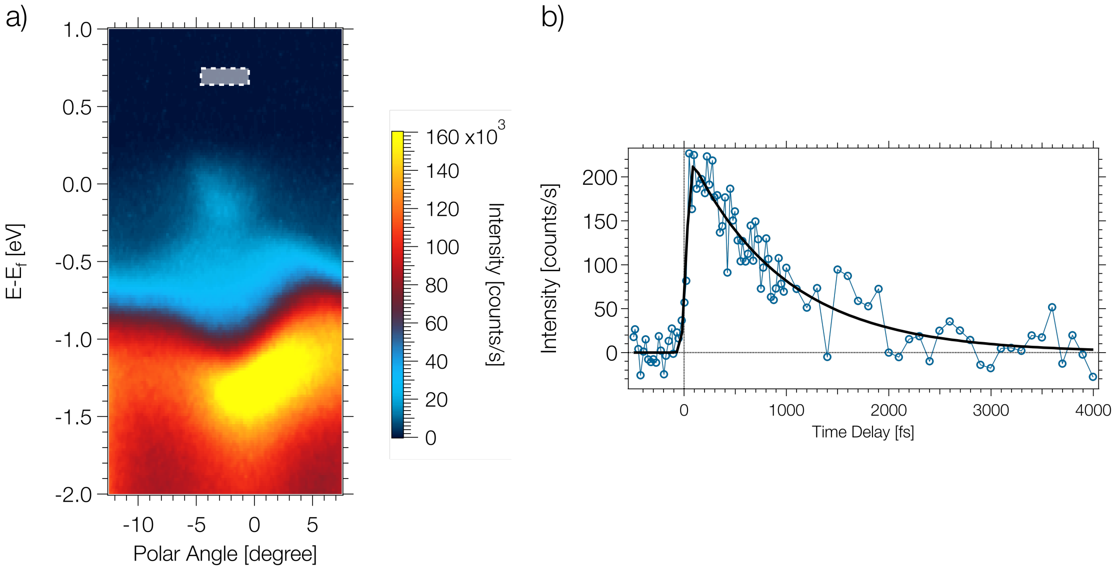

Figure 3.17 Temporal resolution of the pump-probe experiment with IR and XUV. **a)** 800 nm pump and XUV probe measurement. Integration window (white box) at 0.7 eV above E_F covers a height of 100 meV and a width of 4 °. **b)** Time trace from the integration window indicated in a). The time trace is fitted with a gaussian convoluted with an exponential (cf. equation 3.8) where the resulting FWHM of the gaussian is 103 ±26 fs.

3.6 Conclusions

The main objective of this thesis was the design and implementation of a high harmonic generation light source at high repetition rates to perform time- and angle-resolved photoelectron spectroscopy experiments.

The 5th harmonic of the driving laser with a photon flux of $5.5 \cdot 10^4 \gamma$/pulse at 100 kHz repetition rate and a photon energy of 15 eV could successfully be generated in Ar^+ gas. For this purpose, the second harmonic of an amplified Ti:sapphire oscillator was focussed into the noble gas acting as driving field for the high harmonic generation process. The remaining fundamental after the second harmonic process is diverted over the delay stage and brought to overlap with the high harmonic on the sample. Together with the hemispherical electron analyzer, a working setup to perform time-and angle-resolved photoelectron spectroscopy with 100 fs time-resolution could be implemented.

4 h-BN/Ni(111)

4.1 Introduction

Hexagonal boron nitride (h-BN) is the most common crystalline form of boron nitride [63]. It consists of alternating boron (B) and nitrogen (N) atoms in a stoichiometric ratio of 1 : 1 and is isomorphic to graphite [64]. It has remarkable properties like, e.g. high chemical inertness, large resistance to corrosion and high thermal conductivity. Nowadays it is widely used in the industry in high-temperature applications ($T_m > 3000\,\mathrm{K}$) or as electrical insulator.

H-BN can be grown by chemical vapor deposition (CVD) as a two-dimensional honeycomb layer on various metals like rhodium, nickel, palladium, ruthenium or platinum. [65, 66]. Under UHV conditions boron nitride grows as a self-assembling monolayer. Depending on the substrate and on the lattice constant of the material, h-BN grows as flat [67] or as a corrugated layer. The latter was named nanomesh [68]. This large band gap insulator offers interesting properties to study materials which can be deposited on top of the multi and monolayer boron nitride like graphene [69, 70]. The adsorption geometry of a monolayer h-BN/Ni(111) and the valence band structure were studied by means of x-ray photoelectron diffraction (XPD) and ARPES [67]. Tr2PPE experiments revealed a long living interface state in between the Ni(111) substrate and the h-BN single sheet [24]. On a metal substrate, it is a two-dimensional material with a band gap of roughly 6 eV. The band gap of h-BN on metallic substrates is expected to be indirect [71]. So far the π^*-band of h-BN/Ni(111) was only observed by means of inverse photoemission spectroscopy [72]. The system h-BN/Ni(111) was chosen as a possible candidate for valleytronics because the h-BN layer is flat [73] which minimizes umklapp scattering effects and at the $\overline{\mathrm{K}}$-point of the surface Brillouin zone (SBZ) a valley in the unoccupied π^*-band is expected [16].

4.2 Preparation and Characterization

4.2.1 Preparation of h-BN/Ni(111)

In this section, the preparation and characterization of h-BN on Ni(111) is shown. All preparation steps were performed in UHV at a base pressure of $8 \cdot 10^{-10}$ mbar. The characterization and quality check of h-BN/Ni(111) was done by means of UV photoelectron spectroscopy (UPS), ARPES, XPS and XPD.

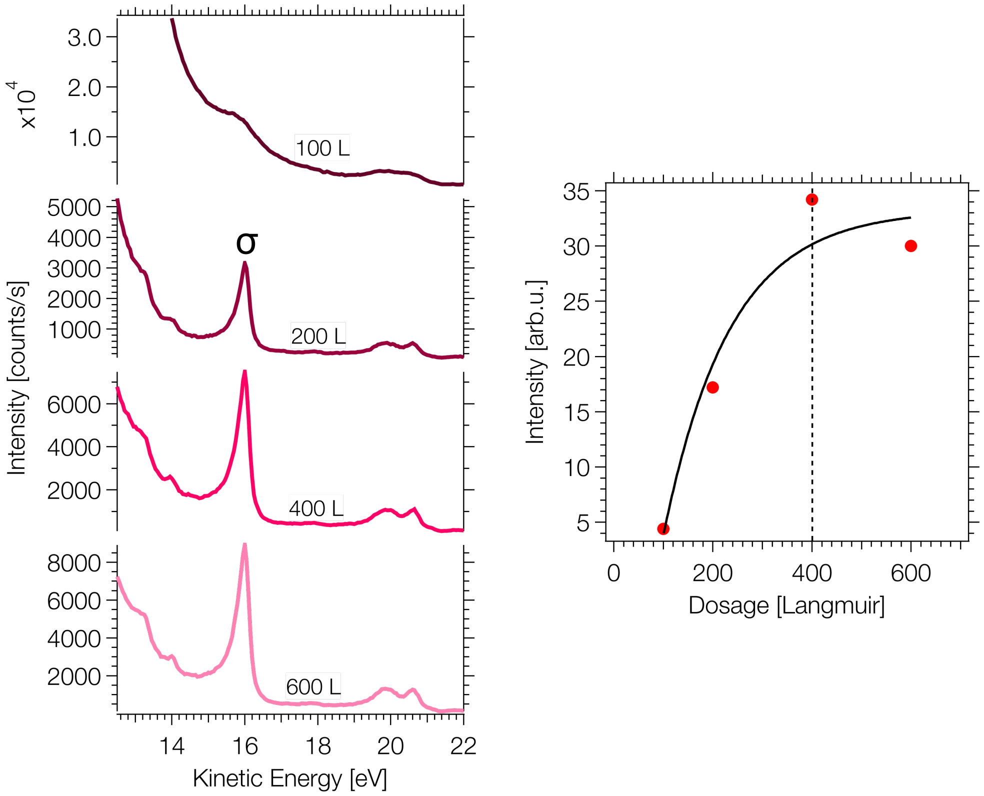

Figure 4.1 Left: UPS spectra with He Iα measured at T-REx to determine the amount of borazine needed to prepare a monolayer of h-BN on Ni(111). Right: Peak integrals of the σ-band of h-BN as reference for different dosages. The σ-band is indicated in the UPS spectra.

In a first step, the single crystalline metal substrate is cleaned by repetitive cycles of sputtering and annealing. The sample surface was sputtered with Ar^+-ions (500 V) for 20 min and subsequently annealed at 1070 K. In order to remove residual carbon, the cleaning of the Ni(111) was done with oxygen dosing (1 L) cycles in between the sputtering and annealing which binds the carbon and is removed more easily. From the XPS spectrum shown in figure 4.2 the contamination of the sample surface could be determined to be below 1 %. After the cleaning steps, the sample was held at 1070 K for the deposition of boron nitride. The liquid (borazine $B_3H_6N_3$) is stored in a home built-glass vial which is constantly cooled by a Peltier cooler. The Ni(111) surface is exposed to borazine vapor at a pressure of $4 \cdot 10^{-7}$ mbar for 20 min to grow a monolayer of h-BN. The amount of borazine which needs to be dosed depends on different factors but especially on the temperature reading. The growth of h-BN on a metal substrate by self-assembly is self-terminating after 1 ML. The UPS spectra for different dosages are shown in figure 4.1. The intensity of the characteristic σ-band in normal emission does not increase once a full monolayer has grown. and a work function of ~ 3.6 eV is reached. In the TREx preparation chamber, a dose of 400 L was calculated.

4.2.2 Chemical analysis

After the cleaning of the Ni(111) substrate the sample was checked with XPS for residual contamination by carbon (C) and oxygen (O). All XPS data were recorded with Si Kα ($h\nu = 1739.5$ eV) to prevent overlap of the characteristic N1s peak with the Ni LMM Auger electrons. The full XPS spectrum is shown in figure 4.2.

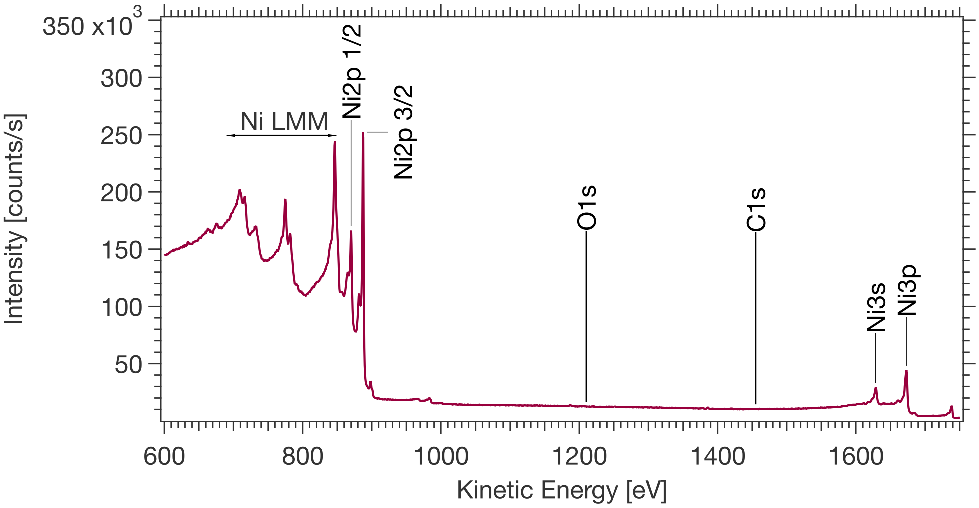

Figure 4.2 XPS overview from the bare Ni(111) substrate after cleaning, measured with Si Kα ($h\nu = 1739.5$ eV). No characteristic core-level peaks of contaminants (O and C) are visible.

After the preparation, another set of XPS spectra is taken to check the stoichiometry. The corresponding B1s and N1s spectra are shown in figure 4.3. These peak areas then are normalized by the cross-sections $\sigma_B = 0.0055$ and $\sigma_N = 0.02$ for the photon energy of $h\nu = 1739.5$ eV [74]. Boron (B) and nitrogen (N) are present in a stoichiometric ratio of 1 : 0.98 which is very close to the ideal ratio of 1 : 1.

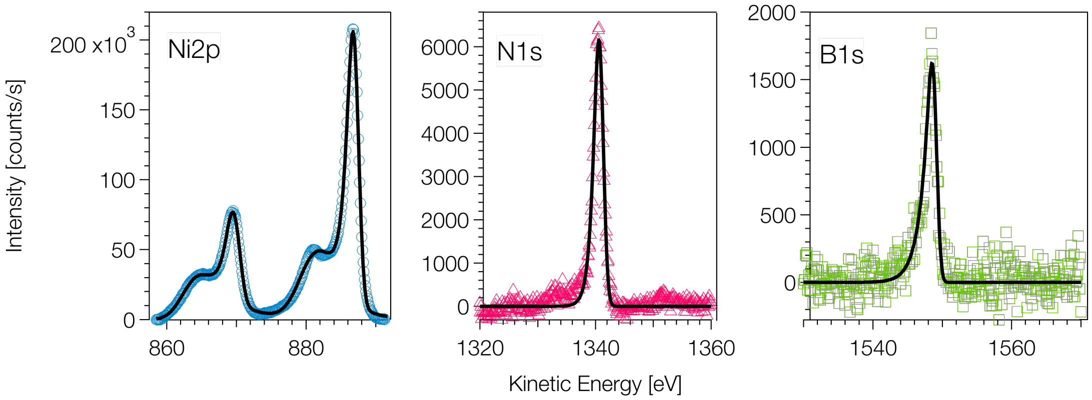

Figure 4.3 XPS data of N1s (pink, open triangles), B1s (green, open squares) and Ni2p (blue, open circles) after the deposition of a monolayer of boron nitride. The spectra are background corrected by a Shirley background. Data recorded with Si Kα ($h\nu$ = 1739.5 eV)

4.2.3 Structural information

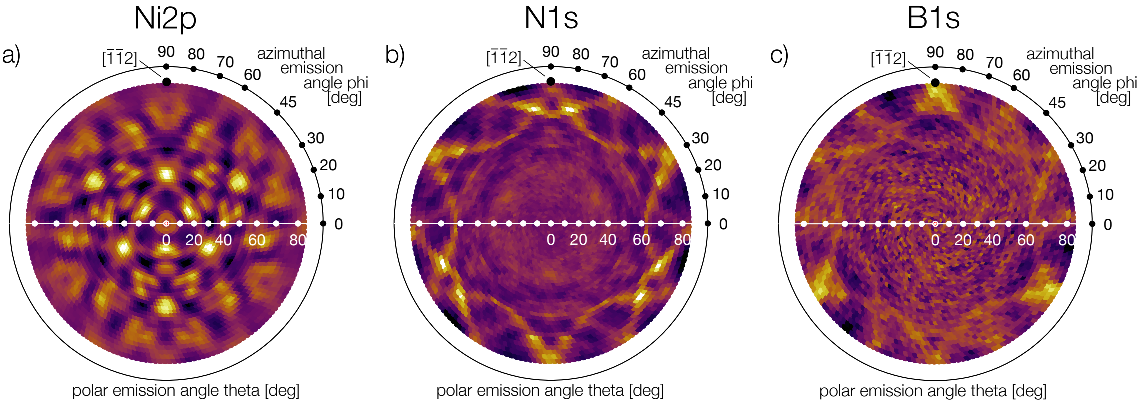

Figure 4.4 XPD patterns of h-BN on Ni(111) recorded with Si Kα x-ray source ($h\nu$ = 1739.5 eV). **a)** Ni2p 3/2 emitter (E_{kin} = 887 eV) **b)** N1s (E_{kin} = 1550 eV) **c)** B1s (E_{kin} = 1342 eV)

An XPD pattern recorded at the kinetic energy of the Ni2p 3/2 emitter is shown in figure 4.4a). The diffraction pattern shows the three-fold symmetry which is expected from the (111) crystal orientation from the face centered cubic (fcc) metal. With this information, the high symmetry directions of the sample can be found. The XPD pattern of N1s and B1s are displayed in figure 4.4b and 4.4c. The difference between these patterns indicates that the monolayer is slightly corrugated [73]. If that were not the case, we would expect a similar N1s pattern as B1s, with three forward focussing spots at ≈ 85 ° polar angle. The forward scattering intensity is concentrated on the B1s pattern which indicates that the nitrogen atoms sit slightly higher than the boron atoms. The ring-like structures in the N1s pattern indicate first order interference cones which are mapped as rings from the stereographic projection. The stacking of the h-BN layer is (N,B)=(top,fcc) which is defined by the forward scattering maximum for B1s at the high symmetry direction $[\overline{1}\overline{1}2]$ [75]. Detailed information on the XPD patterns from h-BN/Ni(111) can be found in Refs [67, 73, 75].

4.2.4 Work function and valence bands

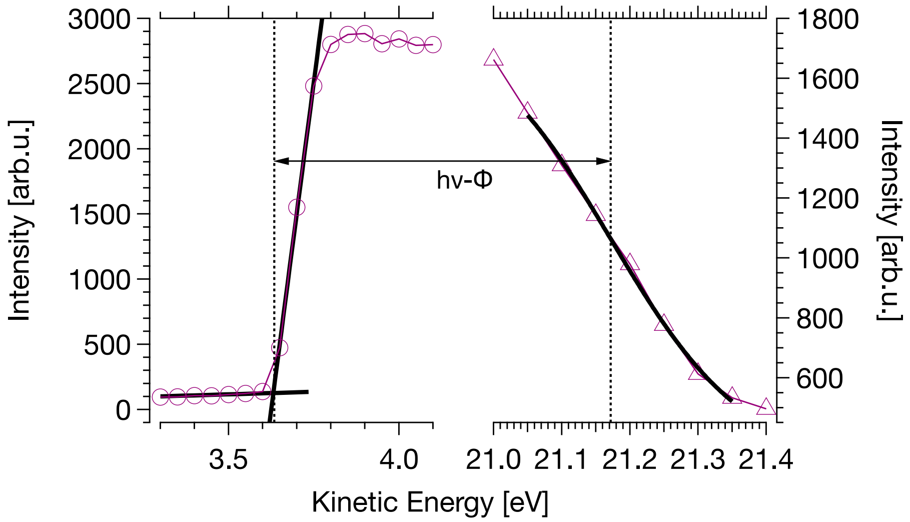

Figure 4.5 Fermi edge and secondary cut-off measurement for a monolayer of h-BN on nickel taken with He Iα ($h\nu = 21.2\,\mathrm{eV}$) photons. The work function of Ni(111) is reduced from 5.3 eV to 3.68 eV after the deposition of boron nitride.

The sample work function is a first indication of the quality of the h-BN film prepared on Ni(111). The work function of $\phi = 5.3\,\mathrm{eV}$ of bare Ni(111) is reduced to 3.68 eV [24] when covered with a monolayer of h-BN. It can be measured with the helium discharge lamp by applying a voltage to the sample and measuring the Fermi edge and the secondary cut-off as shown in figure 4.5. Here we take the intersection of the edge and baseline on the left side to determine the secondary cut-off. E_F was found by fitting a Fermi-Dirac distribution to the spectrum on the right. From equation 2.1 the work function $\phi = 3.68\,\mathrm{eV}$ can be calculated.

A second indication can be found in the valence band structure. h-BN/Ni(111) shows a characteristic valence band structure dominated by the strongly dispersing σ- and π-bands of the boron nitride layer. The cross-section from He Iα ($h\nu = 21.2\,\mathrm{eV}$) to He IIα ($h\nu = 40.8\,\mathrm{eV}$) favour the σ-band for He Iα or the π-band for He IIα. In figure 4.6 the valence band spectra for three different high symmetry points of the first Brillouin zone and the two different photon energies are shown. For He Iα the σ-band has a strong contrast whereas the π-band appears stronger with He IIα. The

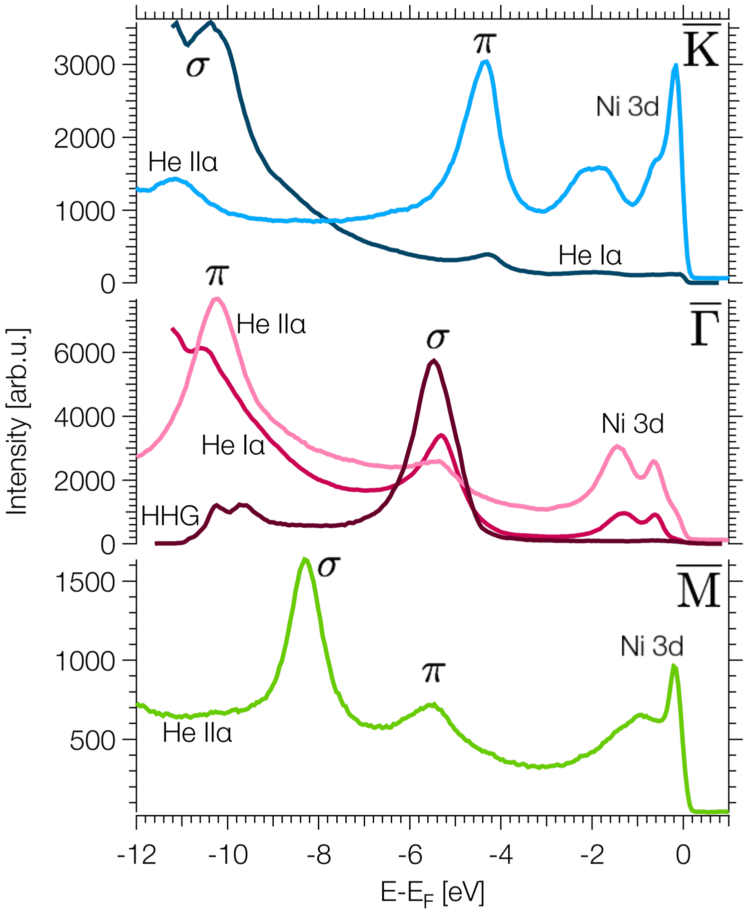

Figure 4.6 Valence band measurements with He Iα, He IIα and HHG for the high symmetry points of the SBZ. The valence band spectra reveal that the intensity of the σ- and the π-bands strongly depends on the photon energy used.

initial state energies are tabulated in table 4.1. The σ-band is located at -5.4 eV and the π-band at -10.2 eV at normal emission [65]. Moving further out in k-space to the $\overline{\mathrm{K}}$-point, the π-band moves up to -4.3 eV and the σ-band down to -11.6 eV and -12.4 eV. The two different binding energies for the σ-band at the $\overline{\mathrm{K}}$-point refer to the splitting of the band. At the $\overline{\mathrm{M}}$-point the σ-band is found at -8.2 eV and the π-band is at -5.5 eV. The full ARPES data are shown in figures 4.7 and 4.8. The most interesting point is the π-band at $\overline{\mathrm{K}}$ which is the valence band maximum of h-BN. From the initial state energy of -4.3 eV of the π-band and the calculated energy of 2 eV for the π^*-band [16] the $\pi - \pi^*$ energy gap at $\overline{\mathrm{K}}$ is expected to be 6.3 eV.

$E - E_{\mathrm{F}}$	$\overline{\Gamma}$	$\overline{\mathrm{K}}$	$\overline{\mathrm{M}}$
σ-band	$-5.4\,\mathrm{eV}$	$-11.6\,\mathrm{eV}$ / $-12.4\,\mathrm{eV}$	$-8.2\,\mathrm{eV}$
π-band	$-10.2\,\mathrm{eV}$	$-4.3\,\mathrm{eV}$	$-5.5\,\mathrm{eV}$

Table 4.1 Binding energies of σ- and π-bands of h-BN for the high symmetry points in the SBZ.

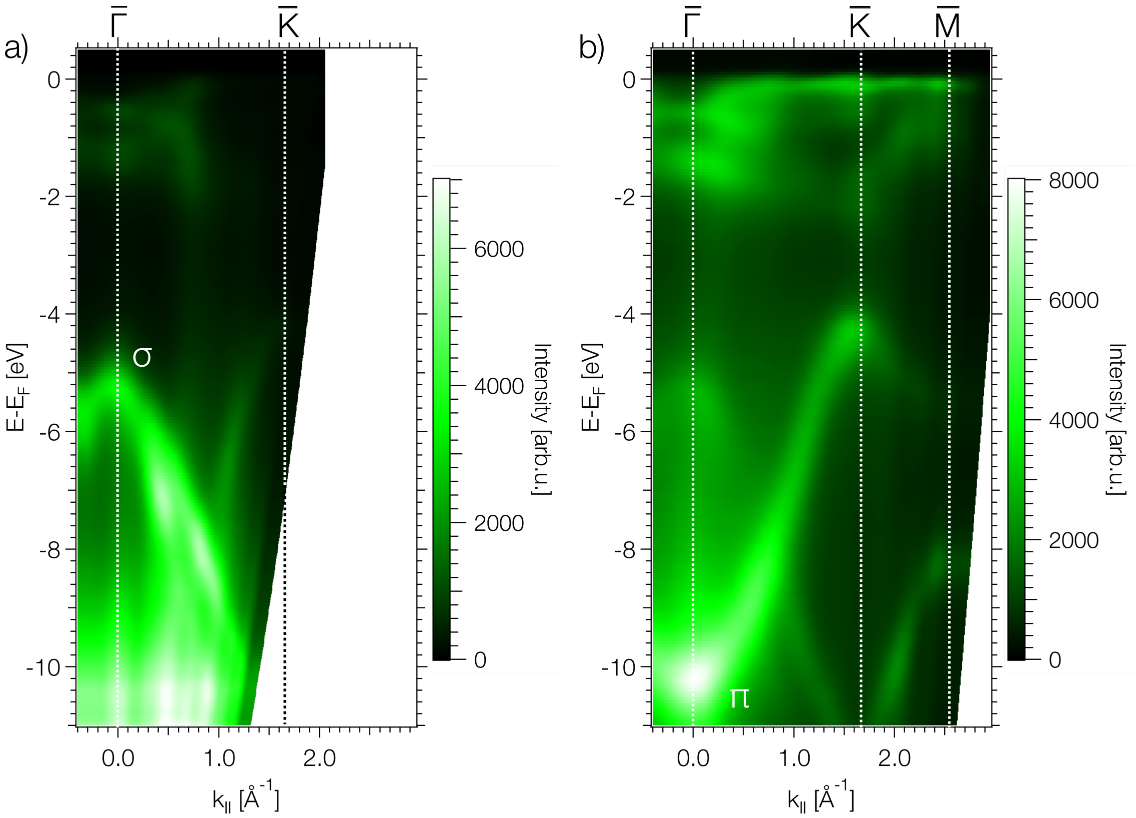

Figure 4.7 ARPES of h-BN/Ni(111) recorded with the low-pressure high-intensity helium discharge lamp. σ- and π-bands are indicated. **a)** He Iα data along $\overline{\Gamma} - \overline{\mathrm{K}}$. **b)** He II$\alpha$ data along $\overline{\Gamma} - \overline{\mathrm{K}} - \overline{\mathrm{M}}$.

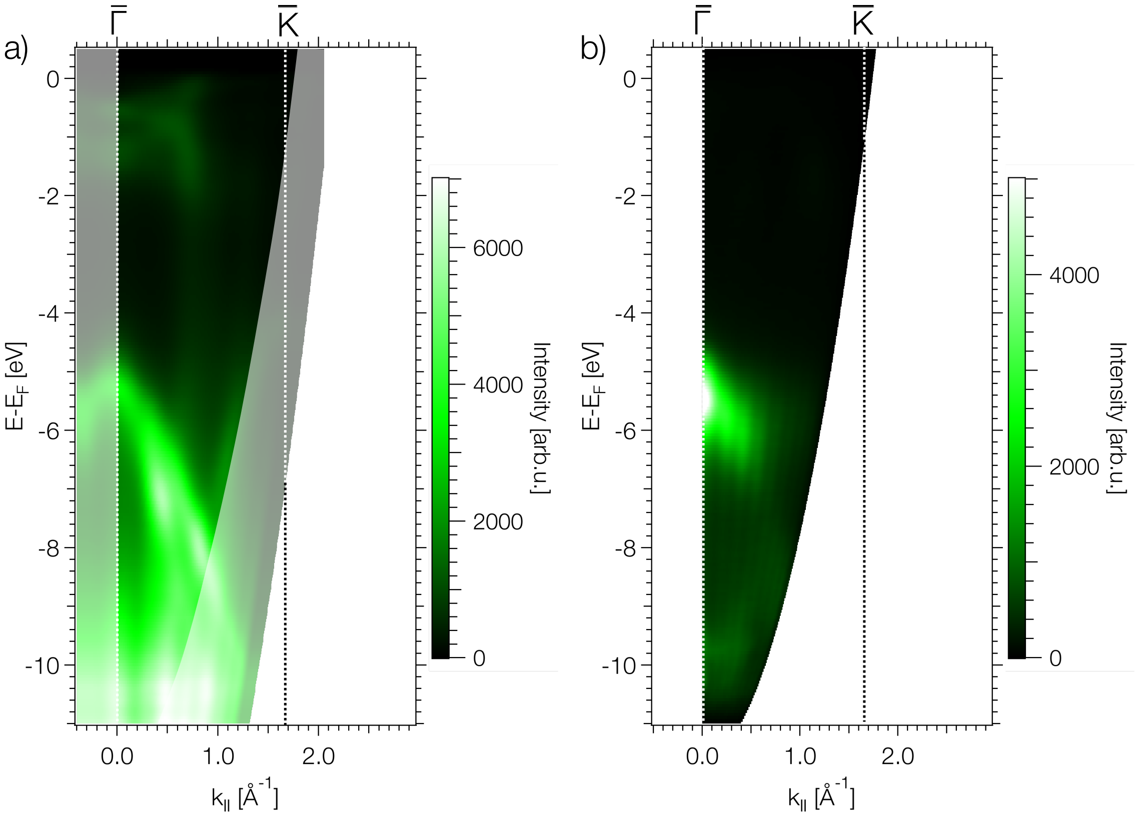

Figure 4.8 ARPES of h-BN/Ni(111) measured with $h\nu = 21.2\,\mathrm{eV}$ from He Iα and $h\nu = 15\,\mathrm{eV}$ from the HHG. **a)** He Iα data along $\overline{\Gamma} - \overline{\mathrm{K}}$. The area enclosed by the white shaded part indicates the range which is measured with the HHG light source. **b)** HHG data along $\overline{\Gamma} - \overline{\mathrm{K}}$.

4.3 Time-resolved measurements

In this section we present tr2PPE and trARPES measurements from a monolayer of h-BN on Ni(111). The schematic of the laser setup used within this section is displayed in figure 3.5. Different combinations of the fundamental 800 nm beam, SHG and fourth harmonic generation (FHG) were used to record the data.

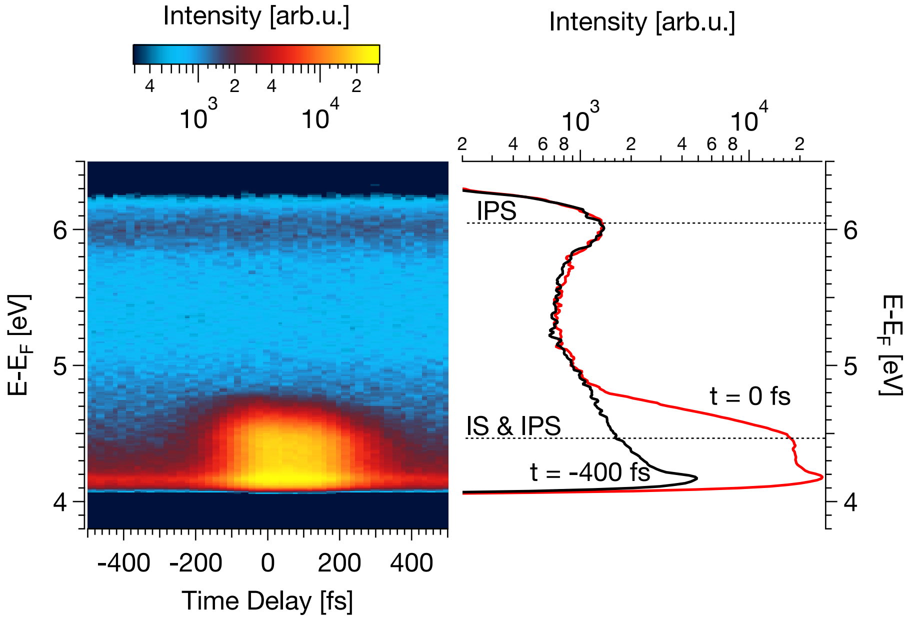

Figure 4.9 tr2PPE data recorded with $\lambda_{pump} = 808\,\text{nm}$ (s-pol) and $\lambda_{probe} = 404\,\text{nm}$ (p-pol). *Left panel:* EDCs displayed versus time delay between pump and probe pulse. The EDCs were integrated over the full angular axis of the photoelectron detector window. *Right panel:* Two EDCs at $t = 0$ and $t = -400\,\text{fs}$ at normal emission are plotted.

In figure 4.9 the tr2PPE data from the h-BN/Ni(111) are displayed which were measured with s-polarized 1.535 eV pump and p-polarized 3.07 eV probe with a bias voltage of $-5\,\text{V}$ applied to the sample. In the left panel, the EDCs are displayed versus the time delay between pump and probe. The EDCs were integrated over the full angular detector window. In the right panel, two EDCs integrated over 5 ° at normal emission are shown. The curve at $t = 0$ shows two unoccupied states (dotted lines) which correspond to the image potential state (IPS) and the interface state (IS) [16, 24]. The IPS has a final state energy of 6.05 eV and the resonance (IS & IPS) 4.47 eV. It has to be mentioned at this point that the work function for this preparation was determined to be 3.68 eV as shown in figure 4.5. The origin of the sudden cut-off seen at 4 eV in the EDCs still remains unclear.

The transient intensity of the resonance is shown in figure 4.10. The data were fitted with a Gaussian convoluted with an exponential. The FWHM of the Gaussian is

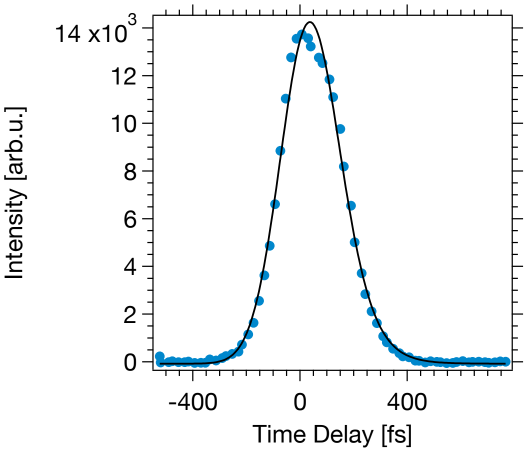

Figure 4.10 The transient intensity for the resonance is plotted with intensity (arb.u.) versus time delay.

332 fs and the time constant is 65 fs. It was shown in Ref [24] that the resonance is most pronounced at $\lambda_{\text{pump}} = 810\,\text{nm}$ and that the transient intensity is a Gaussian when IS and IPS are in resonance.

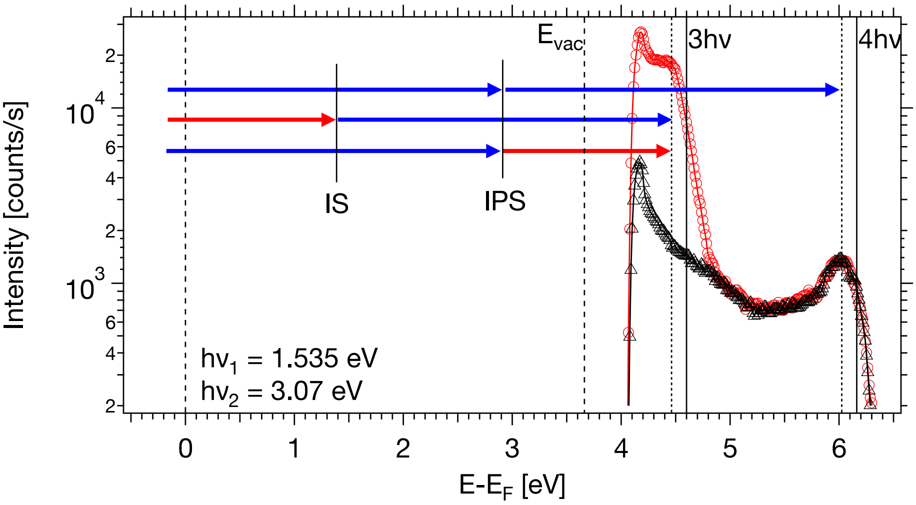

Figure 4.11 Schematics of the excitation paths. The EDCs are taken from figure 4.9. The red (circles) curve corresponds to $t = 0$ and the black (triangles) curve to $t = -400\,\text{fs}$. The IPS at 6.05 eV has to be pumped and probed by blue photons since there is no dynamics. The resonance at 4.47 eV does show dynamics.

The level diagram in figure 4.11 explains the excitation paths of the unoccupied states and the corresponding final state energies. The resonance at 4.47 eV shows clear dynamics on top of a constant background of the two-photon photoemission (2PPE) signal from 404 nm light (black curve). The resonance consists of the IS and IPS which have the same final state energy for the photon energies used [24]. The IS is pumped by a red photon and probed by a blue photon whereas the IPS is pumped by blue and probed by red. The image potential state at 6.05 eV does not show any dynamics what means that it has to be pumped and probed by blue photons. Therefore, the initial state energy of the IS is 1.4 eV and for the IPS 2.98 eV. Considering the work function of 3.68 eV, the IPS is 700 meV below the vacuum energy. The energies for the unoccupied states nicely fits the findings in Ref [24].

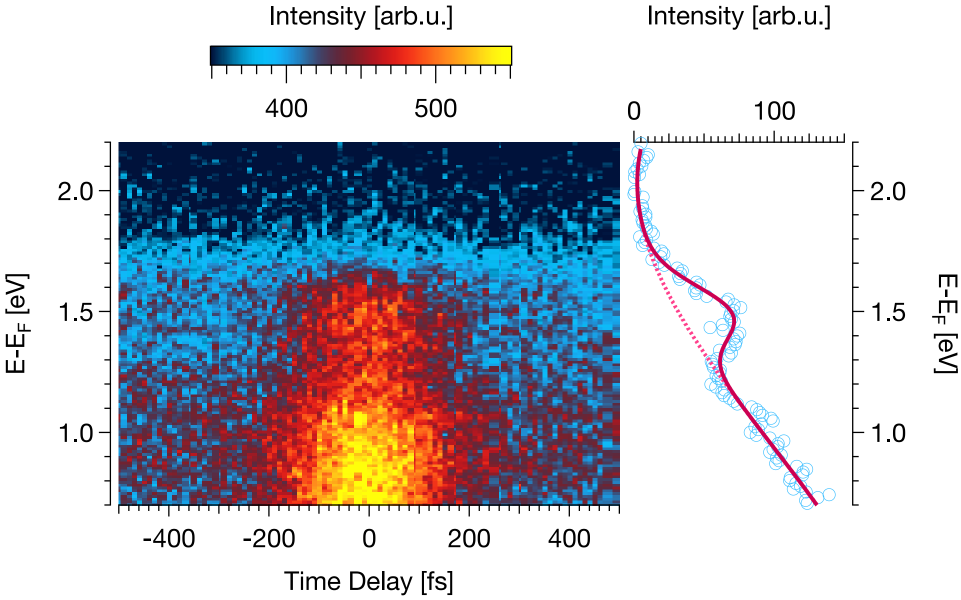

Figure 4.12 Time-resolved measurement with $h\nu = 800\,\mathrm{nm}$ pump and $4h\nu = 200\,\mathrm{nm}$ probe. *Left panel:* The EDCs integrated over ±5° around normal emission and the final state energy is plotted versus time delay. *Right panel:* The data points (blue, open circles) show the difference spectra of t_0 and before t_0. The EDCs used are indicated by the two lines in the carpet to the left. The IS is found at $E - E_\mathrm{F} = 1.496\,\mathrm{eV}$ and with a FWHM of 260 meV.

The next step is to populate the unoccupied states with the fundamental ($\lambda_{pump} = 830\,\mathrm{nm}/1.5\,\mathrm{eV}$) and to probe with the FHG ($\lambda_{probe} = 207\,\mathrm{nm}/6\,\mathrm{eV}$). By employing this combination it should be possible to populate the IS with 830 nm and probe with 207 nm. Calculations predicted the IS at 1.63 eV and 1.75 eV depending on the spin of the electron [16]. The IS was measured experimentally by means of inverse photoemission spectroscopy where an initial state energy of 1.75 eV and 1.85 eV was determined [72]. At the same time, in tr2PPE experiments the IS was found at 1.51 eV above E_F [24]. The different energies found for the IS is conjectured to be an excitonic energy reduction. From the tr2PPE measurements we can determine the binding energy of the unoccupied IS which should be roughly 1.5 eV above the Fermi level because it has been shown that the resonance is 100 meV below the IS [24].

The trARPES data from 1.5 eV pump and 6 eV probe is shown in figure 4.12. In the left panel, the EDCs integrated over the full angular window of the detector are plotted versus time delay. The difference of the EDCs at $t = 0$ and $t = -400$ fs at normal emission is illustrated in the right panel. It shows the populated IS at $E = 1.496$ eV above E_F with a FWHM of 370 meV on top of a background of hot electrons indicated by the dotted line.

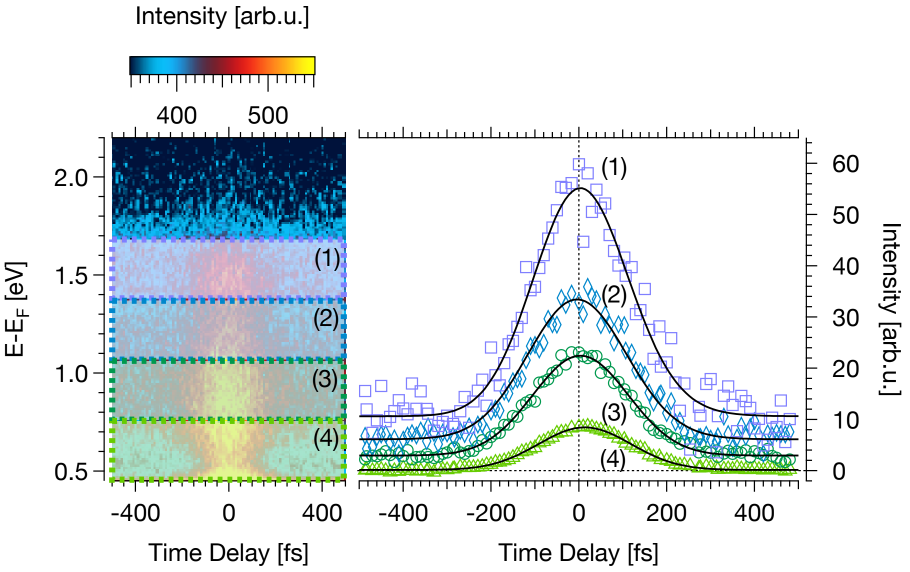

Figure 4.13 Transient intensities at different energy positions. *Left panel:* Carpet from figure 4.12 with larger energy range. The boxes (1)-(4) indicate the integration region for the transient intensities to the right side. *Right panel:* Time traces fitted with Gaussians convoluted with an exponentials. The purple trace (open squares) belongs to the IS at 1.496 eV.

In figure 4.13, transient intensities integrated over certain energy ranges at normal emission are shown. In the panel to the left, the same data as in figure 4.12 with bigger energy window is plotted. The boxes indicate the integration areas for the transient intensities at normal emission which are illustrated in the right panel. The fits (black solid lines) reveal that curve (1) and (2) are Gaussians but (3) and (4) show time constants of $\tau = 29$ fs and $\tau = 43$ fs, respectively.

The lifetime of the IS was experimentally verified to be 107 fs [24, 25]. From our data set, we are not able to extract the same lifetime. The time constant for the box (1), which corresponds to the IS, is 43 fs. However, the FWHM for (1)-(3) is 362 fs and gets reduced at (4) to 336 fs. Moreover, the maximum of the fit for (1) and (2) is at 5 fs, for (3) at -31 fs and for (4) at -34 fs.

In an attempt to observe the unoccupied π^*-band at $\overline{\mathrm{K}}$ and to determine the nature of the band gap we participated in a synchrotron beamtime together with Prof. Annick Loiseau and carried out trARPES in our homelab. This particular experiment was carried out with the HHG source in our lab and from h-BN single crystals at the

TEMPO beamline at the synchrotron Soleil in France. In our lab the h-BN/Ni(111) sample was pumped with 1.55 eV to excite the Ni3d electrons into the π^*-band of the boron nitride at $\overline{\mathrm{K}}$ and probe the excited electrons with 15 eV. The calculated initial state energy of 2 eV [16] and the experimentally measured initial state energy of 2.2 eV [72] the π^*-band at $\overline{\mathrm{K}}$ suggest that the pump photon energy needs to be increased. In future experiments, it is planned to extend the HHG setup in order to have the availability of a tunable pump laser source by adding the optical parametric amplifier (OPA). Then one would have the option to tune the pump photon energies from 1.77 eV to 2.58 eV.

The experiment performed at TEMPO was done in collaboration with the group of Prof. Dr. Annick Loiseau. The goal was to pump a π–π^* transition at the $\overline{\mathrm{K}}$-point of the h-BN single crystals [76] with 6.3 eV light and to probe with 120 eV synchrotron radiation. The predicted energy gap in bulk h-BN for the $\pi - \pi^*$ transition is 4.5 eV from LDA and 6.19 eV from GW calculations [71]. However, the experiment of pumping the $\pi - \pi^*$ transition with 6.3 eV light did not reveal the unoccupied π^* band. Since DFT calculations are known to underestimate band gaps, the missing dynamics could be attributed to low pump photon energies.

4.4 Conclusions

We did successfully demonstrate that a monolayer of h-BN on Ni(111) can be prepared and characterized with the new photoemission setup TREx. The resonance of the IS and IPS was populated with 1.535 eV and probed with 3.07 eV in the tr2PPE experiment and observed at 1.4 eV above the Fermi level. The time constant of the resonance is 65 fs. In Ref [24] it was shown that in order to observe the time constants of the IS and IPS the wavelength have to be changed to 1.47 eV and 1.57 eV, respectively. Moreover, the IS was populated with 1.5 eV and probed with 6 eV in trARPES. The IS was found at the initial state energy of 1.496 eV with a time constant of 43 fs. The IS was predicted to be at 1.63 eV and 1.75 eV [16], respectively, depending on the spin of the electron. With inverse photoemission spectroscopy, the IS was observed at 1.75 eV and 1.85 eV [72]. The different energy compared with the value found is conjectured to be an excitonic energy reduction. In Ref [24], the IS was observed by means of tr2PPE at 1.51 eV which fits our result. The π^* population at $\overline{\mathrm{K}}$ with 1.55 eV pump and 15 eV probe could not be observed. The calculated initial state energy of 2.2 eV [72] suggests that the pump photon energy needs to be increased. The tunability and extension of the pump photon energies is planned to be done (see chapter 7).

5 Bi_2Se_3

5.1 Introduction

Atoms and their electrons can establish different forms of condensed matter. Such states of condensed matter like crystals, magnets or superconductors can be attributed to symmetries which spontaneously break [77]. The quantum Hall (QH) state which was discovered in 1980 [78] describes a quantum state in a semiconductor which has no spontaneously broken symmetry but can be broken by an external magnetic field. The quantum state only depends on the topology of the solid. The QH effect requires cooling of the solid and a strong external magnetic field applied to the two-dimensional electron gas to force the electrons only to travel along the edges of the semiconductor where the two counterflows of electrons are spatially separated. The quantum spin Hall (QSH) state [79] is a newer class of topological states which topologically differs from the QH state. QSH systems are insulating in the bulk where the valence bands and conduction band are separated by an energy gap, but on the boundary, they get metallic by forming a gapless edge or surface state. The missing energy gap at the edges is topologically protected and is immune to defects and perturbations. These topological insulators (TI) share similarities with QH systems but differ in a specific point where the QH systems need an external magnetic field to break the time-reversal (TR) symmetry, the TIs are TR invariant and do not need an external magnetic field.

5.2 Topological insulators

The counter-propagation of electrons with opposite spin in QSH systems requires spin-orbit coupling (SOC) which is strong in systems containing heavy elements. The SOC in heavy elements is no guarantee that they are candidates for TIs. In fact, only few of them turn out to be TIs. The mechanism which stays behind finding a TI candidate is the band inversion, proposed by Bernevig et al. [79] in 2006. In heavy elements, the SOC is so large that the p-type valence band orbital can be lifted above the s-type conduction band orbital leading to band inversion. Band inversion is illustrated in a tight-binding model calculation from [80] on Bi_2Se_3 in figure 5.1. One can observe by increasing the SOC (M=mass term) by moving from right to left in the figure that a trivial Rashba pair is transformed into the topological surface state (TSS) and unoccupied surface resonance (USR) by band inversion.

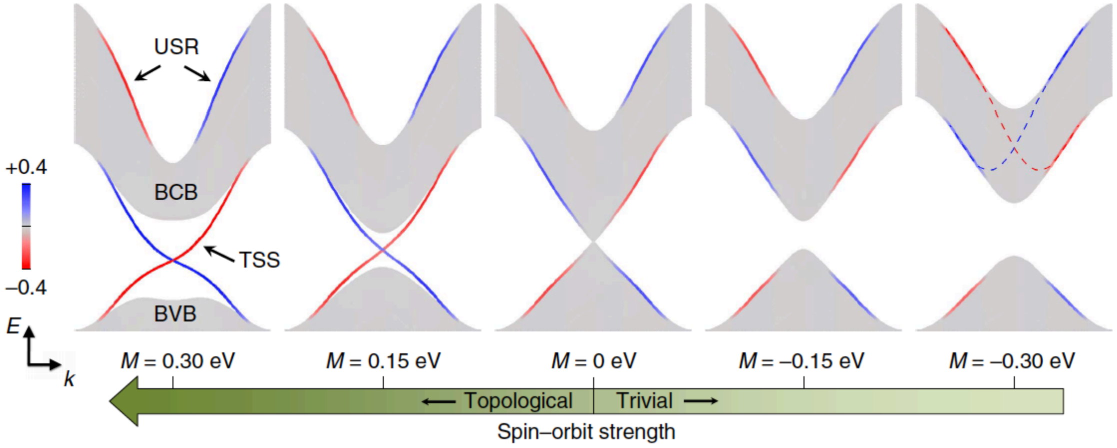

Figure 5.1 Tight binding model calculation results of Bi_2Se_3 from [80]. The band structure on the left ($M = 0.3\,\mathrm{eV}$) qualitatively represents the experimental observations of the surface state and the conduction band. By moving to the left side, the mass term M is increasing to simulate an increase of SOC. A trivial Rashba pair gets transformed into the topological surface state and unoccupied surface resonance by band inversion. Figure taken from Ref [80].

The two-dimensional topological insulator mercury telluride (HgTe) quantum well was introduced by Bernevig et al. [79]. The HgTe quantum well was placed in between cadmium telluride CdTe layers which has a similar lattice constant and weaker SOC than HgTe. It could be shown that a minimum thickness of the HgTe layer exists where the SOC becomes dominant, and the bands are inverted. The band inversion in HgTe is illustrated in figure 5.2. A pair of one-dimensional edge states are found at the momentum $k = 0$, where the dispersion of these states is linear at the crossing point. The dispersion corresponds to a massless relativistic fermion in one dimension. This picture can be extended to three dimensions where the dispersion forms a Dirac cone which consists of a massless two dimensional Dirac fermion.

Hsieh et al. [81] experimentally discovered in 2008 the first three-dimensional TI in $Bi_{1-x}Sb_x$. In 2009, Bi_2Se_3 one of the second generation TIs was reported by Xia et

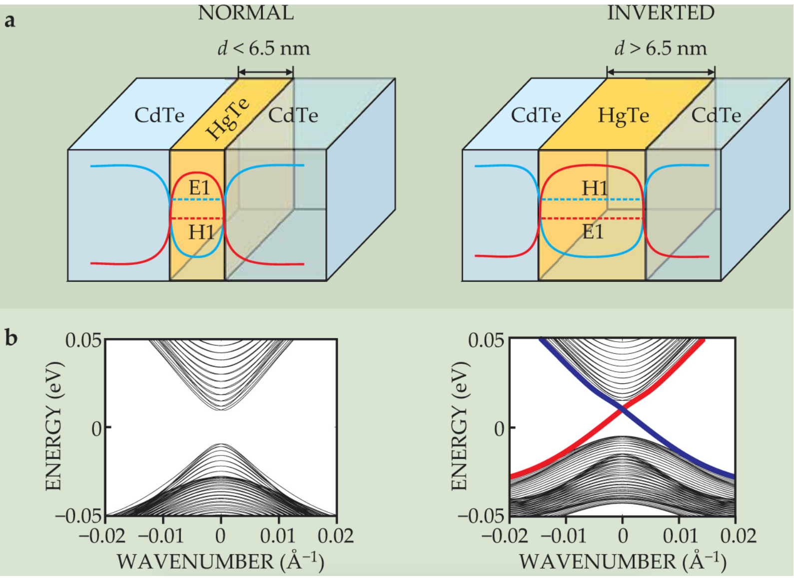

Figure 5.2 Illustriation of the two-dimensional TI HgTe. **a)** If the minimum thickness ($d>$ 6.5 nm) of the HgTe in between CdTe is exceeded the strong SOC in HgTe becomes dominant and the bands H1 and E1 are inverted. **b)** The system then becomes a topological insulator with a surface state with linear disperstion at the crossing point ($k=0$). This figure is taken from [77].

al. [82]. This material also shows the band inversion at $k=0$ forming a single three-dimensional Dirac cone on the surface. Thus, Bi_2Se_3 is metallic on the surface and insulating in the bulk. One of the most important aspects in view of applications is the relatively large band gap of 300 meV which indicates TI behavior even at room temperature [83].

5.3 Crystal and band structure of Bi_2Se_3

Figure 5.3a illustrates the rhombohedral unit cell crystal structure with the three primitive lattice vectors t_1,t_2 and t_3 of Bi_2Se_3. The unit cell, with the lattice constants $a = 4.143$ Å and $c = 28.636$ Å consists of three stacked quintuple layers which are bound by van der Waals forces [84]. The samples are prepared in UHV by scotch tape cleaving where the termination is expected between the Se1 planes due to the weak van der Waals bonding between the quintuple layers [85].

The first Brillouin zone is displayed in figure 5.3b. The four inequivalent time-reversal-invariant momenta (TRIM) Γ, Z, F and L of the three-dimensional first Brillouin zone are projected onto the two-dimensional first Brillouin zone of the (111) surface resulting in the high-symmetry points $\overline{\Gamma}$, $\overline{\mathrm{M}}$ and $\overline{\mathrm{M}'}$. Particularly for ARPES, the high-symmetry points $\overline{\Gamma}$, $\overline{\mathrm{M}}$ and $\overline{\mathrm{M}'}$ are of great interest.

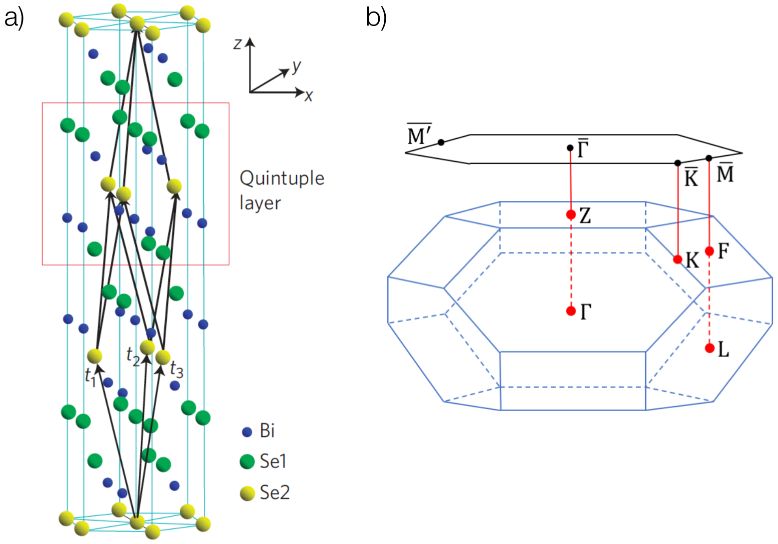

Figure 5.3 Real and reciprocal space illustration of Bi_2Se_3. **a)** The rhombohedral unit cell consists of three quintuple layers bonded by van der Waals forces and is defined by the three primitive lattice vectors t_1, t_2 and t_3. **b)** The three dimensional Brillouin zone with the high-symmetry points Γ, Z, F, L and K projected onto the two-dimensional surface Brillouin zone of the (111) surface with $\overline{\Gamma}$, $\overline{\mathrm{M}}$ and $\overline{\mathrm{K}}$. This figure is adapted from [86].

The distance of $\overline{\Gamma\mathrm{M}}$ is calculated by considering the primitive lattice vectors and the lattice constants [87]:

$$t_1 = (-a/2,\ -\sqrt{3}a/6,\ c/3) \tag{5.1}$$

$$t_2 = (a/2,\ -\sqrt{3}a/6,\ c/3) \tag{5.2}$$

$$t_3 = (0,\ \sqrt{3}a/3,\ c/3) \tag{5.3}$$

In figure 5.4, Bi_2Se_3 band structure calculations of the (111) surface are shown [82]. Bi_2Se_3 only exhibits a bulk parity inversion at the TRIM Γ [86]. Due to the strong SOC and the parity inversion, the bands at $\overline{\Gamma}$ of the (111) surface show non-trivial behavior [88]. Thus, the bands at $\overline{\Gamma}$ are inverted and a Dirac cone is formed on the surface.

Bi_2Se_3 is grown as n- or p-doped single crystalline sample. The crystals of Bi_2Se_3 are intrinsically n-doped due to the vacancies of Se atoms [89]. The p-type doping can be accomplished by substituting roughly 1 % of the Bi atoms with Ca [90]. In n-type Bi_2Se_3 a downward band bending from bulk to surface due to aging in UHV was observed [91–93]. This band bending was found to extend 20 nm inside the bulk

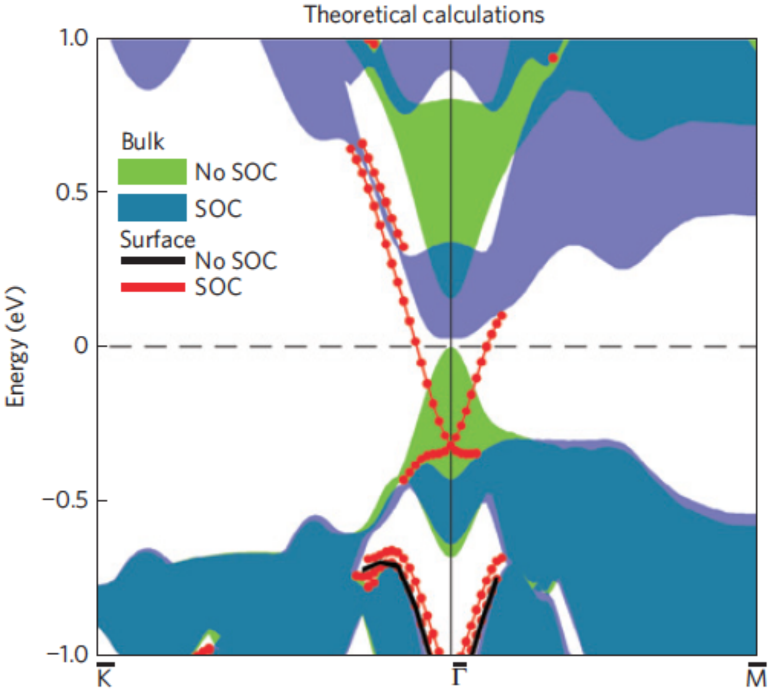

Figure 5.4 LDA band structure calculations of the (111) surface of Bi_2Se_3. Bulk parity inversion at Γ and the strong SOC from a Dirac cone at $\overline{\Gamma}$. This figure is taken from Ref [82].

and the energy of the Dirac point changes by roughly 100 meV to higher binding energies.

The samples used within the framework of this thesis are grown by the group of P. Hofmann from the University of Aarhus. In figure 5.5 we present ARPES data measured by C. Monney with the setup of P. Aebi at the University of Fribourg. The measurements were done with 6.2 eV while the Bi_2Se_3 crystal was held at 70 K. The partially filled TSS and BCB, displayed in figure 5.5a, indicate the n-type nature of the sample. The energy gap between the BCB bottom and the Dirac point can be estimated to be 200 meV. Figure 5.5b depicts an EDC at normal emission ($k_{\|} = 0$). The work function ($\phi = h\nu - \Delta E$) could be determined to be 5.58 eV and the position of the Dirac point is 280 meV below the Fermi level.

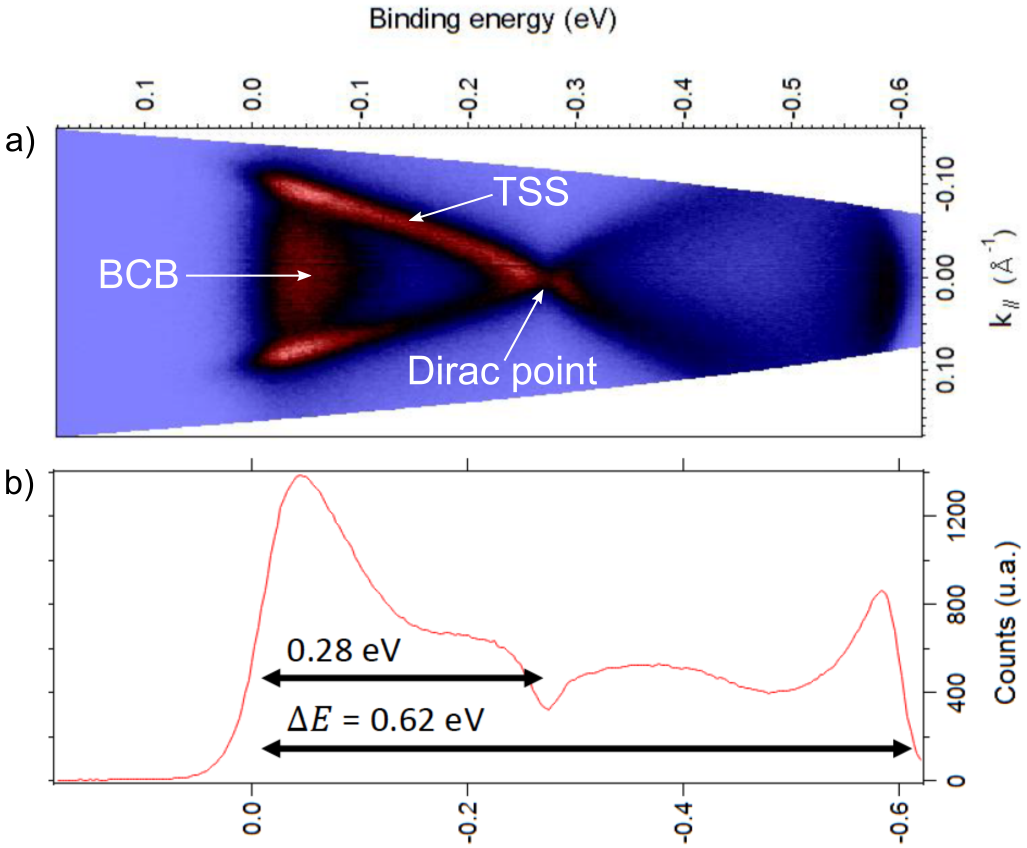

Figure 5.5 ARPES measurement with 6.2 eV while the sample was held at 70 K. **a)** ARPES data illustrated with the most prominent band structure features around $\overline{\Gamma}$. The energy gap between the Dirac point and the bulk conduction band (BCB) bottom is roughly 200 meV. **b)** EDC from a) at $k_{\|} = 0$. The Dirac point is found to be at 280 meV below the Fermi level and the work function is 5.58 eV. These data were taken by the group C. Monney with the setup of P. Aebi at the University of Fribourg.

5.4 Previous time-resolved studies

This section covers a short summary of previous results which are relevant for the discussion of the findings within the time-resolved section of the thesis. Carrier dynamics of the surface state and bulk conduction band on a femtosecond timescale play a major role for the understanding of our observations at the $\overline{\Gamma}$ and $\overline{\mathrm{M}}$ point.

Electron dynamics of the TSS and BCB in p-type Bi_2Se_3 was previously studied by Sobota et al. [62]. They could show using 6 eV probe that upon excitation with 1.5 eV pump the completely unoccupied TSS and BCB are populated. The electrons are excited to ~ 1.3 eV above the Fermi level and relax quickly, triggering a cascade of scattering processes and populating the TSS and BCB. The population decay time constants of the TSS above the BCB bottom are in the order of 2 ps. Remarkably, the BCB bottom is still populated at 10 ps as well as the TSS below the BCB bottom. The interpretation is that the BCB bottom acts as a charge reservoir which slowly relaxes by interband scattering into the TSS on a time scale of $\sim 6\,\mathrm{ps}$.

A similar study was carried out on $\mathrm{Bi_2Te_3}$ by Hajlaoui et al. [94]. Their trARPES experiment was performed with similar photon energies (1.58 eV pump and 6.32 eV probe). Unlike in Ref [62], these samples were n-doped. In n-type $\mathrm{Bi_2Te_3}$, the TSS and BCB are partially filled. Thus the dynamics of the interband scattering from the BCB bottom to the TSS below E_F is based on electron-hole recombination. They showed that the TSS below the BCB bottom is refilled on the similar timescale of $\sim 6\,\mathrm{ps}$ as in Ref [62]. This suggest that the slow refilling of the TSS by interband scattering could be a general property within the class of TIs.

5.5 TrARPES measurements

In this section, trARPES results at the high symmetry points $\overline{\Gamma}$, $\overline{\mathrm{M}}$ and $\overline{\mathrm{M}'}$ are presented. The data in the following subsections is splitted into two parts. The first subsection covers the electron and hole dynamics of the TSS and BCB at $\overline{\Gamma}$. The second part concentrates on the excitation of the BCB and the dynamics in the occupied band structure at $\overline{\mathrm{M}}$ and $\overline{\mathrm{M}'}$.

All time-resolved data were measured with p-polarized 1.5 eV pump and the p-polarized 5th harmonic of the SH driving laser as probe ($h\nu = 15\,\mathrm{eV}$) at a pressure of $1.6 \cdot 10^{-9}$mbar in the AC during the measurements. Data sets with varying polarizations (s-polarized pump and/or s-pol probe) were taken as well but no change of the results was observed. The sample was pumped with a photon fluence of $\sim 226\,\mu\mathrm{J\,cm^{-2}}$ and held at room temperature. The time and energy resolution for this experiment could be determined to be 103 fs and 190 meV, respectively.

The band bending effect due to aging is assumed to be saturated (see section 5.3). All measurements were performed over the course of eight days without observing a shift of the TSS. The measurement geometry is illustrated in figure 5.6. The angle of light incidence at normal emission is 45 °. In order to reach the $\overline{\mathrm{M}}$-point, the sample was rotated towards the light source by 34 °. Thus, the angle of incidence is reduced to 11 °. The sample needs to be rotated azimuthally 180 °, but the angle of incidence remains unchanged to reach $\overline{\mathrm{M}'}$.

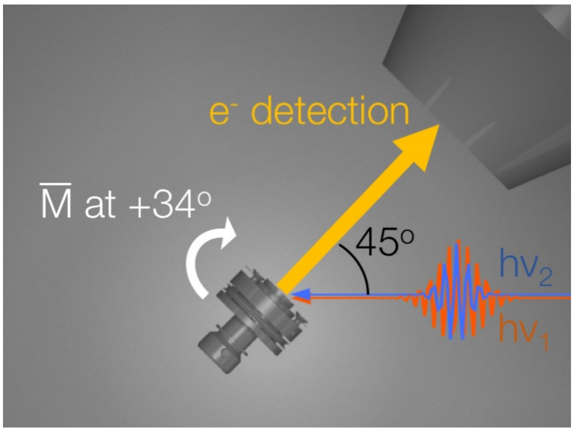

Figure 5.6 Illustration of the measurement geometry. The angle of incidence at normal emission is 45 °. $\overline{\mathrm{M}}$ is reached by a rotation of 34 °.

5.5.1 Electron and hole dynamics of TSS and BCB

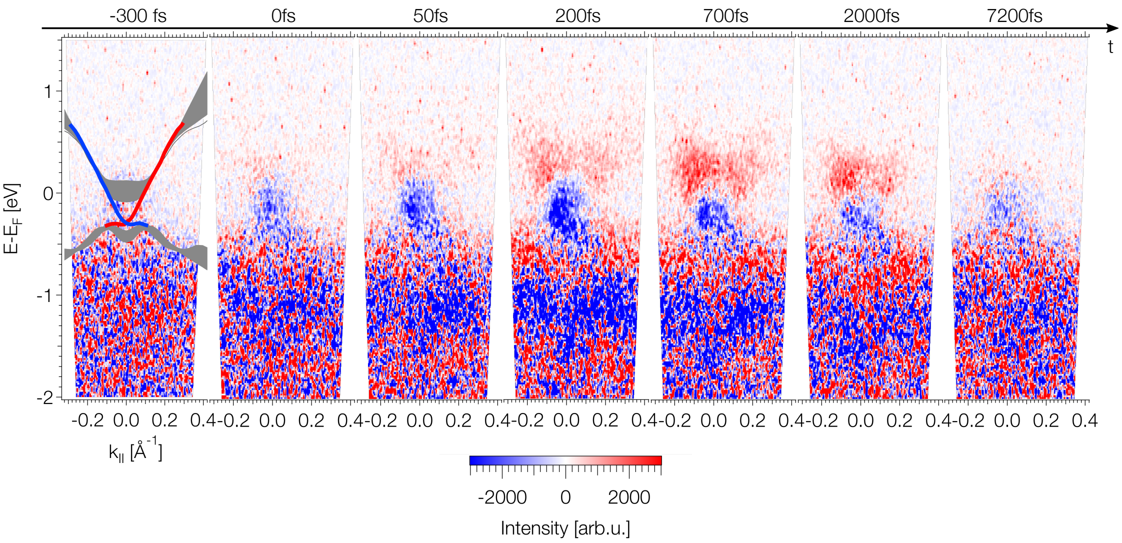

Figure 5.7 TrARPES at $\overline{\Gamma}$ for several selected time delays. The trARPES data for $t < 0$ were averaged and subtracted to illustrate only the change in intensity. The same intensity color scale is used for all plots. Red is intensity increase, blue decrease and white is no change in intensity. Theoretical bands [80] were added. Here red and blue indicate the opposite spins in the TSS.

In figure 5.7, trARPES data sets for seven selected time delays are introduced. Each delay step represents a difference map between the actual time step and the averaged spectra before time zero. The averaged spectra before time zero are used as reference and referred to hereafter as "onset". At −300 fs the electronic system is at equilibrium. Depletion due to excitation of the electrons from the valence bands and partially filled BCB and TSS into unoccupied states starts with the pump pulse at time zero and persists to large delays at 7.2 ps. The maximum depletion is reached after the pump pulse. The unoccupied BCB and TSS close to and above E_F are populated starting at roughly 50 fs and reach the maximum population at 700 fs. In contrast to the depletion of the occupied states, the excited BCB and TSS above E_F are not populated anymore at 7.2 ps.

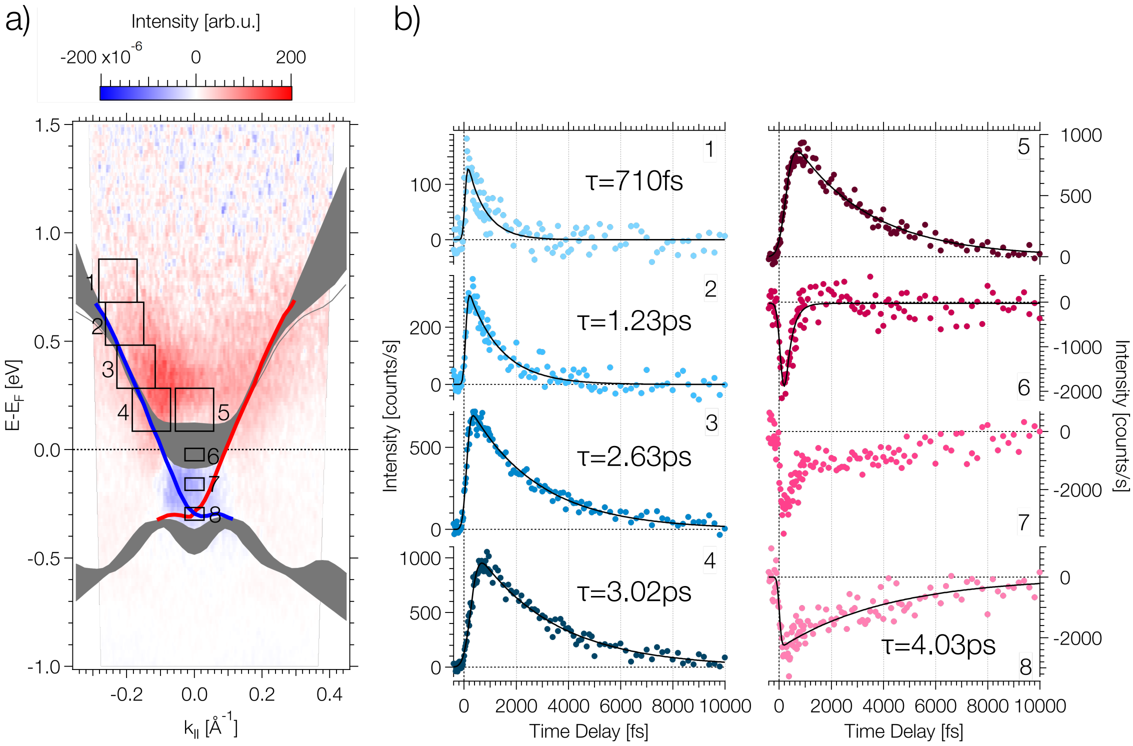

Figure 5.8 TrARPES data of the TSS and BCB. **a)** TrARPES map at $\overline{\Gamma}$ at $t = 300\,\mathrm{fs}$) with the onset subtracted. Band structure calculations from [80] are superimposed in the graph. Here red and blue indicate the opposite spins in the TSS. The energy alignment of the band structure calculations is based on the findings for the Dirac point and BCB. The color scale reflects intensity increase or decrease with red or blue, respectively. **b)** Transient intensities of the integration windows marked in a.

In figure 5.8 and 5.9, the electron and hole dynamics for the TSS and the BCB bottom at $\overline{\Gamma}$ are evaluated. Figure 5.8a displays the band structure at $t = 300\,\mathrm{fs}$ with the onset subtracted and divided by $\sum_i I(E, k_{\mathrm{i}||})$. Band structure calculations from Ref [80] were superimposed in the graph. The position of the Dirac point and the BCB bottom were aligned according to the data shown in figure 5.5. Numbered boxes define the integration areas of the time traces in the right panel. The time traces 1-4 show that the TSS decays with a single exponential and that the closer to the Fermi energy the larger are the time constants. The population decay time constant for the time trace 1 could be determined to be 710 fs, time trace 2 is 1.23 ps, time trace 3 is 2.63 ps and time trace 4 is 3.02 ps. The time constant of the electrons from 4 and 5 is nearly identical. Integration areas 5 to 8 represent depletion and the refilling of the holes. The BCB bottom (box 6) is refilled at roughly $t = 700\,\mathrm{fs}$ when the unoccupied part of the BCB (box 5) reaches the maximum intensity. Time trace 8 shows a slow refilling of the holes of the TSS with a time constant of 4.03 ps. Time trace 7 seems to have two different timescales. This could indicate that the integration range contains contributions from the fast process of the BCB and the slow refilling of the TSS.

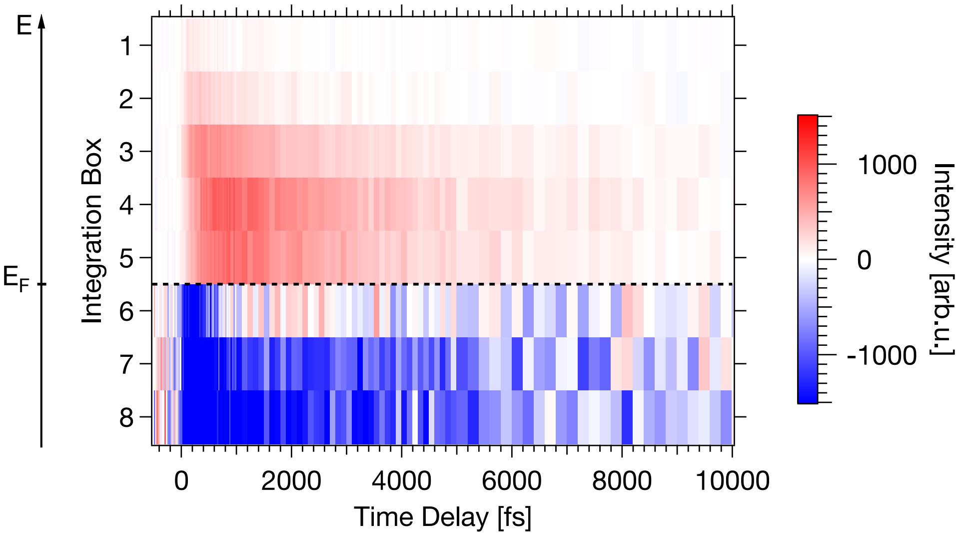

Figure 5.9 Integration areas 1-8 plotted versus time delay. The color scale is chosen to illustrate increase of intensity with red and decrease of intensity with blue.

In figure 5.9, the time traces 1 to 8 are plotted with the intensities being color-coded. Box 1-5 shows the shift of the intensity maximum to larger time delays and the increase of the time constant. By comparing integration box 5 and 6, it can be seen that when the maximum population of the unoccupied BCB and TSS above and close to E_F is reached, the previously occupied BCB bottom is already refilled. In contrast to that, the TSS below the BCB bottom is still being refilled.

5.5.2 High-symmetry points at the Brillouin zone boundaries

The trARPES measurements from the high-symmetry point $\overline{\mathrm{M}}$ are shown in the energy domain and in the time domain in figures 5.10 and 5.11, respectively.

Energy domain: The red and blue solid lines in figure 5.10 are EDCs after time zero at $\overline{\mathrm{M}}$ and $\overline{\mathrm{M}'}$, respectively, whereas the dashed lines depict the onset. The spectra are divided by $\sum_i I(E, k_{\mathrm{i}\|})$ before time zero to enhance weak features above E_F. The normalization function is plotted as a guide for the eye. The energy range -2.2 eV to -1 eV shows the depletion due to electron excitation into unoccupied states. Above -1 eV, an increase of intensity at -0.6 eV and the unchanged intensity in the band gap at -0.2 eV are observed. The increase of intensity at -0.6 eV is exaggerated due

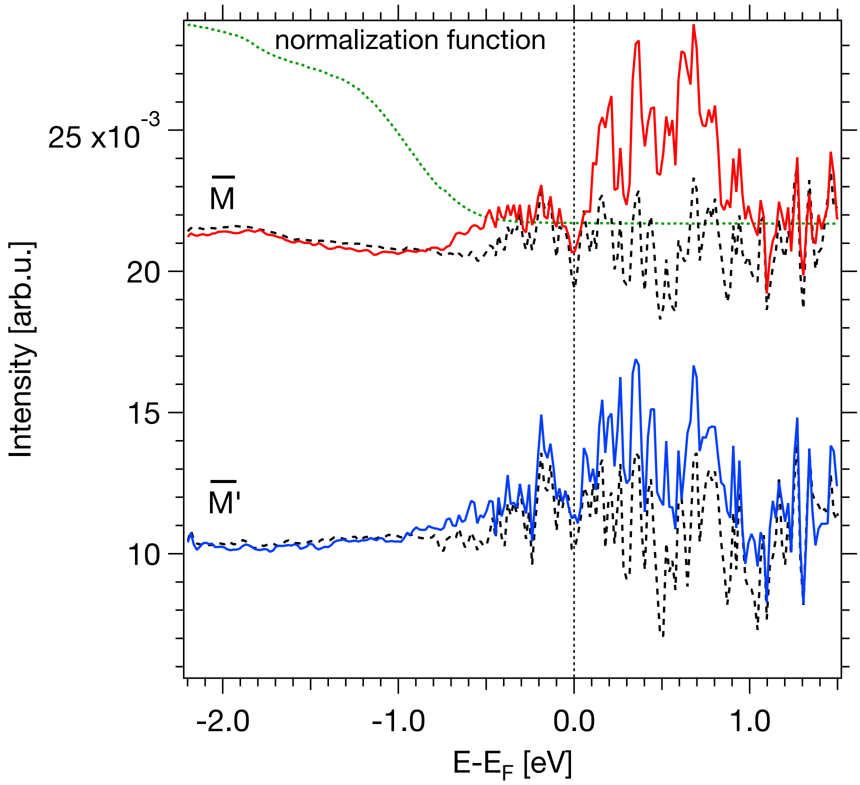

Figure 5.10 EDCs of the trARPES measurements at $\overline{\mathrm{M}}$ and $\overline{\mathrm{M}'}$ integrated over an angular window of 5 °. The data are normalized by the angle-integrated intensity before time zero. This normalization function (green dotted line) is plotted as a guide for the eye. The dashed curves are the EDCs at $t< 0$. The upper solid line (red) and the lower solid line (blue) correspond to the EDCs at $t = 200$ fs at $\overline{\mathrm{M}}$ and $\overline{\mathrm{M}'}$, respectively.

to the normalization. The width of the band gap is roughly 400 meV. The intensity increase at 0.5 eV above the Fermi level can be attributed to hot electrons excited into the BCB.

Time domain: The temporal evolution of the intensity is illustrated in figure 5.11. In 5.11**a)**, the depletion due to electron excitation from the valence band is shown. The maximum of the depletion is reached after 200 fs and does not recover within our measurement window of 10 ps. In 5.11**b)**, an intensity increase is found at −0.6 eV. The transient intensities for both high symmetry points $\overline{\mathrm{M}}$ and $\overline{\mathrm{M}'}$ exhibit two different timescales for the relaxation. Both timescales are indicated by the dotted lines (1) and (2) as a guide for the eye. Timescale (1) resembles a typical electronic excitation, reaching the maximum at 250 fs followed by an exponential decay. The second dynamic (2) is reminiscent of thermal effects due to heating of the lattice which reaches the maximum at roughly 3 ps. In 5.11**c)**, the transient intensity of the band gap just below the Fermi level at −0.2 eV is shown, which does not show any dynamics. In 5.11**d)**, the transient intensities at 0.5 eV above E_F are plotted. They illustrate the dynamics of the unoccupied conduction band at $\overline{\mathrm{M}}$ and $\overline{\mathrm{M}'}$. The population decay time constants of the conduction band at $\overline{\mathrm{M}}$ and $\overline{\mathrm{M}'}$ were fitted to be 1.02 ps and 1.27 ps, respectively.

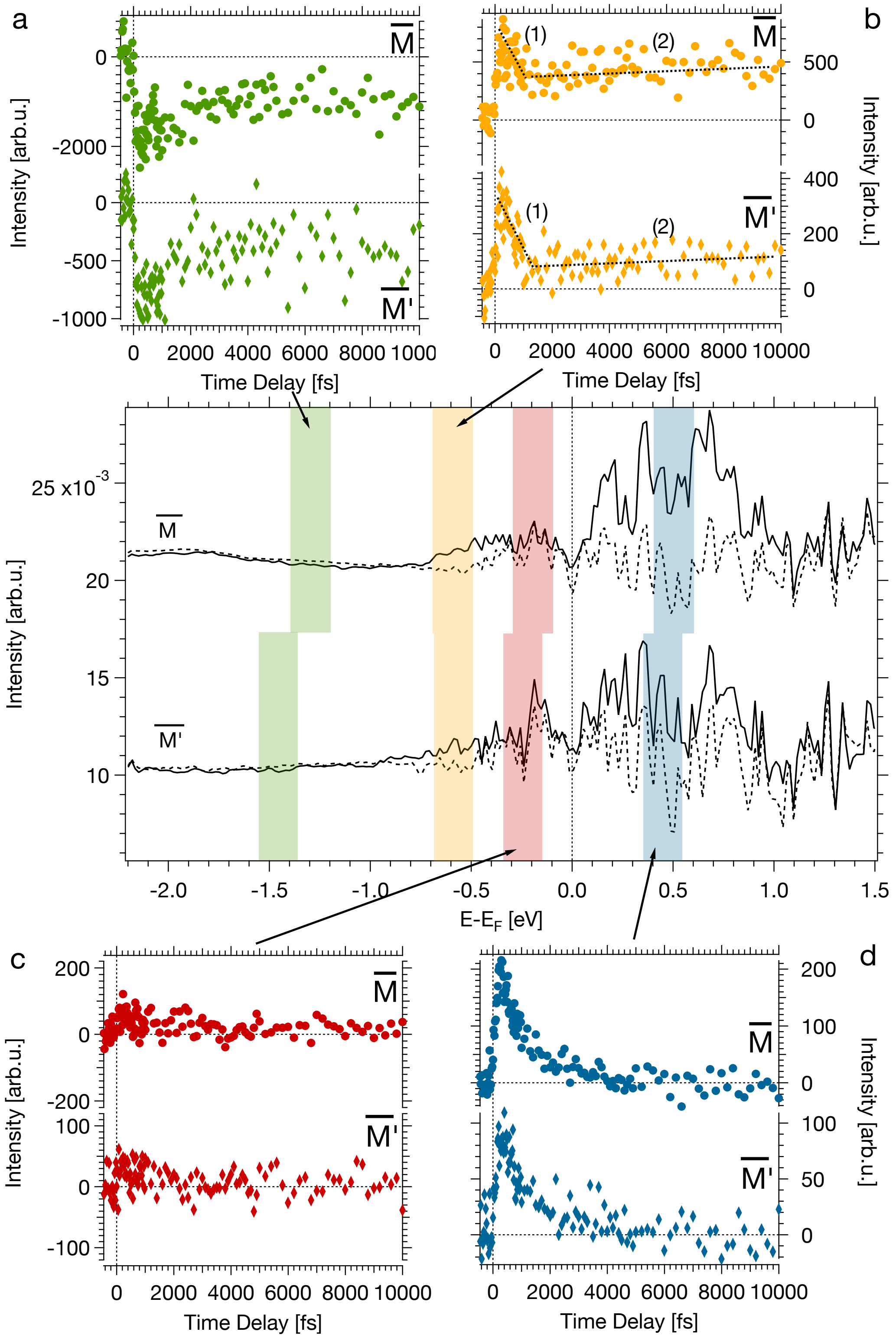

Figure 5.11 Transient intensities from $\overline{\mathrm{M}}$ and $\overline{\mathrm{M}}'$ at selected energies. **Middle panel:** EDCs from figure 5.10 with shaded markers for the integration areas. Top EDC at $\overline{\mathrm{M}}$ and bottom EDC at $\overline{\mathrm{M}}'$. **a, b, c and d:** Transient intensities for the occupied band structure (a and b), band gap (c) and the unoccupied BCB (d). The transients represent intensities without normalization.

5.5.3 Discussion

Electron dynamics at $\overline{\Gamma}$

Figure 5.12 outlines a possible model for the dynamics at $\overline{\Gamma}$.

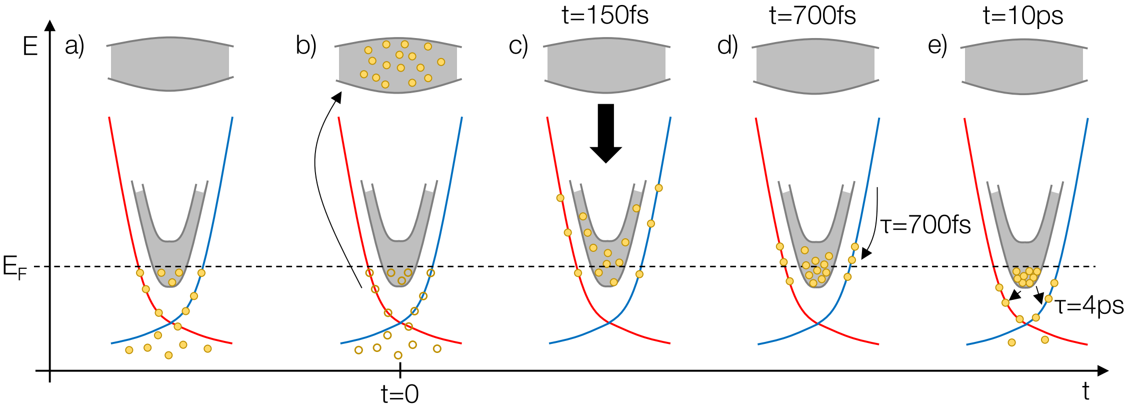

Figure 5.12 Schematic of electron and hole dynamics at $\overline{\Gamma}$ after excitation with 1.5 eV pump in n-type Bi_2Se_3. Adapted from [62].

a) At times $t < 0$ the complete electronic distribution is in equilibrium.

b) At $t = 0$, the electrons are excited into unoccupied states at higher energy by the pump pulse. This distribution of hot electrons in the bulk appears as diffuse features [62, 94] in the trARPES experiment.

c) The electrons then relax quickly down in energy by a cascade of scattering processes. At 150 fs after time zero, the TSS at $E - E_F = 0.8$ eV is already populated and the transient population reached its maximum.

d) The electrons scattering towards the Fermi energy refill the depleted BCB bottom within 700 fs which is equal to the instant of maximum electron population in the unoccupied TSS and BCB close to the Fermi level.

e) Electrons accumulate at the BCB bottom. Therefore, the BCB acts as a charge reservoir, slowly filling the TSS by interband scattering. It takes more than 10 ps to completely refill the TSS. The slow recovery has a time constant of 4.03 ps. Hajlaoui and Sobota presented similar results from Bi_2Te_3 [94] and p-type Bi_2Se_3 [62] where they showed that the TSS has a population decay time constant of 5.7 ps respectively 6 ps.

Electron dynamics at $\overline{\mathrm{M}}$

Diffusion and scattering In figure 5.13, the total electron yield of the occupied states at $\overline{\mathrm{M}}$ and $\overline{\mathrm{M}'}$ is shown.

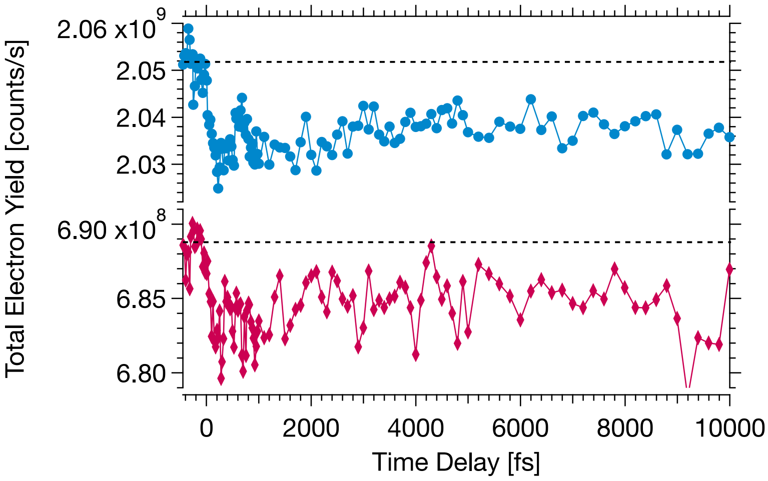

Figure 5.13 Total electron yield for the occupied states at $\overline{\mathrm{M}}$ and $\overline{\mathrm{M}'}$ integrated over the full angular window of the detector. The angular window covers 24 °, which is 0.55 Å^{-1} or 63 % of the BZ radius. The dashed lines depict the average yield before time zero.

After 200 fs the maximum depletion due to the electron excitation by the pump pulse is reached. The data illustrate that roughly 1 % of the electrons are excited into states at higher energy. Even after 10 ps the depletion does not recover. The fact that the intensity is not restored after 10 ps could be due to diffusion of the excited electrons out of the probed volume or due to lack of relaxation channels of the excited electrons in the BCB and TSS. The diffusion of the excited electrons out of the probed volume was studied for metallic films of different thicknesses on an insulating substrate [95]. It was shown that the excited electrons diffuse towards the bulk. Bi_2Se_3 is a layered material with van der Waals bonding between the quintuples and the bulk is insulating with charge carrier densities in the range of $5 \cdot 10^{18}\,\mathrm{cm}^{-3}$ [96] and $6 \cdot 10^{19}\,\mathrm{cm}^{-3}$ [97]. Conductivity measurements of nanowires with different orientation show anisotropic transport properties with conductivity along (111) cleavage planes which are $\sim$ 250x better than perpendicular to the planes [98]. Therefore diffusion towards the bulk is neglected here.

Another explanation is that the scattering rate from the BCB and TSS to the BVB is extremely low. In figure 5.14, the schematic for such a relaxation of the excited electrons to the BVB is illustrated. The scattering rate of 4.03 ps from the BCB into the TSS was already discussed. The second time constant for the transition from the TSS into the BVB could be expected to be above 10 ps by observing the

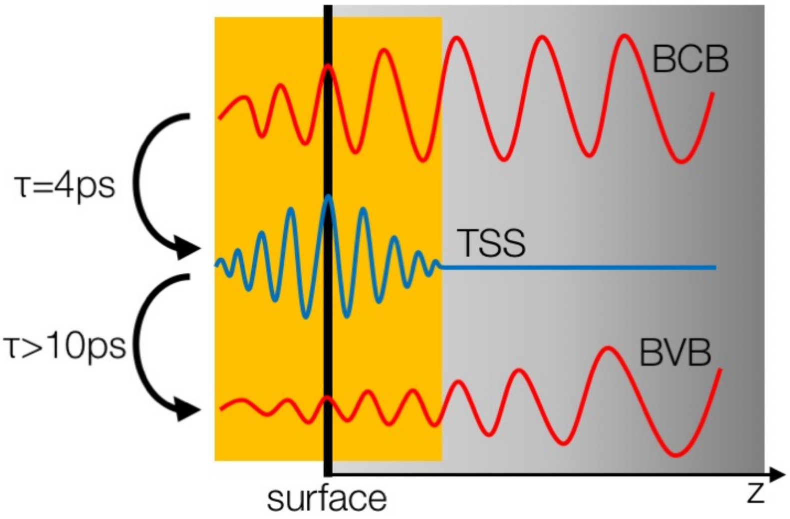

Figure 5.14 Sketch of the wave functions of BCB, TSS and bulk valence band (BVB) close to the surface. The relaxation channels and time constants for the excited electrons are illustrated.

total electron yield of the occupied states at $\overline{\mathrm{M}}$ and $\overline{\mathrm{M}}'$. Relaxation of the excited electrons in the conduction band at $\overline{\mathrm{M}}$ and $\overline{\mathrm{M}}'$ by electron-electron scattering is ruled out due to the energy gap. We assume that the excited electrons scatter to the TSS by phonons. We may conjecture that the overlap of the wave functions of the TSS and BVB is small which limits the probability for the excited electrons to scatter into the BVB as visualized in figure 5.14.

Conduction band In figure 5.15, the difference map of $t = 200\,\mathrm{fs}$ and $t < 0$ at $\overline{\mathrm{M}}$ is shown. The diamonds and circles are band structure calculations from Ref [87] for the high-symmetry directions ΓF and ΓL. The hot electron dynamics shown on the right hand side of figure 5.15 correspond to those of the bulk conduction band. The green triangles illustrate the position of maxima from the conduction band and the bars indicate their FWHM. At the $\overline{\mathrm{M}}$-point, the conduction band is centered at $E - E_\mathrm{F} = 0.52\,\mathrm{eV}$ with a FWHM of 620 meV and shows a population decay time constant of 1.02 ps. The energy position of 0.8 eV above the Dirac point at $\overline{\Gamma}$ is in good agreement with the conduction band at $\overline{\mathrm{M}}$ and $\overline{\mathrm{M}}'$ predicted in Refs [86, 87].

Broadening Furthermore, an increase of the intensity in the occupied states can be observed in figure 5.15. This may either be due to a rigid shift or to a broadening of the bands. The EDCs of $t = 200\,\mathrm{fs}$ and $t < 0$ at $\overline{\mathrm{M}}$ are compared in figure 5.16. The data were fitted by a Gaussian with a polynomial background. The Gaussian shows a peak shift of $\sim 1\,\mathrm{meV}$ and a broadening of 25 meV compared to 576 meV

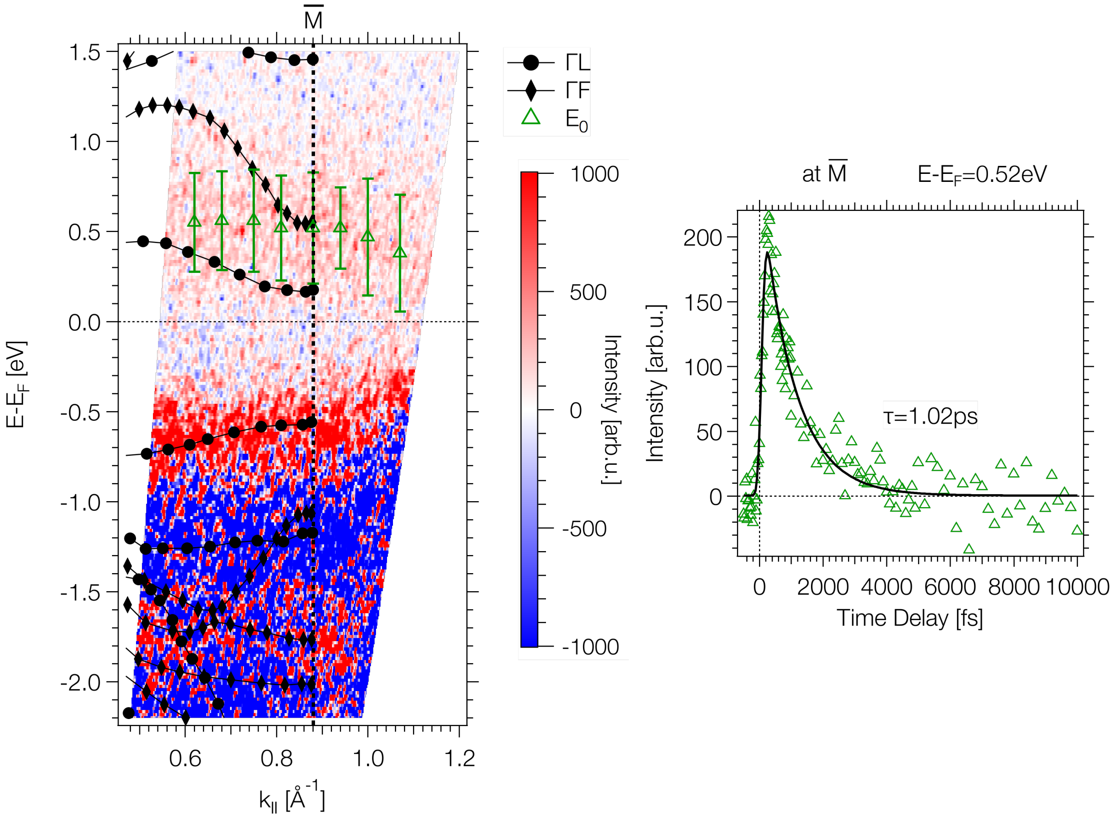

Figure 5.15 **Left:** TrARPES at $\overline{\mathrm{M}}$ for $t = 200$ fs with onset subtracted. The diamonds and circles are band structure calculation from Ref [87] for the high-symmetry directions ΓF and ΓL. The green triangles correspond to the position of the conduction band and the FWHM is shown by the vertical bars. **Right:** The transient intensity for the conduction band at $\overline{\mathrm{M}}$ taken at 0.52 eV. The time constant is $\tau = 1.02$ ps.

FWHM at $t < 0$. Therefore, the shift can be neglected but not the broadening which is the apparent reason for the intensity increase.

The slow recovery of the intensity increase of the occupied states at $\overline{\mathrm{M}}$ and $\overline{\mathrm{M}'}$ could have several reasons.

(i): One of them is photoinduced band bending due to surface photovoltage (SPV). It has been shown that the downward band bending in n-type Bi_2Se_3 extends to 20 nm into the bulk with a maximum amplitude at the surface of 0.26 eV [91, 93]. The band bending in Bi_2Se_3 is an aging effect due to contamination with the residual gas [92]. Our experiments were performed within eight days after the sample was cleaved in-situ and spectra at $\overline{\Gamma}$ were taken regularly without observing shifts in the band structure. Therefore, we assume that the band bending due to aging is saturated.

Figure 5.17 illustrates the SPV effect in the case for downward band bending. Therefore, upon creation of electron-hole pairs, the band bending represents a potential

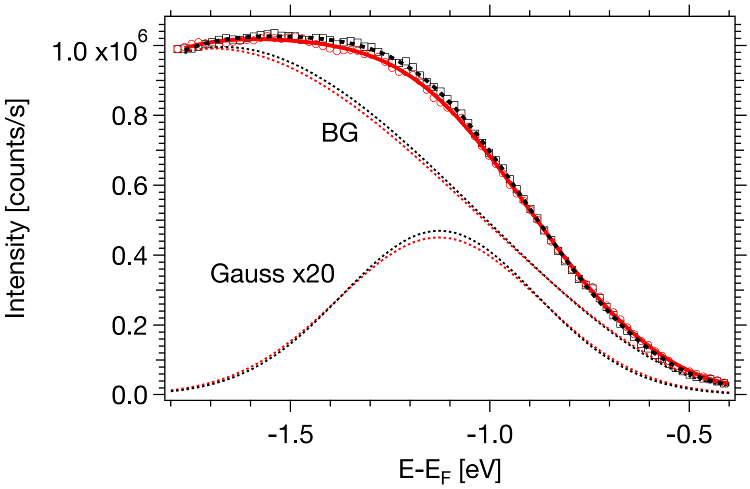

Figure 5.16 EDCs for $t = 200$ fs (red circles) and $t < 0$ (black squares) at $\overline{\mathrm{M}}$. The integration window of the EDCs was 5 °. The data were fitted by a Gaussian with a polynomial background. The fitting result for $t = 200$ fs and $t < 0$ are the solid red and dashed black line, respectively.

gradient. Thus, the charges are separated which leads to an accumulation of electrons at the surface and holes in the bulk. The excess of electrons at the surface reduces the band bending potential V_{BB} by the surface photovoltage V_{SPV}. As a result, the bands observed in trARPES are expected to undergo a rigid shift [99]. As shown before in figure 5.16, no rigid shift was observed. Furthermore, the time delay dependence of the SPV was studied for different semiconductors [100–102]. The results indicate that the timescales for the SPV are in the range of hundreds of picoseconds. Thus, we rule out the SPV effect responsible for the intensity increase in the occupied states.

(ii): A second explanation is based on lattice heating due to the pump pulse. The impinging pump fluence for all measurements was $226\,\mu\mathrm{J\,cm}^{-2}$. In Ref [103], the dielectric functions as function for bulk Bi_2Se_3 are given. For 1.5 eV pump photon energy, the reflectance is 40 % and the penetration depth 26 nm [97]. The spot size diameter was $420\,\mu$m. Thus, the pulse energy of $0.188\,\mu$J is deposited in a volume of $3.6 \cdot 10^{-9}\,\mathrm{cm}^3$. Moreover, with the heat capacity of $125\,\mathrm{J\,mol}^{-1}\,\mathrm{K}^{-1}$ [104] and $4 \cdot 10^{-11}$ mol of charge carriers in the excited volume, a change of $\Delta T \sim 36$ K for the lattice is expected. In metals, the temperature rise of 36 K together with the electron-phonon coupling parameter $\lambda = 0.62$ [105] would result in a broadening of $\pi \cdot \lambda k_B \cdot \Delta T \sim 6$ meV. Fraxedas et al. studied the temperature dependence of photoemission peaks of bulk and surface states [106, 107] of III-V semiconductors. At high temperature as compared to the Debye temperature (185 K for Bi2Se3 [108]), the temperature dependence can be well approximated by a linear function. The

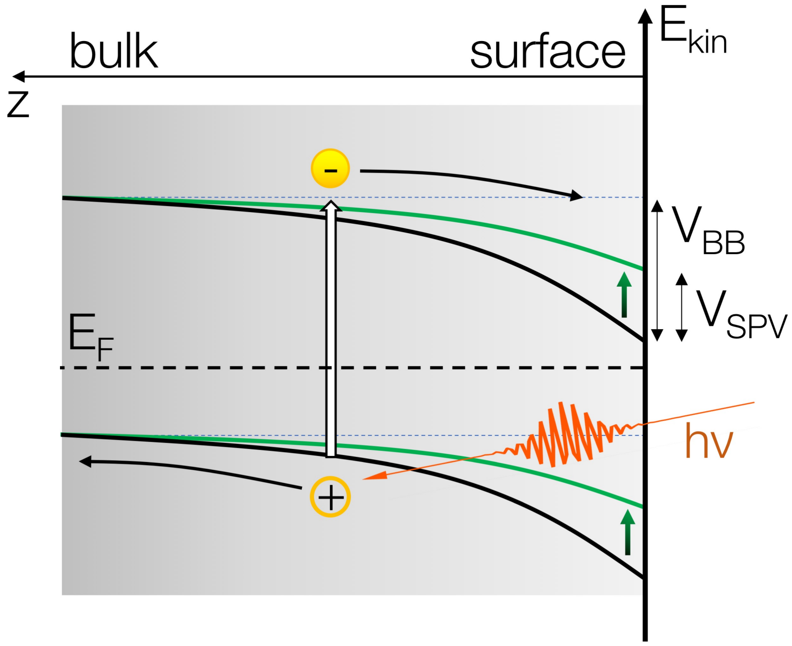

Figure 5.17 Schematic of the SPV effect. The excitation of an electron by light leaves an hole behind. Due to the natural downward band bending (V_{BB}), the electron will move to the surface and the hole into the bulk. This accumulation of electrons close to the surface lowers the effect of the initial band bending by the photovoltage V_{SPV}. Figure adapted from [99].

proportionality constants are in the range between 0.1 and 0.5 for typical transitions depending on DOS and final state contribution. Using 0.5 meV K^{-1} we obtain an additional broadening of about 17 meV for a transient lattice temperature rise of about 36 K. This is close to the value of 25 meV found in our experiments giving evidence that the broadening is due to the increase in lattice temperature.

5.6 Conclusions

The topological insulator $\mathrm{Bi_2Se_3}$, was the first system examined by pump-probe technique with the new high harmonic light source.

It could be demonstrated, that the TREx setup with the high harmonic light source is a suitable setup to measure out-of-equilibrium electron dynamics on solids. The TSS at $\overline{\Gamma}$ could be populated by the 1.5 eV pump pulse and the relaxation of the excited electrons was observed. The large time constants for the refilling of the TSS below the BCB bottom can be attributed to the latter being a charge reservoir and slowly releasing electrons to the surface state by interband scattering.

At the high symmetry points $\overline{\mathrm{M}}$ and $\overline{\mathrm{M}'}$, the population of the BCB at 0.52 eV above the Fermi level was observed. The population decay time constant of the BCB was found to be 1.02 ps. Furthermore, the depletion within the BVB was observed with a time constant of > 10 ps. The large time constant is conjectured to be a result of the excited electrons in the BCB not being able to relax by electron-electron scattering due to the energy gap but by interband scattering to the metallic TSS by phonons. The intensity increase due to a broadening of the BVB is conjectured to be due to lattice heating. The broadening of the BVB of 25 meV is in a good order of magnitude compared to the calculated broadening of 6 meV and 17 meV.

6 TBA/Au(111): Outlook for time-resolved photoelectron diffraction

6.1 Time-resolved photoelectron diffraction

The goal of a time-resolved photoelectron diffraction (trPED) experiment is to observe the dynamics of structural changes in real-time with chemical sensitivity and femtosecond temporal resolution.

Photoelectron diffraction (PED) offers the possibility to study structural properties of single-crystalline surfaces and ordered adsorbates. The emitted photoelectron can be considered as a wave propagating through the crystal, which is scattered at the atomic potential of the neighboring atoms (cf. figure 6.1a). In the far field, all the waves coming from the same emitter interfere to form a diffraction pattern [22].

XPD is a particular case of PED, where the photoelectrons are excited with high photon energies (typically $h\nu > 500\,\mathrm{eV}$) and the pattern is dominated by sharp spots which correspond to the real-space vectors between emitter and scatterers. The magnitude of the the scattered electron wave ϕ_s is defined by the form factors $f(\theta_\mathrm{s})$. In figure 6.1b, the form factors for photoelectrons with a kinetic energy of 723 eV scattering off an oxygen atom or rhodium atom are illustrated. The scattering is dominant in the forward direction $\theta = 0$ because of constructive interference. This phenomenon is known as forward focussing or forward scattering. Thus, the intensity maxima in the diffraction pattern are the result of forward scattering.

The next step is photoelectron diffraction in a pump-probe scheme. This would allow to observe changes of the real-space lattice vectors between emitter and scatterer in real-time [109]. In view of observing molecular motion, one particular challenge for time-resolved photoelectron diffraction is, that only a small fraction of molecules are

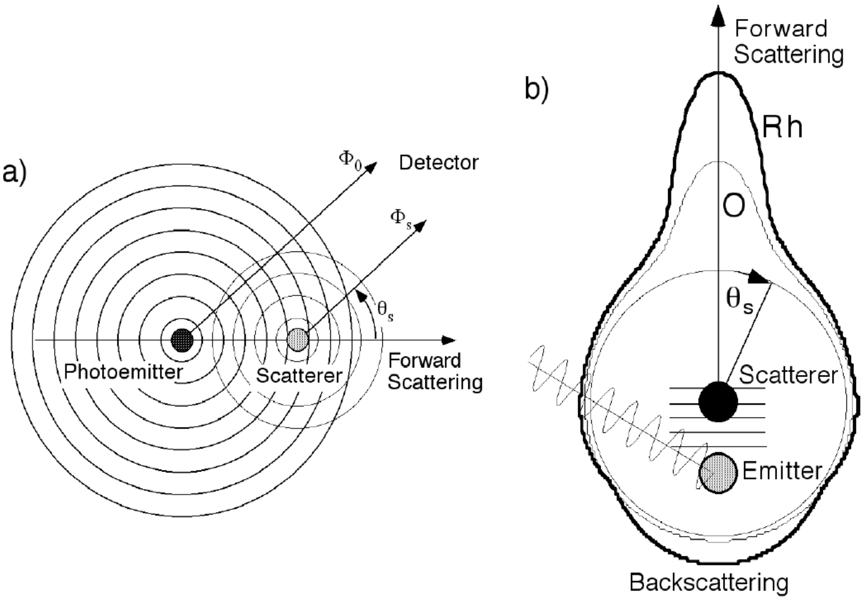

Figure 6.1 **a)** Outline of the scattering process. The emitted photoelectron wave is scattered at the neighboring atom. In the far-field all the waves interfere and form a diffraction pattern. **b)** At high photon energies, the scattering amplitude with respect to θ_s is largest for forward scattering. The sketch shows the form factor $f(\theta_\mathrm{s})$ for photoelectrons with a kinetic energy of 723 eV scattered at a oxygen atom and rhodium atom. This figure is taken from [22].

excited and change their structure. It has to be clarified if this method is sensitive enough to observe these changes with a large background of unchanged molecules.

6.2 Model system: TBA/Au(111)

Organic molecules that undergo pronounced and reversible conformational changes are an important functional class among molecules. They can be used in materials and devices for interesting optoelectronic and optomechanical applications [110, 111]. A well-known molecule which changes the arrangement of the atoms when illuminated with light is azobenzene [17, 112]. Azobenzene was found to adsorb on Au(111) in ordered monolayers[113], but the photoswitching ability is not preserved. Reducing the binding to the surface by attaching four tert-butyl ligands to the phenyl groups, allows the molecule to maintain the switching ability on a metal surface.

The photoelectron diffraction data of tetra-tert-butyl-azobenzene on Au(111) are taken once in thermal equilibrium and once with illumination. The first data set corresponds to an ensemble of mostly *trans* isomers. The photostationary state (PSS) corresponds to a certain ratio of *trans* and *cis* isomers which depends on the experimental parameters like e.g. temperature, illumination spectrum, illumination intensity,... Thus, the second data set is taken after shifting the PSS to increase the amount of *cis* isomers using a He discharge lamp. This allows us to generate difference maps which reveal the structural change between both isomers. Furthermore, from those difference maps the fraction of excited molecules could be determined for this particular experiment.

6.3 This work was published in Structural Dynamics

This chapter is a reprint of the publication:

A. Schuler, M. Greif, A.P. Seitsonen, G. Mette, L. Castiglioni, J. Osterwalder and M. Hengsberger, *Sensitivity of photoelectron diffraction to conformational changes of adsorbed molecules: Tetra-tert-butyl-azobenzene/Au(111)*, Structural Dynamics **4**, 015101 (2017)

Abstract

Electron diffraction is a standard tool to investigate the atomic structure of surfaces, interfaces, and adsorbate systems. In particular, photoelectron diffraction is a promising candidate for real-time studies of structural dynamics combining the ultimate time resolution of optical pulses and the high scattering cross-sections for electrons. In view of future time-resolved experiments from molecular layers we studied the sensitivity of photoelectron diffraction to conformational changes of only a small fraction of molecules in a monolayer adsorbed on a metallic substrate. 3,3',5,5'-tetra-tert-butyl-azobenzene served as test case. This molecule can be switched between two isomers, *trans* and *cis*, by absorption of ultraviolet light. X-ray photoelectron diffraction patterns were recorded from tetra-tert-butyl-azobenzene/Au(111) in thermal equilibrium at room temperature and compared to patterns taken in the photostationary state obtained by exposing the surface to radiation from a high-intensity helium discharge lamp. Difference patterns were simulated by means of multiple-scattering calculations which allowed us to determine the fraction of molecules that underwent isomerization.

Introduction

Small organic molecules that undergo pronounced and reversible conformational changes upon photoexcitation represent an important class of molecular switches. They can be used as building blocks in materials and devices with promise for interesting optoelectronic and optomechanical applications [110, 111, 114]. Adsorbed on surfaces, they are of interest in the context of molecular electronics and smart surfaces where they may introduce functionalities that can be controlled by light of specific wavelengths. For this purpose one would like to characterize their switching behavior in the adsorbed state in terms of structural rearrangements and structural dynamics.

The photo-induced *trans* to *cis* isomerization in azobenzene along the N=N double bond connecting the two phenyl rings is an early example of photo-switching [115, 116] that has been studied in great detail in solution later on [117]. Azobenzene was found to adsorb on Au(111) in well-ordered monolayers [113]. However the photo-switching ability of the molecule is not preserved, most likely due to the presence of short-lived electronic states in the metal substrate, which dissipate energy before the conformational change is finished [17]. The coupling to the surface can be reduced by the attachment of four tert-butyl (TB) ligands to the 3 and 5 positions of the two phenyl groups of the azobenzene molecule. These spacers allow the molecule to maintain the switching ability on a metal surface. Indeed, the light-induced *trans-cis* isomerization of tetra-tert-butyl-azobenzene (TBA) adsorbed on Au(111) has been observed by scanning tunneling microscopy [17] and by two-photon photoemission spectroscopy [112].

The pronounced structural changes in the TBA/Au(111) system associated with the *trans-cis* isomerization have been studied experimentally by means of near-edge x-ray absorption fine structure (NEXAFS) [118] and theoretically by density functional theory (DFT) [119]. The *trans* isomer adsorbs in a nearly planar geometry with both phenyl rings parallel to the surface. In the *cis* isomer one of the phenyl groups flaps up by ≈ 30° while the second one finds itself perpendicular with respect to the surface normal [118], as shown in Fig. 6.2 (bottom part). In the present work it is explored to what degree this structural rearrangement can be detected via x-ray photoelectron diffraction (XPD) [22], which can in principle provide very detailed and precise information on adsorbate geometries [120, 121]. This is done in view of future time-resolved XPD experiments with femtosecond resolution in a pump-probe scheme [122, 123] that may shed light on the switching dynamics.

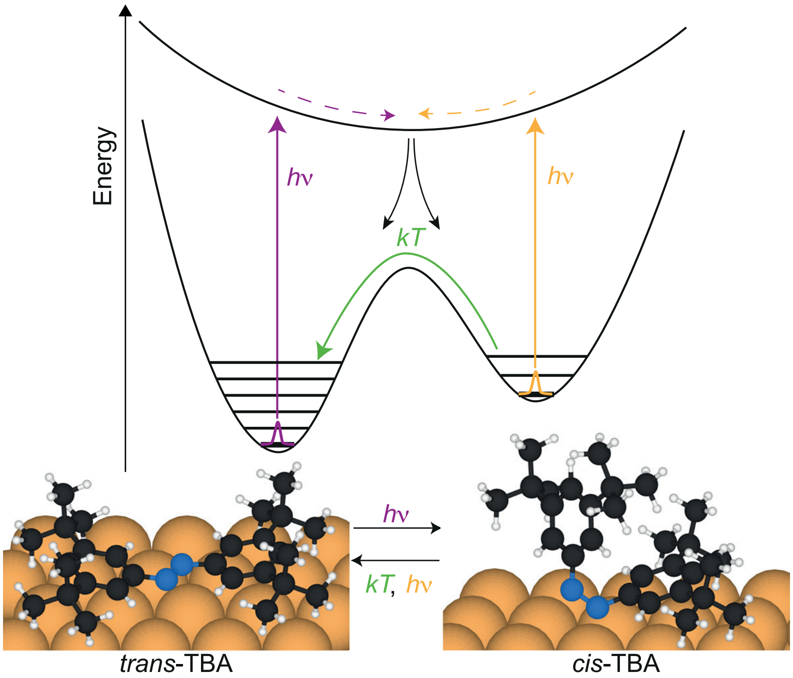

Figure 6.2 Schematic diagram of the photoisomerization process: TBA adsorbed on a Au(111) surface exhibits two different structural configurations, *trans* and *cis*. Since the energy minimum of the *cis* isomer is significantly more shallow than the one of the *trans* isomer, the net thermal transition rate drives the molecule towards the *trans* state [18]. The molecule can be switched between *trans* and *cis* by absorption of light as depicted by the dashed arrows [112].

In XPD an electron is promoted from a core-level to a continuum of free-electron-like states by absorption of an x-ray photon. The photoelectron wave propagates from the emitting atom through the surface and is partially scattered by neighboring atoms, thus generating an interference pattern by coherent superposition of direct and scattered waves [22]. The angular intensity distribution is recorded as a function of emission direction. At kinetic energies of a few hundred eV XPD patterns are dominated by relatively narrow forward focusing peaks [124]. These diffraction maxima are caused by small-angle scattering where the scattering form factor is strongly peaked. Thus, these maxima in the photoemission intensity distribution directly indicate real-space vectors between the emitter site and other atomic sites.

One particular challenge for time-resolved XPD studies of molecular switches will be that, for low pump fluence, only a small fraction of the adsorbed molecules may undergo the *trans-cis* isomerization, and that the isomerization dynamics will follow many different trajectories. Since photoemission samples a macroscopic surface area, the XPD pattern represents a superposition of many coexisting conformations [122]. The goal of the present work is to compare the XPD pattern from a monolayer of TBA molecules on Au(111) in thermal equilibrium at room temperature with a XPD pattern obtained from the same ensemble of molecules during exposition to ultraviolet radiation from a continuous high-intensity source. The differences in the patterns are related to conformational changes of the excited molecules. In combination with scattering calculations, the quantitative analysis of the XPD patterns allows the fraction of excited molecules to be determined.

The *trans* isomer is the stable ground state of the azobenzene molecule, with the *cis* isomer slightly higher in energy and separated by a high barrier in the potential energy surface (Fig. 6.2, top part). In solution the absorption of ultraviolet (UV) light ($\approx$ 365 nm) can promote it to the *cis* state via $\pi \rightarrow \pi^*$ (S_2) excitation. The reverse reaction can be triggered with high quantum yield by blue light ($\approx$ 420 nm) [116, 125] by $n \rightarrow \pi^*$ (S_1) excitation. Depending on the excitation wavelength and light intensity, a so-called photostationary state (PSS) is established in an ensemble of azobenzene molecules with a defined *cis*-to-*trans* ratio. Adsorbed on a surface, the situation is different in that the absorption spectra change and any photon with energy > 2 eV can trigger isomerization in either direction [18]. It has been shown that the excitation proceeds predominantly via electron-hole pair creation in the metal substrate followed by a positive ion resonance due to charge transfer of holes from the substrate d-bands into the HOMO [126]. A more detailed discussion can be found in Section 6.3.

Experiment

Data acquisition

The Au(111) surface was prepared by cycles of sputtering and annealing in order to obtain a clean and highly-ordered surface. The surface quality was checked by means of x-ray and ultraviolet photoelectron spectroscopy (XPS and UPS, respectively) and low-energy electron diffraction. TBA was synthesized and characterized according to the procedure given in Alemani *et al* [127]. The preparation and adsorption behaviour of TBA on Au(111) is discussed in detail by Hagen *et al*[128]. The molecules were evaporated onto the surface from TBA powder with a home-built Knudsen cell at a temperature of 370 K. The substrate was held at 410 K during deposition [128]. The coverage of the molecular layer is important: In the compressed phase (1 ML=1 monolayer), the molecular interactions are presumed to be stronger and the phenyl rings are tilted with respect to the surface whereas in the relaxed phase (coverages up to 0.9 ML) they lie parallel to the substrate for the *trans* isomer [112]. The coverage was controlled during deposition by monitoring the work function change [129] and after deposition determined by means of XPS. All data presented here were taken for 0.9 ML TBA/Au(111).

The photoemission data were recorded at room temperature and at a pressure of $p < 3 \cdot 10^{-10}$ mbar during the measurement without He lamp in a modified version of the VG Escalab 220 spectrometer [130]. For the XPS/XPD measurements, photons from the Mg Kα line ($h\nu = 1253.6$ eV) were used. The five-axis sample goniometer of the manipulator allows one to rotate the sample orientation in order to map the photoemission intensity distribution over the full hemisphere above the sample surface. Every angular setting, and thereby every data pixel represents emission into a solid angle of the same size. The data were background corrected by subtracting a background function slowly varying with the polar emission angle, and averaged taking advantage of the three-fold rotational symmetry of the substrate around the surface normal. For visualization they are represented in stereographic projection. A more detailed description of the data treatment will be given in Section 6.3.

A microwave-driven high-intensity He discharge source (VUV5000, Gammadata AB) [131] with the monochromator set to zero order was used to expose the molecules to visible and near-UV radiation, which is dominated by lines at wavelengths of 388 nm, 402 nm, 447 nm and 505 nm, respectively [132]. Moreover, very strong emission is found at 58.4 nm (21.2 eV, HeI), and two weaker lines lie at 53.7 nm and 30.4 nm in the vacuum ultraviolet (VUV) [131]. It is known from scanning tunneling microscopy (STM) [17, 133] and two-photon-photoemission (2PPE) [112, 126] measurements that prolonged exposure of molecules to UV radiation drives the TBA/Au system into a photostationary state. The ratio of *cis* and *trans* isomers in dynamical equilibrium, *i.e.* the PSS is given by the ratio of the cross-sections for the two photo-induced transitions and the thermal transition rate [134]. The time needed to reach the PSS depends essentially on the total isomerization cross-section and on the photon flux. By comparing the photon flux and photon-energy dependent cross-sections from previous work [17, 112, 126] with those from our He discharge lamp, we estimate the time required to drive the system into the dynamical equilibrium to be less than one hour (see the quantitative analysis presented below in Section 6.3). This was confirmed *a posteriori* by the observation that we switched on the He lamp about one hour before starting the actual measurement and obtained consistent results for the different runs and for the different angular settings used during the 10-12 hours of data acquisition.

Electron Diffraction in Atomic Clusters (EDAC) calculations

XPD patterns were simulated by multiple-scattering cluster calculations using the *electron diffraction in atomic clusters* (EDAC) code [135], which has been shown to describe experimental data well [136]. Briefly, the calculations are based on interference of the direct wave and waves scattered several times by the atoms surrounding the emitter. The coherent sum is then evaluated at the position of detection in the far field. The computations are done by using a cluster model of the substrate, which allows adsorbed molecules to be included in a straightforward fashion [121]. The atomic positions of the *trans* and *cis* isomers of TBA adsorbed on Au(111) were taken from the DFT calculation of McNellis *et al.* [119]. The two clusters consist of a single TBA molecule (*trans* and *cis*) on a gold (111) substrate. The total number of atoms in one cluster is $N = 150$. The atomic coordinates served as input to EDAC calculations, which are shown in Fig. 6.3a and b beside the atomic structures predicted by DFT. The kinetic energy for the simulations was 854 eV, which corresponds to emission from the N 1s core-level (binding energy of ≈400 eV) with photons from the Mg Kα line ($h\nu = 1253.6$ eV).

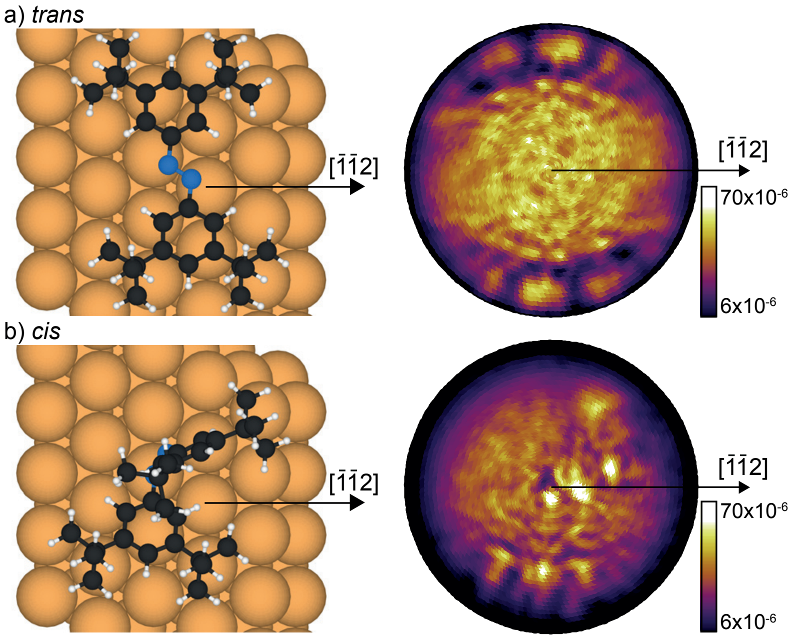

Figure 6.3 Hard sphere models and corresponding simulated scattering patterns of single TBA molecules in two different configurations: a) *trans* isomer and b) *cis* isomer. We assumed emission from the N 1s level using Mg-Kα radiation ($E_{kin} \approx 854$ eV). The orientation of the substrate is the same, the horizontal corresponding to the direction $[\bar{1}\bar{1}2]$ as indicated. The adsorption geometries and the atomic positions were taken from McNellis *et al*[119].

Results and qualitative analysis

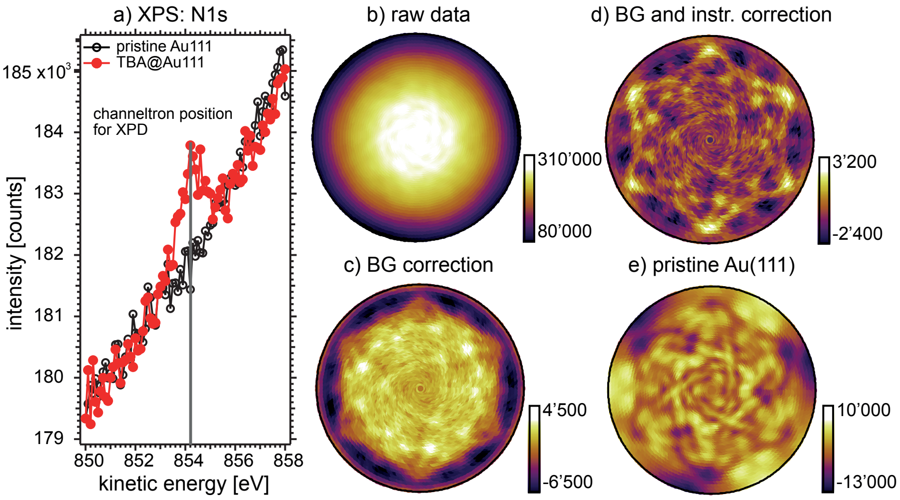

Figure 6.4 Data acquisition and data treatment: a) Experimental XPS spectrum. The red peak is due to emission from the N 1s state. The intensity of this peak is recorded as a function of the emission angle which results in the raw XPD pattern b). c) N 1s XPD pattern after subtraction of the spectral background. d) Final diffraction pattern after subtracting a Gaussian background in order to compensate for instrumental effects. e) Spectral background measured for the same kinetic energy $E_{kin} \approx 854\ eV$ on the bare Au(111) surface.

The two simulated N 1s XPD patterns of Fig. 6.3 illustrate the pronounced differences that one would measure for an individual molecule that undergoes the *trans-cis* isomerization. At the kinetic energy of 854 eV, the XPD patterns are dominated by forward scattering (see the work of Greif *et al.*[121] and references therein). As can be seen in Fig. 6.3a, the dominant forward focusing peaks in the diffraction pattern for the nearly planar *trans* isomer appear near grazing emission and along azimuthal directions near ±90° away from the $[\bar{1}\bar{1}2]$ direction. They correspond to forward focusing by the nearest carbon atoms, one for each nitrogen emitter. Carbon scatterers further away contribute less pronounced signals, because several of them lie within a narrow cone such that their scattering signals become strongly entangled. Intensities at lower emission angles arise due to higher order intramolecular scattering and backscattering from the substrate.

The *cis* isomer is far from planar since one of the phenyl moieties of the TBA is flapped up perpendicular to the surface while the second one is slightly tilted upwards [119] (see Figs. 6.2 and 6.3b). Therefore, forward focusing signals now appear at angles closer to normal emission than for the *trans* isomer, forming a complex pattern with little symmetry. The brightest spots near the centre belong to the nearest carbon atoms of the phenyl ring which is flapped up. The three less intense forward focusing maxima which can be found at higher emission angles near the bottom of the pattern are linked to the second, slightly tilted phenyl.

In order to demonstrate the sensitivity of the method to conformational changes of a small fraction of TBA molecules we recorded two experimental XPD patterns for two different states: The first pattern was recorded without additional UV source (*trans* only). The second pattern was taken while the sample was illuminated with the He high-intensity lamp with the monochromator in zero order. This led to a photostationary state with a specific ratio of *cis* to *trans* molecules.

The experimental procedure is visualized in Fig. 6.4 for a data set measured without UV illumination of the sample: The intensity of photoelectrons at the N 1s core-level position was recorded as a function of emission angle and displayed in stereographic projection, just like the EDAC simulations of Fig. 6.3. It is important to note that each pixel represents emission into a well-defined and constant solid angle. The raw data pattern (Fig. 6.4b) is essentially featureless except for a marked polar dependence. To make the intramolecular diffraction features visible, the spectral background underneath the N 1s peak was subtracted. This background was measured on a bare, clean Au(111) surface. It is not featureless, but contains signatures of photoelectrons produced deep below the Au(111) surface as a consequence of multiple elastic and inelastic scattering within the fcc lattice [137]. This particular way of background subtraction is not the standard procedure in XPD experiments, where normally the background is determined from intensity measurements to the left and right of the peak of interest and subsequent interpolation [22]. In the present case the standard procedure did not succeed mostly due to the very steep inelastic background (Fig. 6.4a). Finally, a two-dimensional Gaussian function centered at normal emission was subtracted from the data in order to remove polar dependencies related to instrument geometry. This includes the varying probe volume, x-ray spot size on the surface and changing inelastic attenuation length of the photoelectrons [138]. Since we are interested in slight changes of the signal, only a minimum of data treatment shall be applied here. The same procedure was applied to the data taken with the sample being irradiated by UV light.

When comparing the measured XPD data of Fig. 6.4d, which should correspond to the *trans* isomer, to the EDAC simulations, one has to consider one more step: owing to the three-fold symmetry of the Au(111) surface, the simulated pattern needs to be symmetrized by summing up three patterns rotated by 120° with respect to each other. In Fig. 6.5 the experimental data are compared to the symmetrized results of the EDAC calculations. The agreement is good at large polar angles for the

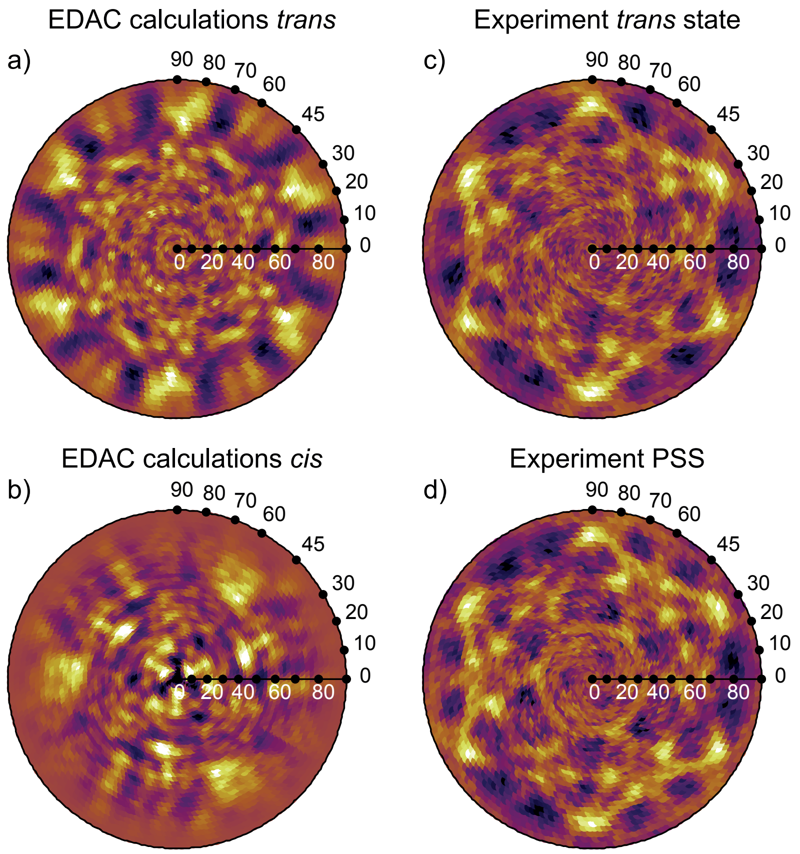

Figure 6.5 Comparison of simulated and experimental patterns: a) and b) EDAC calculations after three-fold averaging for *trans* and *cis* isomers, respectively. c) and d) experimental XPD patterns for N 1s emission in *trans* and photostationary state, respectively.

trans isomer: The six maxima related to nitrogen-carbon forward focusing between $70-80°$ appearing in the EDAC calculation for the *trans* isomer (Fig. 6.5a) can also be found in the experimental pattern (Fig. 6.5c). Some of the finer structures seen in the experiment are also reproduced. Remaining discrepancies might call for a refinement of the structural parameters, but this is beyond the scope of this work.

The XPD data from the UV illuminated sample, which was in a photostationary state with so far unknown *cis:trans* ratio, are shown in Fig. 6.5d. The pattern is very similar to the one from the non-illuminated sample, with very subtle changes. This suggests that the *cis:trans* ratio is rather small. Accordingly, none of the features of the symmetrized *cis* state pattern (Fig. 6.5b) can be clearly recognized.

In order to verify that the signal changed upon illumination we subtracted the raw data of the experimental patterns recorded in PSS and *trans* from each other after careful normalization for x-ray flux using reference measurements on the bare substrate. No background subtraction or correction for instrument functions was

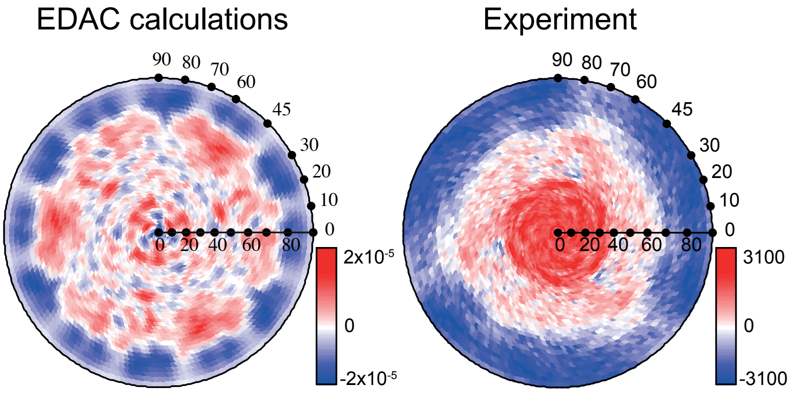

Figure 6.6 Difference patterns for the "*cis-trans*" isomerization. Left panel: EDAC simulation, right panel: difference of the two experimental patterns after three-fold average and normalization to the integral yield before background subtraction. The angular scales are indicated and the color code is defined such that blue color represents a loss of spectral weight and red color an increase of spectral weight upon excitation by UV light.

carried out because these effects affect both measurements in the same way and, therefore, cancel out in the difference pattern. Moreover, irrespective of the number of molecules which switched during the experiment the difference pattern is always the same qualitatively if the total number of molecules is constant. The difference pattern is displayed in Fig. 6.6 and compared to the corresponding difference pattern obtained from the EDAC simulations.

Both, the experimental and the simulated patterns show a clear shift of spectral weight from high to low polar angles. This can easily be understood by comparing the results with the structures of the isomers shown in Fig. 6.3. As described above, at kinetic energies of about 850 eV the electrons are predominantly scattered in forward direction. Hence, emission is enhanced at high polar angles for the *trans* isomer, and for lower polar angles in the *cis* isomer.

Moreover, some propeller-like lobes can be observed in the experimental difference pattern which might correspond to three positive maxima found in the simulation at polar angles between 65° and 80° in Fig. 6.6. The structure in the experimental pattern appears to be broadened. Since in the *cis* isomer both phenyl moieties are lifted from the surface and since interactions between neighboring molecules are expected to be negligible, the phenyls may rotate around the nitrogen-carbon bonds, thus reducing strongly the rigidity of the molecules. As a consequence, any azimuthal structure which leads to rather sharp features for emission from *trans* isomers, is expected to be smeared out in the case of the *cis* isomer, in agreement with our findings.

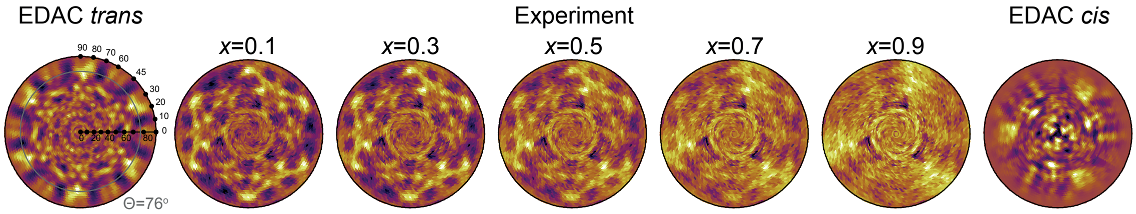

Figure 6.7 Comparison of calculated and experimental patterns for various values of x. From left to right: EDAC calculation for *trans*, experimental patterns $I_{\mathrm{PSS}}(\theta,\phi) - x \cdot I_{trans}(\theta,\phi)$ for $x = 0.1$ through $x = 0.9$ and EDAC calculation for *cis*. The circle in the EDAC *trans* calculation indicates a polar emission angle of $\theta = 76°$.

Quantitative analysis

A quantitative assessment is more complex. The main reason is that the calculation of the switching probability relies on the scattering calculations. In principle one might compare the modulation amplitude in the difference pattern shown in Fig. 6.6 to the intensity of the pure *trans* signal, for instance. The EDAC calculations then provide the reference, *i.e.* the relative change in the pattern expected for the isomerization of 100% of the molecules on the surface. This procedure is prone to errors due to the instrumental normalization required to account for polar variations of the geometrical light incidence and analyzer focus and the inelastic attenuation length, as already outlined in Section 6.3. In particular, any normalization procedure affects the distribution in polar angle. The latter is the most significant part of the difference patterns as can be easily seen in Fig. 6.6.

We have therefore chosen another approach to access the isomerization ratio quantitatively. We use [*cis*] and [*trans*] to denote the relative occurrences of *cis* and *trans* isomers on the surface with the normalization [*cis*]+[*trans*]=1. We may then write the resulting photoelectron distribution in any state as follows:

$$I(\theta,\phi) = [cis] \cdot I_{cis}(\theta,\phi) + [trans] \cdot I_{trans}(\theta,\phi), \tag{6.1}$$

where θ and ϕ denote the polar angle with respect to the surface normal and the azimuthal angle around the surface normal with respect to the crystalline $[\bar{1}\,\bar{1}\,2]$ direction, respectively (see Figs. 6.3 and 6.5). We assume that the sample without UV illumination is close to pure *trans* state ([*trans*]=1 and [*cis*]=0), denoted hereafter as I_{trans}, while the photostationary state can be written as mixed state I_{PSS}. Since the concentrations [*cis*] and [*trans*] in I_{PSS} are still unknown, we test our assumption made in Eqn. (6.1) and subtract the experimental *trans* pattern multiplied with a

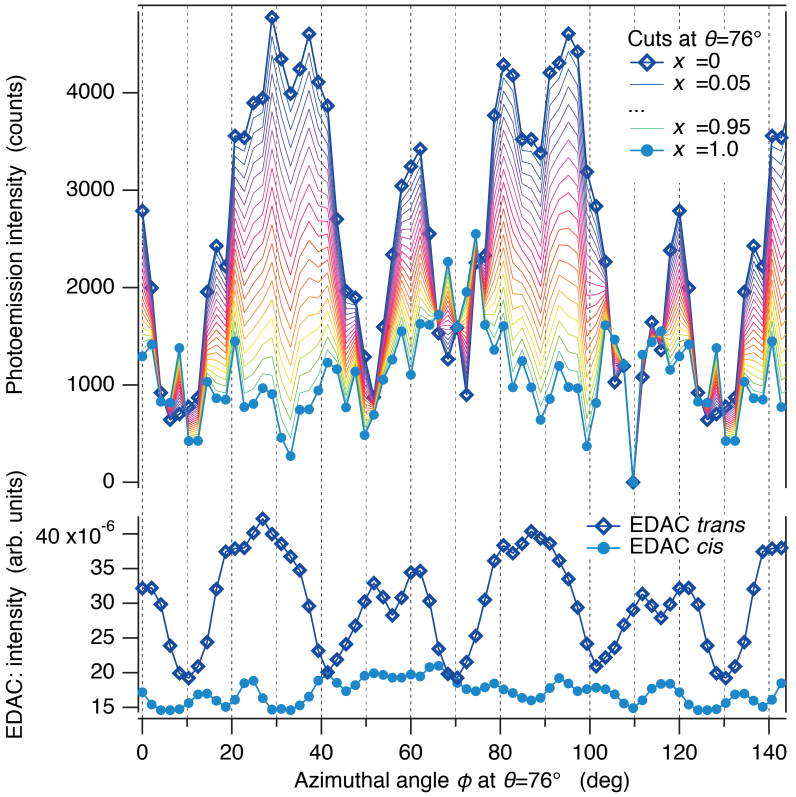

Figure 6.8 Azimuthal cuts at $\theta = 76°$ along the circle shown in Fig. 6.7. Top panel: experimental traces from $x = 0$ (topmost trace, blue open symbols) to $x = 1.0$ (bottommost trace, solid turquoise symbols) in steps of $\Delta x = 0.05$ (see text for details). Bottom panel: azimuthal cuts through the simulated EDAC *trans* (blue open symbols) and *cis* (solid turquoise symbols) patterns at the same angular position.

factor x ranging from 0 to 1 from the experimental pattern in the PSS:

$$\Delta I(x, \theta, \phi) = \; I_{\mathrm{PSS}}(\theta, \phi) - x \cdot I_{trans}(\theta, \phi). \tag{6.2}$$

If we compare Eqns. (6.2) and (6.1) we see that at $x = [trans]$ the resulting pattern $\Delta I(x, \theta, \phi)$ must be a pure *cis* pattern. This procedure is visualized in Fig. 6.7: starting at $x = 0.1$ with a pattern close to the calculated *trans* pattern and increasing x we continuously approach a pattern which is close to the EDAC simulation of the *cis* state. Note that as already mentioned above the features are smeared out due to increased flexibility of the molecules around the nitrogen-carbon bonds.

The most clear signature of the transition from *trans* to *cis* is found at high polar angles. Therefore, we use these features as fingerprints and assume their intensity to be proportional to the density of the corresponding isomers. In addition, it is advantageous to compare traces at fixed polar angle: The intensity variation with polar angle is due to geometrical changes of the focii of light source and electron analyzer, and changes of electron escape depth, and optical matrix elements. The variation and the required normalization is *a priori* unknown. If only azimuthal rotations at constant polar angle are considered, these variations can by neglected. At $\theta \approx 76°$ we observe six sharp spots due to the well-defined nitrogen-carbon bonds in the *trans* state. They gradually disappear with increasing x. At $x \approx 0.9$ three large lobes are observed and some weaker features reminiscent of the *cis* pattern. If we extract the intensity as function of azimuthal angle at $\theta = 76°$ for all these distributions we obtain the traces displayed in Fig. 6.8, which are compared to corresponding curves obtained from the calculations. One clearly observes the transition from the *trans* to the *cis* pattern by following the disappearance of the strong maxima at $\phi = 30°$ and 90°.

For a more objective analysis, a statistical evaluation is required. In contrast to earlier studies (e.g. Refs. [73, 139]), in which a modified χ^2 function was used [140] , we used the Pearson correlation coefficient r to compare each of the azimuthal distributions shown in Fig. 6.8 with the corresponding curves from the *trans* and *cis* calculations. The Pearson r-factor is defined as the covariance of two functions normalized by the square roots of the variances of each of them[141]. It does not require any treatment like scaling of the data prior to the calculation of the correlation function. In case of maximum (anti-) correlation, r must approach the value of (-)1, a value of 0 corresponds to no correlation. We evaluated the following expression for *cis* and the analogous one for *trans*, and for the two most suitable angles $\theta = 76°$ and 78°:

$$\begin{aligned} r_{cis}(x) = &\quad \frac{\sum_i (\Delta I(x,\theta,\phi_i)-\langle \Delta I\rangle)\cdot(I_{cis}(\theta,\phi_i)-\langle I_{cis}\rangle)}{s_{\Delta I}\cdot s_{I_{cis}}} \\ \text{with} \quad s_{\Delta I} = &\ \sqrt{\textstyle\sum_j (\Delta I(x,\theta,\phi_j) - \langle \Delta I\rangle)^2} \\ \text{and} \quad s_{I_{cis}} = &\ \sqrt{\textstyle\sum_k (I_{cis}(\theta,\phi_k) - \langle \Delta I\rangle)^2}, \end{aligned} \tag{6.3}$$

where $\langle \Delta I\rangle$ and $\langle I_{cis}\rangle$ denote the average values of ΔI and I_{cis} for all angles ϕ, respectively.

The results are shown in Fig. 6.9. As expected for $x \approx 0$ the r factor is higher for the *trans* state than for *cis*. When x increases the correlation with *trans* becomes weaker, while the r-factor reflecting the covariance with the *cis* trace increases. The r-factor of the *cis* goes through a maximum for both angles. The weighted mean value at which r is maximum is $x_{\mathrm{m}} = 0.92 \pm 0.025$. This means that $8.0\% \pm 2.5\%$ of the molecules underwent isomerization into the *cis* state in our case.

In order to compare to published switching probabilities, we have to take the tem-

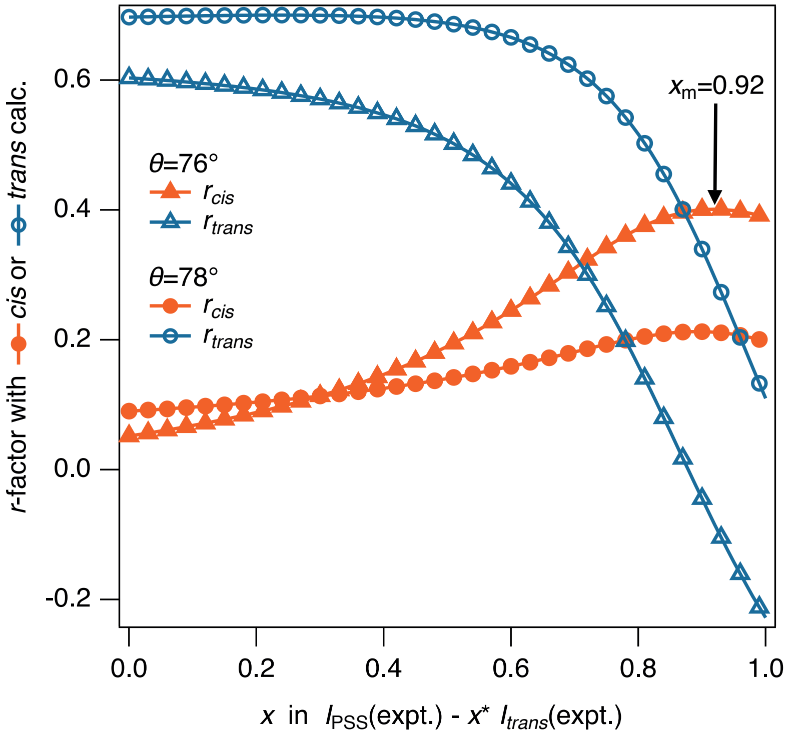

Figure 6.9 Pearson correlation coefficient [141] r comparing the experimental cuts of Fig. 6.8 ($\theta = 76°$, triangles) and for $\theta = 78°$ (circles) with the cuts through the calculated patterns for *cis* (solid orange symbols) and *trans* (open blue symbols) states.

perature and different photon energies into account. It must be emphasized that the isomerization process and the cross-sections change considerably when going from molecules in solution to molecules adsorbed on surfaces [18]. Based on temperature- and photon-energy dependent 2PPE experiments, Hagen and co-workers proposed the following picture for the isomerization of TBA on Au(111) [18, 126, 134]: Electrons are excited by photons out of the substrate Au 5d manifold and the photohole is transferred to the HOMO of the TBA molecule. The minimum energy required for creating photoholes in the 5d levels is about 2.2 eV, which is in agreement with the observed threshold behaviour at 2 eV of the isomerization cross-section and the almost constant value for photon energies between 2.2 and 4.4 eV [126]. For higher photon energies the effective cross-section strongly increases again due to increased photoionization probability of Au 5d.

The transient positive ion resonance due to hole transfer into the HOMO allows for efficient energy transfer to the molecule and, thereby, triggers the isomerization. The isomerization may proceed in both ways, from *trans* to *cis* and from *cis* to *trans*. The branching ratio, *i.e.* the relative probabilities for the two directions are fairly constant in energy [18] and roughly 1:1 slightly in favor of the *trans* to *cis* transition [18, 133]. While in solution the potential energy surface of TBA has two minima of comparable depth for the two isomers, the minimum of the *cis* isomer of TBA becomes shallow upon adsorption on a metal substrate. This favors thermally activated isomerization and leads to a net thermal isomerization rate from *cis* to *trans*. Thus, the relative fraction of *cis* and *trans* molecules is given by the ratio of the cross-sections for photo-induced switching and the thermal rate. The photostationary state comes closer to the pure *trans* state at higher temperature. The typical time scale for reaching the PSS is given by the effective isomerization cross-section and the photon flux.

While the VUV photon flux of the He discharge lamp used here is known from photocurrent measurements [130, 131], the flux of visible and near-UV photons had to be determined in a separate experiment using a discharge source working at the same discharge pressure. We obtain a flux of about 1.1×10^{14} ph/(cm^2 s) for photon energies higher than 2.2 eV, about the same order of magnitude as the one of VUV photons of 1.8×10^{14} ph/(cm^2 s). Using these numbers and our experimental results, and assuming the known branching ratio[18] for *cis* and *trans* isomerization, we achieve good agreement with observed values using an effective cross-section of the order of $\sigma_{\text{eff}} \approx 10^{-17}$ cm^2. The time required to drive the system into the photostationary state, defined as 90% of the final *cis* concentration, is estimated to be about one hour, based on the results for the photon flux and cross-sections and in agreement with own experimental findings. The effective total isomerization cross-section σ_{eff} derived here is higher by several orders of magnitude than cross-sections of 10^{-23} cm^2 at a photon energy of about 3 eV and 30 K [133] or 10^{-22} cm^2 for visible light and a temperature of 90 K [134]. This can be explained by the higher photoionization cross-section of the Au 5d states[142] and the possible direct photo-ionization of the TBA molecule.

Outlook: Time-resolved photoelectron diffraction experiments

A standard photoelectron diffraction data set represents the angular distribution of photoemission intensity recorded at fixed electron kinetic energy for a chosen number of emission directions. When investigating sensitive surface systems like layers of organic molecules data acquisition should be fast to avoid sample damage. Furthermore, the number of emission angles recorded will depend on the goal of experiment, because a full and accurate structure determination requires a fine grid in polar and azimuthal angle. According to experience, such a grid covering the full hemisphere above the sample has 4'000-5'000 angles, spaced such that each pixel represents the same solid angle. Using parallel data acquisition as it is possible with most modern electron detectors the number of sample settings can be greatly reduced [143].

The strategy will be different if the structural dynamics are studied. Time-resolved experiments are usually carried out in pump-probe mode. After an excitation pulse (pump), the transient structure can be tracked by photoelectrons excited by a second time-delayed (x-ray) probe pulse. Thus, the time delay represents an additional parameter, which has to be varied, multiplying the number of measurements with the number of time delays. The latter is typically of the order of 100 steps. Our present results demonstrate the sensitivity of XPD to structural changes in a small number of molecules on top of a high background of molecules in the ground state. Such a measurement could correspond to one such time delay setting in a time-resolved pump-probe experiment. Realistically, however, the number of emission directions (pixels) is limited to the number of angular channels which can be recorded in parallel in a single measurement. Longer integration times and, thereby, better data statistics often outweigh the number of pixels in such experiments [140].

Quantitative assessment then requires the use of fingerprints representing all possible transient structures. Such fingerprints can be either numerical simulations as in our case here or the existence of reference data from these transient structures. Reference date must be taken from pure samples. This is impossible in the present case but such data can be measured in static measurements from all phases of a system undergoing a phase transition as a function of sample temperature, for instance. In order to compare the data, it turned out to be advantageous to analyze difference data. In this way, problems with data normalization due to a change in geometry upon sample rotation are minimized and subtraction of a background is not necessary because it cancels in the difference data to a good approximation. Moreover, in the present case the normalization was avoided by solely comparing traces as function of the azimuthal angle at constant polar angle. Since the azimuthal rotation corresponds to a rotation around the surface normal, the experimental geometry does not change and any intensity modulations can be attributed to effects due to the electronic or atomic structure of the surface under investigation [138].

The features of the patterns which can clearly be attributed to one of the structures can be used as fingerprints. In this case, a full structure determination at each delay is not required, what reduces considerably the measurement time. The intensity of the features is a simple measure of the number of molecules in the corresponding transient state. Statistical analysis can be used in order to assess the ratios of the isomers in a quantitative way. For each delay time step, the best match is found by evaluating reliability factors as shown in the present work.

Conclusion

In conclusion we presented photoelectron diffraction data from tetra-tert-butyl-azobenzene molecules adsorbed on Au(111). Upon excitation with visible, ultraviolet, and vacuum-ultraviolet radiation, the molecules undergo reversible *trans*-to-*cis* isomerization, which can be detected in the diffraction patterns. Moreover, a quantitative analysis revealed that the isomerization can be driven very efficiently with high-energy vacuum-ultraviolet photons. This gives further evidence for an isomerization mechanism, which proceeds by generation of photoholes in the Au 5d shell and hole transfer into the HOMO, where a transient positive ion is formed. The excess energy is then used to drive the isomerization of the molecule.

The fact that a small number of switched molecules can be observed in photoelectron diffraction experiments on top of a large background of passive molecules opens new possibilities for studying structural dynamics in solid surfaces with potentially femtosecond time resolution.

Acknowledgments

We thank Prof. Dr. Stefan Bienz (Department of Chemistry, University of Zurich) for providing the TBA molecules and Prof. Dr. Thomas Greber for valuable discussions. We acknowledge financial support from the Swiss National Science Foundation through NCCR MUST.

7 Outlook

In this thesis it was successfully demonstrated that the new HHG light source and the photoemission endstation TREx are well suited for trARPES of solids. The 100 fs time resolution and the photon energy of 15 eV allows one to study electron dynamics even at the SBZ boundaries. This is important for the investigation of many different physical systems which require pump-probe and XUV photon energies. Such systems like, e.g. graphene or MoS_2 are possible candidates to be measured with high harmonic light. Furthermore, time-resolved UV photoelectron diffraction and time-resolved molecular tomography studies can be carried out with a pulsed XUV light source.

It is planned to expand the high harmonic light source in the future by the optical parametric amplifier (OPA). The OPA is a tunable light source with an energy range from 1.77 eV to 2.65 eV. With the option of a tunable pump laser, the $\pi - \pi^*$ transition in h-BN/Ni(111) could be realized to investigate the nature of the energy gap in a monolayer h-BN on Ni(111). Furthermore, in view of electron excitation from the highest occupied molecular orbital (HOMO) to the lowest unoccupied molecular orbital (LUMO), the tunability of the photon energies would be an improvement in order to locate the HOMO-LUMO energy gap.

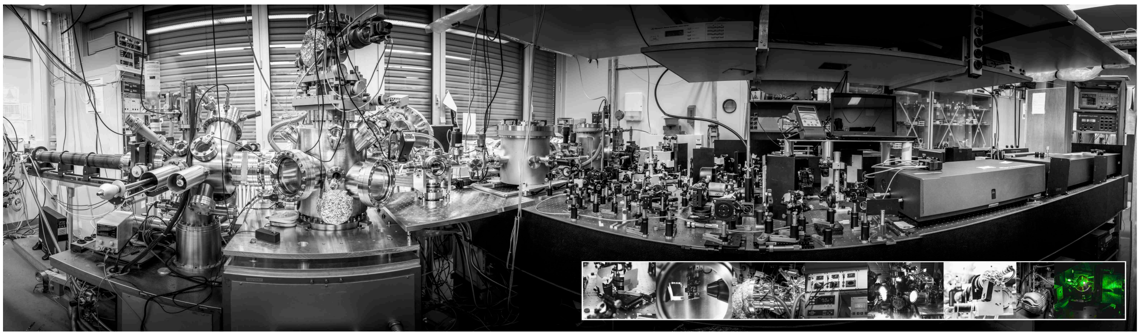

Figure 7.1 Photography of TREx and the high harmonic light source.

Bibliography

[1] A. Einstein, *Zur Quantentheorie der Strahlung*, Physikalische Zeitschrift **18**, 121–128 (1917).

[2] J. P. Gordon, H. J. Zeiger, and C. H. Townes, *The Maser—New Type of Microwave Amplifier, Frequency Standard, and Spectrometer*, Physical Review **99**, 1264–1274 (1955).

[3] A. L. Schawlow and C. H. Townes, *Infrared and Optical Masers*, Physical Review **112**, 1940–1949 (1958).

[4] T. H. Maiman, *Stimulated optical radiation in Ruby*, Nature **187**, 493–494 (1960).

[5] R. Jiang, D. Mou, Y. Wu, L. Huang, C. D. McMillen, J. Kolis, H. G. Giesber, J. J. Egan, and A. Kaminski, *Tunable vacuum ultraviolet laser based spectrometer for angle resolved photoemission spectroscopy*, Review of Scientific Instruments **85**, 033902 (2014).

[6] M. Ferray, A. L'Huillier, X. F. Li, L. A. Lompre, G. Mainfray, and C. Manus, *Multiple-harmonic conversion of 1064 nm radiation in rare gases*, Journal of Physics B: Atomic, Molecular and Optical Physics **21**, 31–35 (1988).

[7] A. McPherson, G. Gibson, H. Jara, U. Johann, T. S. Luk, I. A. McIntyre, K. Boyer, and C. K. Rhodes, *Studies of multiphoton production of vacuum-ultraviolet radiation in the rare gases*, Journal of the Optical Society of America B **4**, 595–601 (1987).

[8] S. Mathias, L. Miaja-Avila, M. M. Murnane, H. Kapteyn, M. Aeschlimann, and M. Bauer, *Angle-resolved photoemission spectroscopy with a femtosecond high harmonic light source using a two-dimensional imaging electron analyzer*, Review of Scientific Instruments **78**, 083105 (2007).

[9] P. Siffalovic, M. Drescher, M. Spieweck, T. Wiesenthal, Y. C. Lim, R. Weidner, A. Elizarov, and U. Heinzmann, *Laser-based apparatus for extended ultraviolet femtosecond time-resolved photoemission spectroscopy*, Review of Scientific Instruments **72**, 30–35 (2001).

[10] R. Locher, L. Castiglioni, M. Lucchini, M. Greif, L. Gallmann, J. Osterwalder, M. Hengsberger, and U. Keller, *Energy-dependent photoemission delays from noble metal surfaces by attosecond interferometry*, Optica **2**, 405–410 (2015).

[11] M. Nakasuji, A. Tokimasa, T. Harada, Y. Nagata, T. Watanabe, K. Midorikawa, and H. Kinoshita, *Development of coherent extreme-ultraviolet scatterometry microscope with high-order harmonic generation source for extreme-ultraviolet mask inspection and metrology*, Japanese Journal of Applied Physics **51**, 06FB09 (2012).

[12] S. Passlack, S. Mathias, O. Andreyev, D. Mittnacht, M. Aeschlimann, and M. Bauer, *Space charge effects in photoemission with a low repetition, high intensity femtosecond laser source*, Journal of Applied Physics **100**, 024912 (2006).

[13] J. Sobota, S.-L. Yang, D. Leuenberger, A. Kemper, J. Analytis, I. Fisher, P. Kirchmann, T. Devereaux, and Z.-X. Shen, *Ultrafast electron dynamics in the topological insulator Bi2Se3 studied by time-resolved photoemission spectroscopy*, Journal of Electron Spectroscopy and Related Phenomena **195**, 249–257 (2014).

[14] P. Hein, A. Stange, K. Hanff, L. X. Yang, G. Rohde, K. Rossnagel, and M. Bauer, *Momentum-resolved hot electron dynamics at the 2H MoS2 surface*, Physical Review B **94**, 205406 (2016).

[15] R. Wallauer, J. Reimann, N. Armbrust, J. Güdde, and U. Höfer, *Intervalley scattering in MoS 2 imaged by two-photon photoemission with a high-harmonic probe*, Applied Physics Letters **109**, 162102 (2016).

[16] G. B. Grad, P. Blaha, K. Schwarz, W. Auwärter, and T. Greber, *Density functional theory investigation of the geometric and spintronic structure of h - BN/Ni(111) in view of photoemission and STM experiments*, Physical Review B **68**, 085404 (2003).

[17] M. J. Comstock, N. Levy, A. Kirakosian, J. Cho, F. Lauterwasser, J. H. Harvey, D. A. Strubbe, J. M. J. Fréchet, D. Trauner, S. G. Louie, and M. F. Crommie, *Reversible Photomechanical Switching of Individual Engineered Molecules at a Metallic Surface*, Physical Review Letters **99**, 038301 (2007).

[18] M. Wolf and P. Tegeder, *Reversible molecular switching at a metal surface: A case study of tetra-tert-butyl-azobenzene on Au(111)*, Surface Science **603**, 1506–1517 (2009).

[19] H. Hertz, *Ueber einen Einfluss des ultravioletten Lichtes auf die electrische Entladung*, Annalen der Physik und Chemie **267**, 983–1000 (1887).

[20] A. Einstein, *Über einen die Erzeugung und Verwandlung des Lichtes betreffenden heuristischen Gesichtspunkt*, Annalen der Physik **322**, 132–148 (1905).

[21] S. Hüfner, *Photoelectron spectroscopy Principles and applications* (1995).

[22] J. Osterwalder, *Edited by K. Wandelt*, Surface and Interface Science Vol.1 , Wiley–VCH (2012).

[23] A. Damascelli, *Probing the Electronic Structure of Complex Systems by ARPES*, Physica Scripta **T109**, 61–74 (2004).

[24] M. Muntwiler, M. Hengsberger, A. Dolocan, H. Neff, T. Greber, and J. Osterwalder, *Energetics and dynamics of unoccupied electronic states at the h-BN/Ni(111) interface*, Physical Review B **75**, 075407 (2007).

[25] D. Leuenberger, H. Yanagisawa, S. Roth, J. Osterwalder, and M. Hengsberger, *Disentanglement of electron dynamics and space-charge effects in time-resolved photoemission from h-BN/Ni(111)*, Physical Review B **84**, 125107 (2011).

[26] U. Bovensiepen, H. Petek, and M. Wolf, *Dynamics at Solid State Surfaces and Interfaces* (2012).

[27] F. Buchner, *Time-resolved photoelectron spectroscopy of DNA molecules in solution*, PhD Thesis , Freie Universität Berlin (2015).

[28] P. B. Corkum, *Plasma perspective on strong field multiphoton ionization*, Physical Review Letters **71**, 1994–1997 (1993).

[29] J. Metje, *Development and Application of a XUV Laser Light Source for Photoelectron Spectroscopy of Solutions*, PhD Thesis , Freie Universität Berlin (2016).

[30] M. Lewenstein, P. Balcou, M. Y. Ivanov, A. L'Huillier, and P. B. Corkum, *Theory of high-harmonic generation by low-frequency laser fields*, Physical Review A **49**, 2117–2132 (1994).

[31] V. S. Popov, *Tunnel and multiphoton ionization of atoms and ions in a strong laser field (Keldysh theory)*, Physics-Uspekhi **47**, 855–885 (2004).

[32] NIST Database, *Ionization potential.*

[33] C. M. Heyl, *High-Order Harmonic Generation at 100 kHz Repetition Rate for Time-Resolved Two-Photon Photoemission*, Diploma Thesis , Philipps Universität Marburg (2010).

[34] T. F. Gallagher, *Above-Threshold Ionization in Low-Frequency Limit*, Physical Review Letters **61**, 2304–2307 (1988).

[35] A. L'Huillier, M. Lewenstein, P. Salières, P. Balcou, M. Y. Ivanov, J. Larsson, and C. G. Wahlström, *High-order Harmonic-generation cutoff*, Physical Review A **48**, R3433–R3436 (1993).

[36] V.-M. Gkortsas, S. Bhardwaj, C.-J. Lai, K.-H. Hong, E. L. Falcão-Filho, and F. X. Kärtner, *Interplay of mulitphoton and tunneling ionization in short-wavelength-driven high-order harmonic generation*, Physical Review A **84**, 013427 (2011).

[37] G. G. Paulus, W. Becker, and H. Walther, *Classical rescattering effects in two-color above-threshold ionization*, Physical Review A **52**, 4043–4053 (1995).

[38] C. H. García, *Coherent attosecond light sources based on high-order harmonic generation: influence of the propagation effects*, PhD Thesis , Universidad de Salamanca (2013).

[39] C. M. Heyl, J. Güdde, A. L'Huillier, and U. Höfer, *High-order harmonic generation with μJ laser pulses at high repetition rates*, Journal of Physics B: Atomic, Molecular and Optical Physics **45**, 074020 (2012).

[40] X. He, M. Miranda, J. Schwenke, O. Guilbaud, T. Ruchon, C. Heyl, E. Georgadiou, R. Rakowski, A. Persson, M. B. Gaarde, and A. L'Huillier, *Spatial and spectral properties of the high-order harmonic emission in argon for seeding applications*, Physical Review A **79**, 063829 (2009).

[41] M. Lewenstein, P. Salières, and A. L'Huillier, *Phase of the atomic polarization in high-order harmonic generation*, Physical Review A **52**, 4747–4754 (1995).

[42] K. Varjú, Y. Mairesse, B. Carré, M. B. Gaarde, P. Johnsson, S. Kazamias, R. López-Martens, J. Mauritsson, K. J. Schafer, P. Balcou, A. L'huillier, and P. Salières, *Frequency chirp of harmonic and attosecond pulses*, Journal of Modern Optics **52**, 379–394 (2005).

[43] C. Heyl, *Scaling and Gating Attosecond Pulse Generation*, PhD Thesis (2014).

[44] P. Rudawski, C. M. Heyl, F. Brizuela, J. Schwenke, A. Persson, E. Mansten, R. Rakowski, L. Rading, F. Campi, B. Kim, P. Johnsson, and A. L'Huillier, *A high-flux high-order harmonic source*, Review of Scientific Instruments **84**, 073103 (2013).

[45] S. Eich, A. Stange, A. Carr, J. Urbancic, T. Popmintchev, M. Wiesenmayer, K. Jansen, A. Ruffing, S. Jakobs, T. Rohwer, S. Hellmann, C. Chen, P. Matyba, L. Kipp, K. Rossnagel, M. Bauer, M. Murnane, H. Kapteyn, S. Mathias, and M. Aeschlimann, *Time- and angle-resolved photoemission spectroscopy with optimized high-harmonic pulses using frequency-doubled Ti:Sapphire lasers*, Journal of Electron Spectroscopy and Related Phenomena **195**, 231–236 (2014).

[46] J. Rothhardt, M. Krebs, S. Hädrich, S. Demmler, J. Limpert, and A. Tünnermann, *Absorption-limited and phase-matched high harmonic generation in the tight focusing regime*, New Journal of Physics **16**, 033022 (2014).

[47] C.-T. Chiang, A. Blättermann, M. Huth, J. Kirschner, and W. Widdra, *High-order harmonic generation at 4 MHz as a light source for time-of-flight photoemission spectroscopy*, Applied Physics Letters **101**, 071116 (2012).

[48] M. Wieland, R. Frueke, T. Wilhein, C. Spielmann, M. Pohl, and U. Kleineberg, *Submicron extreme ultraviolet imaging using high-harmonic radiation*, Applied Physics Letters **81**, 2520–2522 (2002).

[49] L. Poletto and G. Tondello, *Time-compensated extreme-UV and soft x-ray monochromator for ultrashort high-order harmonic pulses*, Journal of Optics A: Pure and Applied Optics **3**, 374–379 (2001).

[50] E. J. Takahashi, M. Hatayama, S. Ichimaru, and K. Midorikawa, *Dispersion-free monochromator for selecting a single high-order harmonic beam*, in *CLEO: 2014* (OSA, Washington, D.C., 2014) p. FTu3B.6.

[51] F. Frassetto, C. Cacho, C. A. Froud, I. E. Turcu, P. Villoresi, W. A. Bryan, E. Springate, and L. Poletto, *Single-grating monochromator for extreme-ultraviolet ultrashort pulses*, Optics Express **19**, 19169–19181 (2011).

[52] P. Villoresi, *Compensation of optical path lengths in extreme-ultraviolet and soft-x-ray monochromators for ultrafast pulses*, Applied Optics **38**, 6040–6049 (1999).

[53] H. Wang, Y. Xu, S. Ulonska, J. S. Robinson, P. Ranitovic, and R. A. Kaindl, *Bright high-repetition-rate source of narrowband extreme-ultraviolet harmonics beyond 22 eV*, Nature Communications **6**, 7459 (2015).

[54] Henke Tables, *Transmission of metal foils.*

[55] OptiXfab, *XUV mirror producer.*

[56] B. Feuerbacher and B. Fitton, *Experimental investigation of photoemission from satellite surface materials*, Journal of Applied Physics **43**, 1563–1572 (1972).

[57] M.-C. Chen, M. R. Gerrity, S. Backus, T. Popmintchev, X. Zhou, P. Arpin, X. Zhang, H. C. Kapteyn, and M. M. Murnane, *Spatially coherent, phase matched, high-order harmonic EUV beams at 50 kHz*, Optics Express **17**, 17376 (2009).

[58] W.-Z. Lin, R. Schoenlein, J. Fujimoto, and E. Ippen, *Femtosecond absorption saturation studies of hot carriers in GaAs and AlGaAs*, IEEE Journal of Quantum Electronics **24**, 267–275 (1988).

[59] J. H. Dil, F. Meier, and J. Osterwalder, *Rashba-type spin splitting and spin interference of the Cu(111) surface state at room temperature*, Journal of Electron Spectroscopy and Related Phenomena **201**, 42–46 (2015).

[60] S. D. Kevan, *Evidence for a New Broadening Mechanism in Angle-Resolved Photoemission from Cu(111)*, Physical Review Letters **50**, 526–529 (1983).

[61] T. Hertel, E. Knoesel, M. Wolf, and G. Ertl, *Ultrafast Electron Dynamics at Cu(111): Response of an Electron Gas to Optical Excitation*, Physical Review Letters **76**, 535–538 (1996).

[62] J. A. Sobota, S. Yang, J. G. Analytis, Y. L. Chen, I. R. Fisher, P. S. Kirchmann, and Z.-X. Shen, *Ultrafast Optical Excitation of a Persistent Surface-State Population in the Topological Insulator* Bi_2Se_3, Physical Review Letters **108**, 117403 (2012).

[63] Y. Wang, J. Han, Y. Li, and H. Chen, *Progress in preparation, properties and application of boron nitride nanomaterials*, in *AIP Conference Proceedings*, Vol. 1864 (2017) p. 020132.

[64] A. A. Tonkikh, E. N. Voloshina, P. Werner, H. Blumtritt, B. Senkovskiy, G. Güntherodt, S. S. P. Parkin, and Y. S. Dedkov, *Structural and electronic properties of epitaxial multilayer h-BN on Ni(111) for spintronics applications*, Scientific Reports **6**, 23547 (2016).

[65] A. Nagashima, N. Tejima, Y. Gamou, T. Kawai, and C. Oshima, *Electronic Structure of Monolayer Hexagonal Boron Nitride Physisorbed on Metal Surfaces*, Physical Review Letters **75**, 3918–3921 (1995).

[66] A. Goriachko, He, M. Knapp, H. Over, M. Corso, T. Brugger, S. Berner, J. Osterwalder, and T. Greber, *Self-Assembly of a Hexagonal Boron Nitride Nanomesh on Ru(0001)*, Langmuir **23**, 2928–2931 (2007).

[67] W. Auwärter, T. Kreutz, T. Greber, and J. Osterwalder, *XPD and STM investigation of hexagonal boron nitride on Ni(111)*, Surface Science **429**, 229–236 (1999).

[68] M. Corso, *Boron Nitride Nanomesh*, Science **303**, 217–220 (2004).

[69] C. R. Dean, A. F. Young, I. Meric, C. Lee, L. Wang, S. Sorgenfrei, K. Watanabe, T. Taniguchi, P. Kim, K. L. Shepard, and J. Hone, *Boron nitride substrates for high-quality graphene electronics*, Nature Nanotechnology **5**, 722–726 (2010).

[70] S. Roth, T. Greber, and J. Osterwalder, *Some Like It Flat: Decoupled h-BN Monolayer Substrates for Aligned Graphene Growth*, ACS Nano **10**, 11187–11195 (2016).

[71] X. Blase, A. Rubio, S. G. Louie, and M. L. Cohen, *Quasiparticle band structure of bulk hexagonal boron nitride and related systems*, Physical Review B **51**, 6868–6875 (1995).

[72] K. Zumbrägel, K. Wulff, C. Eibl, M. Donath, and M. Hengsberger, *Exchange-split interface state at h-BN/Ni(111)*, Physical Review B **78**, 085422 (2008).

[73] M. Muntwiler, W. Auwärter, F. Baumberger, M. Hoesch, Thomas Greber, and J. Osterwalder, *Determining adsorbate structures from substrate emission X-ray photoelectron diffraction*, Surface Science **472**, 125–132 (2001).

[74] ElettraDatabase, *Photoionization cross-sections.*

[75] W. Auwärter, M. Muntwiler, J. Osterwalder, and T. Greber, *Defect lines and two-domain structure of hexagonal boron nitride films on Ni(111)*, Surface Science **545**, L735–L740 (2003).

[76] K. Watanabe, T. Taniguchi, and H. Kanda, *Direct-bandgap properties and evidence for ultraviolet lasing of hexagonal boron nitride single crystal*, Nature Materials **3**, 404–409 (2004).

[77] X.-L. Qi and S.-C. Zhang, *The quantum spin Hall effect and topological insulators*, Physics Today **63**, 33–38 (2010).

[78] K. V. Klitzing, G. Dorda, and M. Pepper, *New Method for High-Accuracy Determination of the Fine-Structure Constant Based on Quantized Hall Resistance*, Physical Review Letters **45**, 494–497 (1980).

[79] B. A. Bernevig, T. L. Hughes, and S.-C. Zhang, *Quantum Spin Hall Effect and Topological Phase Transition in HgTe Quantum Wells*, Science **314**, 1757–1761 (2006).

[80] C. Jozwiak, J. A. Sobota, K. Gotlieb, A. F. Kemper, C. R. Rotundu, R. J. Birgeneau, Z. Hussain, D.-H. Lee, Z.-X. Shen, and A. Lanzara, *Spin-polarized surface resonances accompanying topological surface state formation*, Nature Communications **7**, 13143 (2016).

[81] D. Hsieh, D. Qian, L. Wray, Y. Xia, Y. S. Hor, R. J. Cava, and M. Z. Hasan, *A topological Dirac insulator in a quantum spin Hall phase*, Nature **452**, 970–974 (2008).

[82] Y. Xia, D. Qian, D. Hsieh, L. Wray, A. Pal, H. Lin, A. Bansil, D. Grauer, Y. S. Hor, R. J. Cava, and M. Z. Hasan, *Observation of a large-gap topological-insulator class with a single Dirac cone on the surface*, Nature Physics **5**, 398–402 (2009).

[83] M. Z. Hasan and C. L. Kane, *Colloquium: Topological insulators*, Reviews of Modern Physics **82**, 3045–3067 (2010).

[84] R. J. Cava, H. Ji, M. K. Fuccillo, Q. D. Gibson, and Y. S. Hor, *Crystal structure and chemistry of topological insulators*, Journal of Materials Chemistry C **1**, 3176 (2013).

[85] A. S. Hewitt, J. Wang, J. Boltersdorf, P. A. Maggard, and D. B. Dougherty, *Coexisting Bi and Se surface terminations of cleaved Bi 2 Se 3 single crystals*, Journal of Vacuum Science and Technology B, Nanotechnology and Microelectronics Materials, Processing, Measurement, and Phenomena **32**, 04E103 (2014).

[86] H. Zhang, C.-X. Liu, X.-L. Qi, X. Dai, Z. Fang, and S.-C. Zhang, *Topological insulators in Bi2Se3, Bi2Te3 and Sb2Te3 with a single Dirac cone on the surface*, Nature Physics **5**, 438–442 (2009).

[87] W. Zhang, R. Yu, H.-J. Zhang, X. Dai, and Z. Fang, *First-principles studies of the three-dimensional strong topological insulators Bi2Te3, Bi2Se3 and Sb2Te3*, New Journal of Physics **12**, 065013 (2010).

[88] X.-G. Zhu, M. Stensgaard, L. Barreto, W. S. E. Silva, S. Ulstrup, M. Michiardi, M. Bianchi, M. Dendzik, and P. Hofmann, *Three Dirac points on the (110) surface of the topological insulator Bi1minusx Sbx*, New Journal of Physics **15**, 103011 (2013).

[89] J. Navrátil, J. Horák, T. Plecháček, S. Kamba, P. Lošt'ák, J. Dyck, W. Chen, and C. Uher, *Conduction band splitting and transport properties of Bi2Se3*, Journal of Solid State Chemistry **177**, 1704–1712 (2004).

[90] Y. S. Hor, A. Richardella, P. Roushan, Y. Xia, J. G. Checkelsky, A. Yazdani, M. Z. Hasan, N. P. Ong, and R. J. Cava, *p-type Bi2Se3 for topological insulator and low-temperature thermoelectric applications*, Physical Review B **79**, 195208 (2009).

[91] P. D. King, R. C. Hatch, M. Bianchi, R. Ovsyannikov, C. Lupulescu, G. Landolt, B. Slomski, J. H. Dil, D. Guan, J. L. Mi, E. D. Rienks, J. Fink, A. Lindblad, S. Svensson, S. Bao, G. Balakrishnan, B. B. Iversen, J. Osterwalder, W. Eberhardt, F. Baumberger, and P. Hofmann, *Large Tunable Rashba Spin Splitting of a Two-Dimensional Electron Gas in Bi2Se3*, Physical Review Letters **107**, 096802 (2011).

[92] B. Zhou, Z. K. Liu, J. G. Analytis, K. Igarashi, S. K. Mo, D. H. Lu, R. G. Moore, I. R. Fisher, T. Sasagawa, Z. X. Shen, Z. Hussain, and Y. L. Chen, *Controlling the carriers of topological insulators by bulk and surface doping*, Semiconductor Science and Technology **27**, 124002 (2012).

[93] C. E. ViolBarbosa, C. Shekhar, B. Yan, S. Ouardi, E. Ikenaga, G. H. Fecher, and C. Felser, *Direct observation of band bending in the topological insulator Bi2Se3*, Physical Review B **88**, 195128 (2013).

[94] M. Hajlaoui, E. Papalazarou, J. Mauchain, G. Lantz, N. Moisan, D. Boschetto, Z. Jiang, I. Miotkowski, Y. P. Chen, A. Taleb-Ibrahimi, L. Perfetti, and M. Marsi, *Ultrafast Surface Carrier Dynamics in the Topological Insulator Bi2Te3*, Nano Letters **12**, 3532–3536 (2012).

[95] M. Aeschlimann, M. Bauer, S. Pawlik, R. Knorren, G. Bouzerar, and K. Bennemann, *Transport and dynamics of optically excited electrons in metals*, Applied Physics A: Materials Science and Processing **71**, 485–491 (2000).

[96] Z. Wang, T. Lin, P. Wei, X. Liu, R. Dumas, K. Liu, and J. Shi, *Tuning carrier type and density in Bi2Se3 by Ca-doping*, Applied Physics Letters **97**, 10–13 (2010).

[97] Y.-P. Lai, H.-J. Chen, K.-H. Wu, and J.-M. Liu, *Temperature-dependent carrier–phonon coupling in topological insulator Bi2Se3*, Applied Physics Letters **105**, 232110 (2014).

[98] Y. Zou, Z.-G. Chen, Y. Huang, L. Yang, J. Drennan, and J. Zou, *Anisotropic Electrical Properties from Vapor–Solid–Solid Grown Bi2Se3 Nanoribbons and Nanowires*, The Journal of Physical Chemistry C **118**, 20620–20626 (2014).

[99] K. Ozawa, M. Emori, S. Yamamoto, R. Yukawa, S. Yamamoto, R. Hobara, K. Fujikawa, H. Sakama, and I. Matsuda, *Electron–Hole Recombination Time at TiO2 Single-Crystal Surfaces: Influence of Surface Band Bending*, The Journal of Physical Chemistry Letters **5**, 1953–1957 (2014).

[100] A. Melzer, D. Kampa, J. Wang, and T. Fauster, *Time-resolved photoemission at the Si(100)-Ga surface using a femtosecond higher-harmonic laser source*, Physical Review B - Condensed Matter and Materials Physics **80**, 205424 (2009).

[101] D. Lim and R. Haight, *In situ photovoltage measurements using femtosecond pump-probe photoelectron spectroscopy and its application to metal–HfO2–Si structures*, Journal of Vacuum Science and Technology A Vacuum, Surfaces, and Films **23**, 1698–1705 (2005).

[102] R.-Y. Liu, Y. Ogawa, P. Chen, K. Ozawa, T. Suzuki, M. Okada, T. Someya, Y. Ishida, K. Okazaki, S. Shin, T.-C. Chiang, and I. Matsuda, *Femtosecond to picosecond transient effects in WSe 2 observed by pump-probe angle-resolved photoemission spectroscopy*, Scientific Reports **7**, 15981 (2017).

[103] M. Eddrief, F. Vidal, and B. Gallas, *Optical properties of Bi 2 Se 3 : from bulk to ultrathin films*, Journal of Physics D Applied Physics **49**, 505304 (2016).

[104] N. P. Gorbachuk and V. R. Sidorko, *Heat Capacity and Enthalpy of Bi2Si3 and Bi 2Te3 in the Temperature Range 58-1012 K*, Powder Metallurgy and Metal Ceramics **43**, 284–290 (2004).

[105] Z.-H. Pan, A. V. Fedorov, D. Gardner, Y. S. Lee, S. Chu, and T. Valla, *Measurement of an Exceptionally Weak Electron-Phonon Coupling on the Surface of the Topological Insulator Bi2Se3 Using Angle-Resolved Photoemission Spectroscopy*, Physical Review Letters **108**, 187001 (2012).

[106] J. Fraxedas, J. Trodahl, S. Gopalan, L. Ley, and M. Cardona, *Temperature dependence of direct transitions in angle-resolved photoemission and its application to InSb*, Physical Review B **41**, 10068–10081 (1990).

[107] J. Fraxedas, M. K. Kelly, and M. Cardona, *Temperature-dependent angle-resolved photoemission study of the linewidth of surface states of III-V semiconductors*, Physical Review B **43**, 2159–2168 (1991).

[108] X. X. Yang, Z. F. Zhou, Y. Wang, R. Jiang, W. T. Zheng, and C. Q. Sun, *Raman spectroscopy determination of the Debye temperature and atomic cohesive energy of CdS, CdSe, Bi2Se3 , and Sb2Te3 nanostructures*, Journal of Applied Physics **112**, 083508 (2012).

[109] D. Leuenberger, H. Yanagisawa, S. Roth, J. H. Dil, J. W. Wells, P. Hofmann, J. Osterwalder, and M. Hengsberger, *Excitation of Coherent Phonons in the One-Dimensional Bi(114) Surface*, Physical Review Letters **110**, 136806 (2013).

[110] M.-M. Russew and S. Hecht, *Photoswitches: From Molecules to Materials*, Advanced Materials **22**, 3348–3360 (2010).

[111] T. Hugel, *Single-Molecule Optomechanical Cycle*, Science **296**, 1103–1106 (2002).

[112] S. Hagen, F. Leyssner, D. Nandi, M. Wolf, and P. Tegeder, *Reversible switching of tetra-tert-butyl-azobenzene on a Au(111) surface induced by light and thermal activation*, Chemical Physics Letters **444**, 85–90 (2007).

[113] M. J. Comstock, J. Cho, A. Kirakosian, and M. F. Crommie, *Manipulation of azobenzene molecules on Au(111) using scanning tunneling microscopy*, Physical Review B **72**, 153414 (2005).

[114] C. Zhang, M. H. Du, H. P. Cheng, X. G. Zhang, A. E. Roitberg, and J. L. Krause, *Coherent electron transport through an azobenzene molecule: A light-driven molecular switch*, Physical Review Letters **92**, 158301 (2004).

[115] G. S. Hartley, *The Cis-form of Azobenzene*, Nature **140**, 281–281 (1937).

[116] G. Zimmerman, L.-Y. Chow, and U.-J. Paik, *The Photochemical Isomerization of Azobenzene*, Journal of the American Chemical Society **80**, 3528–3531 (1958).

[117] P. Hamm, S. M. Ohline, and W. Zinth, *Vibrational cooling after ultrafast photoisomerization of azobenzene measured by femtosecond infrared spectroscopy*, The Journal of Chemical Physics **106**, 519–529 (1997).

[118] R. Schmidt, S. Hagen, D. Brete, R. Carley, C. Gahl, J. Dokić, P. Saalfrank, S. Hecht, P. Tegeder, and M. Weinelt, *On the electronic and geometrical structure of the trans- and cis-isomer of tetra-tert-butyl-azobenzene on Au(111)*, Physical Chemistry Chemical Physics **12**, 4488 (2010).

[119] E. R. McNellis, C. Bronner, J. Meyer, M. Weinelt, P. Tegeder, and K. Reuter, *Azobenzene versus 3,3,5,5-tetra-tert-butyl-azobenzene (TBA) at Au(111): characterizing the role of spacer groups*, Physical Chemistry Chemical Physics **12**, 6404 (2010).

[120] R. S. Saiki, G. S. Herman, M. Yamada, J. Osterwalder, and C. S. Fadley, *Structure of an unusual tilted state of CO on Fe(001) from x-ray photoelectron diffraction*, Physical Review Letters **63**, 283–286 (1989).

[121] M. Greif, L. Castiglioni, A. P. Seitsonen, S. Roth, J. Osterwalder, and M. Hengsberger, *Photoelectron diffraction in the x-ray and ultraviolet regime: Sn-phthalocyanine on Ag(111)*, Physical Review B **87**, 085429 (2013).

[122] M. Greif, T. Nagy, M. Soloviov, L. Castiglioni, M. Hengsberger, M. Meuwly, and J. Osterwalder, *Following the molecular motion of near-resonant excited CO on Pt(111): A simulated x-ray photoelectron diffraction study based on molecular dynamics calculations*, Structural Dynamics **2**, 035102 (2015).

[123] M. Greif, L. Kasmi, L. Castiglioni, M. Lucchini, L. Gallmann, U. Keller, J. Osterwalder, and M. Hengsberger, *Access to phases of coherent phonon excitations by femtosecond ultraviolet photoelectron diffraction*, Physical Review B **94**, 054309 (2016).

[124] D. Naumović, A. Stuck, T. Greber, J. Osterwalder, and L. Schlapbach, *Full-hemispherical photoelectron-diffraction data from Cu(001): Energy dependence and comparison with single-scattering-cluster simulations*, Physical Review B **47**, 7462–7479 (1993).

[125] H. Rau, *Azo Compounds*, in *Photochromism* (Elsevier, 2003) pp. 165–192.

[126] S. Hagen, P. Kate, F. Leyssner, D. Nandi, M. Wolf, and P. Tegeder, *Excitation mechanism in the photoisomerization of a surface-bound azobenzene derivative: Role of the metallic substrate*, The Journal of Chemical Physics **129**, 164102 (2008).

[127] M. Alemani, M. V. Peters, S. Hecht, K.-H. Rieder, F. Moresco, and L. Grill, *Electric Field-Induced Isomerization of Azobenzene by STM*, Journal of the American Chemical Society **128**, 14446–14447 (2006).

[128] S. Hagen, *Isomerization behaviour of photochromatic molecules in direct contact with noble metal surfaces*, PhD Thesis , Freie Universität Berlin (2009).

[129] A. Hemmi, H. Cun, S. Roth, J. Osterwalder, and T. Greber, *Low cost photoelectron yield setup for surface process monitoring*, Journal of Vacuum Science and Technology A Vacuum, Surfaces, and Films **32**, 023202 (2014).

[130] T. Greber, O. Raetzo, T. J. Kreutz, P. Schwaller, W. Deichmann, E. Wetli, and J. Osterwalder, *A photoelectron spectrometer for k-space mapping above the Fermi level*, Review of Scientific Instruments **68**, 4549–4554 (1997).

[131] P. Baltzer, L. Karlsson, M. Lundqvist, and B. Wannberg, *Resolution and signal-to-background enhancement in gas-phase electron spectroscopy*, Review of Scientific Instruments **64**, 2179–2189 (1993).

[132] A. Kramida, Y. Ralchenko, J. Reader, and NIST Atomic Spectra Database Team, *NIST Atomic Spectra Database (version 5.2), [Online]* (2014).

[133] M. J. Comstock, N. Levy, J. Cho, L. Berbil-Bautista, M. F. Crommie, D. A. Poulsen, and J. M. J. Fréchet, *Measuring reversible photomechanical switching rates for a molecule at a surface*, Applied Physics Letters **92**, 123107 (2008).

[134] S. Hagen, P. Kate, M. V. Peters, S. Hecht, M. Wolf, and P. Tegeder, *Kinetic analysis of the photochemically and thermally induced isomerization of an azobenzene derivative on Au(111) probed by two-photon photoemission*, Applied Physics A **93**, 253 (2008).

[135] F. J. García de Abajo, M. A. Van Hove, and C. S. Fadley, *Multiple scattering of electrons in solids and molecules: A cluster-model approach*, Physical Review B **63**, 075404 (2001).

[136] L. Despont, D. Naumović, F. Clerc, C. Koitzsch, M. G. Garnier, F. J. Garcia De Abajo, M. A. Van Hove, and P. Aebi, *X-ray photoelectron diffraction study of Cu(111): Multiple scattering investigation*, Surface Science **600**, 380–385 (2006).

[137] S. Hüfner, J. Osterwalder, T. Greber, and L. Schlapbach, *Interpretation of substrate photoelectron diffraction*, Physical Review B **42**, 7350–7357 (1990).

[138] D. Friedman and C. Fadley, *Final-state effects in photoelectron diffraction*, Journal of Electron Spectroscopy and Related Phenomena **51**, 689–700 (1990).

[139] K.-M. Schindler, V. Fritzsche, M. C. Asensio, P. Gardner, D. E. Ricken, A. W. Robinson, A. M. Bradshaw, D. P. Woodruff, J. C. Conesa, and A. R. González-Elipe, *Structural determination of a molecular adsorbate by photoelectron diffraction: Ammonia on Ni(111)*, Physical Review B **46**, 4836–4843 (1992).

[140] J. B. Pendry, *Reliability factors for LEED calculations*, Journal of Physics C: Solid State Physics **13**, 937–944 (1980).

[141] K. Pearson, *Note on Regression and Inheritance in the Case of Two Parents*, Proceedings of the Royal Society of London (1854-1905) **58**, 240–242 (1895).

[142] J. Yeh and I. Lindau, *Atomic subshell photoionization cross sections and asymmetry parameters: 1 smaller than Z smaller than 103*, Atomic Data and Nuclear Data Tables **32**, 1–155 (1985).

[143] M. Greif, L. Castiglioni, D. Becker-Koch, J. Osterwalder, and M. Hengsberger, *Acquisition of photoelectron diffraction patterns with a two-dimensional wide-angle electron analyzer*, Journal of Electron Spectroscopy and Related Phenomena **197**, 30–36 (2014).

Acknowledgements

I would like to thank all the people who contributed to this thesis.

First of all, I would like to express my great appreciation to **Jürg Osterwalder** for the opportunity to do my Ph.D. studies in his group, for his encouragement, ideas, and enthusiasm. His knowledge and experience which he contributed to this thesis were very valuable. A very special "thank you" goes to my supervisor **Matthias Hengsberger** who was a big support throughout my thesis. Without your expertise, teaching skills, and guidance this thesis would not have been possible. I would also like to thank my external committee member **Michael Bauer** for his efforts to supervise this thesis. His broad knowledge in the field of high harmonic generation was one of the main reasons for the successful construction of the HHG light source. I would also thank **Thomas Greber** who was a big inspiration with his ideas and interpretation of experimental data.

Big thanks go out to **Claude Monney** who contributed a lot to the construction of TREx and was a great support during my thesis. I would also thank **Titus Neupert** who were a big help for the understanding and interpretation of the experimental data of Bi_2Se_3. A big thank goes to **Luca Castiglioni** who was my office colleague for four years. You were always there if I had a work-related question but we could also always talk about everyday life. A special thanks to **Thomas Kälin** who was a big help with the technical drawings and support in the lab.

I would also like to take the opportunity to thank all the current and past members of the OFP group, namely **Aram, Carlo, Pavel, Kay, Wolf, Adrian H., Dominic, Lisa, Adrian E., Zbynek, Roberta, Fabio, Patrick, Daniel, Benjamin, Jing**. All of you were part of this thesis if it is enjoying coffee breaks, discussing work-related matters, BBQ together or recreational activities.

A big thank you goes out to the workshop of the Physics Institute. You guys constructed many parts for the HHG light source and TREx. Your work was always of highest quality, and I always enjoyed coming by the workshop.

I would also like to express my deepest gratitude to my beloved girlfriend **Valérie Sykora** for the inspiration, and wonderful time we spent together. You were a huge motivation along the way. A big thank you goes out to **Ivan** and **Christa Sykora** for the support and the great hours we spent together.

Last but not least, my deepest heartfelt appreciation goes out to my family **Roland, Regina** und **Katrin Schuler**. You made it possible that I could successfully finish my studies. Thank you very much for your support, love, and care you showed me throughout my whole life.

Curriculum Vitae

Name	Adrian Christian Schuler
Birth	18.12.1983 in Bern (BE), Switzerland
Nationality	Swiss

Education

since 04/2014	Phd student in Physics, University of Zürich, Switzerland Surface Science group of Prof. Dr. Jürg Osterwalder, PhD thesis: Design and implementation of a monochromatic high harmonic generation light source at 100 kHz and its application to time- and angle-resolved photoelectron spectroscopy on Bi_2Se_3
09/2011 - 03/2015	Master of Science in Physics, University of Zürich, Switzerland MSc thesis: Study of the Molecular Switch of TBA/Au(111) by Photoelectron Diffraction and Absorption Spectroscopy
09/2007 - 06/2011	Bachelor of Science in Physics, University of Zürich, Switzerland BSc thesis: Diffraction of low energy electrons on DNA

Working experience

07/2011 - 04/2014	Project Management Office, Project Associate at SwissRe, Zürich, Switzerland

Teaching experience

since 04/2014	Teaching assistant at University of Zürich, Switzerland taught lab-courses and was lecture assistant in physics for medical, bio-medical and physics students

Publications

1. C. Monney, **A. Schuler**, T. Jaounen, M.-L. Mottas, Th. Wolf, M. Merz, M. Muntwiler, L. Castiglioni, P. Aebi, F. Weber, M. Hengsberger, *Robustness of the charge-ordered phases in* $IrTe2$ *against photoexcitation*, PRB **97**, 075110 (2018)
2. **A. Schuler**, M. Greif, A.P. Seitsonen, G. Mette, L. Castiglioni, J. Osterwalder and M. Hengsberger, *Sensitivity of photoelectron diffraction to conformational changes of adsorbed molecules: Tetra-tert-butyl-azobenzene/Au(111)*, Struct. Dyn. **4**, 015101 (2017)
3. H. Cun, A. Spescha, **A. Schuler**, M. Hengsberger, J. Osterwalder and T. Greber, *Characterization of a cold cathode Penning ion source for the implantation of noble gases beneath 2D monolayers on metals: Ions and neutrals*, J. Vac. Sci. Technol. A, **Vol. 34**, No. 2, 020602 (2016)